UNIVERSIDADE D
COIMBRA

Cristiana Filipa Pereira Francisco

Preliminary study of the sensibility to geomagnetic storms of the power network substations in Portugal south region

Dissertação no âmbito do Mestrado em Astrofísica e Instrumentação para o Espaço orientada pela Professora Doutora Maria Alexandra Albuquerque Faria Pais e pelo Doutor Fernando Jorge Gutiérrez Pinheiro e apresentada ao Departamento de Física da Faculdade de Ciências e Tecnologia da Universidade de Coimbra.

Julho de 2020

UNIVERSIDADE DE COIMBRA

FACULDADE DE CIÊNCIAS E TECNOLOGIA

Master in Astrophysics and Instrumentation for Space

Preliminary study of the sensibility to geomagnetic storms of the power network substations in Portugal south region

Cristiana Filipa Pereira Francisco

Advisor

Prof. Dr. Maria Alexandra Albuquerque Faria Pais

Co-Advisor

Dr. Fernando Jorge Gutiérrez Pinheiro

"This thesis does not include the reviews and suggestions done by the Jury"

Coimbra, July 2020

Master in Astrophysics and Instrumentation for Space

Preliminary study of the sensibility to geomagnetic storms of the power network substations in Portugal south region

Cristiana Filipa Pereira Francisco

Advisor
Prof. Dr. Maria Alexandra Albuquerque Faria Pais

Co-Advisor
Dr. Fernando Jorge Gutiérrez Pinheiro

"This thesis does not include the reviews and suggestions done by the Jury"

Preliminary study of the sensibility to geomagnetic storms of the power network substations in Portugal south region

Sumário

A rede elétrica portuguesa é suscetível a tempestades geomagnéticas, que criam correntes geomagnéticas induzidas (GICs) que afetam os transformadores das subestações da rede. Este trabalho começa com uma revisão do processo de acoplamento Sol-Terra, com foco no vento solar como elemento de conexão. Em seguida, é feita uma aplicação original do código de Pethick para explicar o efeito dos modelos de condutividade 1D no cálculo da matriz de impedância MT, seguida por uma análise original de cinco tempestades geomagnéticas durante o início da fase de declínio do ciclo solar 24, combinando dados geomagnéticos do observatório magnético de Coimbra com dados de satélite dos parâmetros do vento solare. Em seguida é usada uma combinação de um determinado modelo simplificado de condutividade, para a região sul de Portugal continental, com os sinais de tempestade geomagnética para produzir gráficos originais do campo elétrico induzido, destacando o efeito da costa. Isso leva, finalmente, ao uso original de uma versão modificada do código GEOMAGICA, num modelo da região sul de Portugal, para testar a sensibilidade de diferentes subestações a uma mudança nas tempestades geomagnéticas e nos parâmetros de resistência de aterramento. Este trabalho também conclui que algumas subestações dificilmente sentem alguma diferença quando a resistência de aterramento é alterada, mas outras sentem, e o facto de se considerar o valor standard de 0.20Ω pode resultar num erro de cálculo da GIC da ordem de $\sim 10\%$.

Palavras-Chave: Interação Sol-Terra; Meteorologia Espacial; Tempestades Geomagnéticas; Magnetotelúrica; Correntes Geomagnéticas Induzidas.

Preliminary study of the sensibility to geomagnetic storms of the power network substations in Portugal south region

Abstract

The Portuguese power network is susceptible to geomagnetic storms, which create geomagnetic induced currents (GICs) that affect the transformers of the network substations. This work starts with a review on the Sun-Earth coupling process focusing on the solar wind as the connecting element. Then it is made an original application of Pethick to explain the effect of 1D conductivity models on the computation of the MT impedance matrix followed by an original analysis of five geomagnetic storms during the begin of decline phase of solar cycle 24, combining geomagnetic data of the magnetic observatory of Coimbra with satellite data of solar wind parameters. Next it is used a combination of a given simplified model of conductivity for the southern region of Portugal mainland with the geomagnetic storm signals, to produce original charts of the induced electric field, highlighting the coast effect. This leads to, finally, an original use of a modified version of the GEOMAGICA code on a model of the Portuguese southern region, to test the sensitivity of different substations to a change in the geomagnetic storms and in the earthing resistance parameters. It is found that the STVR substation has the highest GIC maximum for each storm and that the stronger the geomagnetic storm, the more intense is the GIC in the substations. This work also conclude that some substations hardly feel some difference when the earthing resistance is changed but others do, and the assumption of 0.20 Ω values can result in a GIC miscalculation of the order of $\sim 10\%$.

Keywords: Sun-Earth interaction; Space Weather; Geomagnetic Storms; Magnetotellurics; Geomagnetic Induced Currents.

Dedicated to grandmother Inês!

Acknowledgements

This work could not have been done without the help and support of my family, friends, advisors and colleagues, and it is dedicated to all of those people that has contributed to my academic and personal progress.

To my parents, for all the support through the years and for providing me with the opportunity to attend the university, and to my big brother, who always helped me, pushed me forward and believed in me.

To my partner of the last nine years, Paulo. I can't put into words everything he is for me and I can't thank him enough for the help, support and love through all this time.

A special thanks to my advisors, Professor Doctor Alexandra Pais and Doctor Fernando Pinheiro, for all the patient and advice through all the process and for introducing me in CITEUC (Earth and Space Research Center of the University of Coimbra) and to Paulo Ribeiro, senior technician at OGAUC and researcher at CITEUC, who helped me with storm analysis.

A special thanks to Professor Doctor Fernando Acácio Monteiro dos Santos from the department of Geographic Engineering, Geophysics and Energy of the Faculty of Science of the University of Lisbon, for all the help with the understanding of the principles of the magnetotelluric method, and also to Doctor Joana Alves Ribeiro (CITEUC) for all the advice and guidance through this work.

To all my dearest and oldest friends, especially Daniela Pedroso, Marco Pinto and Francisco Almeida, for all the support through years and years.

I can't forget the SportZone family where I've been working for the last five years and who never ever let me give up on my studies.

Lastly, I wish to thank the Jury: Professor Doctor Margarida Maria Lopes da Silva Camarinha, Professor Doctor Fernando Acácio Monteiro dos Santos and Professor Doctor João Manuel Rendeiro Cardoso.

This study was carried out in the framework of project MAG-GIC: PTDC/CTA-GEO/31744/2017, funded by FCT (Foundation for Science and Technology, I.P.), a research project from CITEUC. CITEUC is funded by National Funds through FCT (project: UID/MUL-

TI/00611/2019) and FEDER European Regional Development Funds through COMPETE 2020 Operational Programme Competitiveness and Internationalization (project: POCI-01-0145-FEDER-006922). We greatly acknowledge the collaboration with REN (Rede Elétrica Nacional).

Acronyms

1D one-dimensional

2D two-dimensional

3D three-dimensional

ACE Advanced Composition Explorer

CIR Corotating Interaction Regions

CITEUC Centro de Investigação da Terra e do Espaço da Universidade de Coimbra

CME Coronal Mass Ejection

COI IAGA code for Coimbra Magnetic Station (Portugal)

Dst Disturbance storm-time index

EM Electromagnetic

emf Electromotive force

FAC Field-aligned current

GAI Geomagnetic Activity Indices

GSE Geocentric Solar Ecliptic Coordinate System

GSFC Goddard Space Flight Center

GSM Geocentric Solar Magnetic Coordinate System

GSW Geocentric Solar Wind Coordinate System

GIC Geomagnetically Induced Current

HMF Heliospheric Magnetic Field

HV High-Voltage

IAGA International Association of Geomagnetism and Aeronomy

IMF Interplanetary Magnetic Field

IMP Interplanetary Monitoring Platform

ISEE International Sun-Earth Explorer

K Local K geomagnetic index

Kp Planetary K index

LV Low-Voltage

MHD Magnetohydrodynamics

MT Magnetotelluric

NASA National Aeronautics and Space Administration

NLL Newell's Coupling function

NOAA/SWPC National Center for Environmental Information/Space Weather Prediction Center

OGAUC Observatório Geofísico e Astronómico da Universidade de Coimbra

ppm parts per million

SFE Solar Flare Effect

SSC Storm sudden commencement

SW Solar Wind

SWE Space Weather

TE Transverse Electric mode

TM Transverse Magnetic mode

UT Universal Time

Physical Constants

Fundamental Constants

π	≈ 3.1416		
m_p	$= 1.67262192369 \times 10^{-27}$	kg	proton's mass
m_e	$= 9.10938356 \times 10^{-31}$	kg	electron's mass
c	$= 299792458$	m s^{-1}	speed of light in vacuum
G	$= 6.674184 \times 10 - 11$	m^3 kg^{-1} s^{-2}	gravitational constant
k_B	$= 1.380649 \times 10^{-23}$	J K^{-1}	Boltzmann constant
σ_{sb}	$= 5.6704 \times 10^{-8}$	W m^{-2} K^{-4}	Stefan-Boltzmann constant
ε_0	$= 8.85 \times 10^{-12}$	F m^{-1}	permitivity of free space
μ_0	$= 4\pi \times 10^{-7}$	H m^{-1}	permeability of free space
R	$= 8.314462618$	J mol^{-1} K^{-1}	Perfect gas constant

Fundamental Earth Parameters

R_E	$= 6371$	km	Mean radius
M_E	$= 5.97219 \times 10^{24}$	kg	Mass
1 AU	$= 1.495978707 \times 10^{11}$	m	Orbital radius

Fundamental Sun Parameters

$M_\odot$	$= 1.99 \times 10^{30}$	m	Mass
$R_\odot$	$= 6.96 \times 10^{8}$	m	Mean radius
$L_\odot$	$= 3.844 \times 10^{36}$	W m^{-2} K^{-4}	Luminosity
T_{eff}	$= 5778$	K	Effective Black Body Temperature
$\Omega_\odot$	$= 2.7 \times 10^{-6}$	rad s^{-1}	Angular velocity of the Sun's rotation

Symbols

i	Complex number
Re	Real part of a complex number
Im	Imaginary part of a complex number
$\partial/\partial t$	Time derivative
∇	Nabla operator
∞	Infinite

t	Time	[s]
T	Period	[s]
f	Frequency	[Hz = s^{-1}]
ω	Angular frequency	[s^{-1}]
$\mathbf{k}$	Wavenumber	[m^{-1}]
$\mathbf{B}$	Magnetic field	[T = V s m^{-2}]
$\mathbf{E}$	Electric field	[V m^{-1}]
$\mathbf{Z}$	Impedance	[V A^{-2}]
ε	Electrical permittivity	[A s $V^{-1}m^{-1}$ = F m^{-1}]
μ	Magnetic permeability	[V s $A^{-1}m^{-1}$ = H m^{-1}]
I	Current	[A]
$\mathbf{j}$	Current density	[A m^{-2}]
h	Surface-Layer thickness	[m]
ρ	Resistivity	[Ω m = V m A^{-1}]
ρ_a	Apparent resistivity	[Ω m = V m A^{-1}]
σ	Conductivity	[S m^{-1} = A V^{-1} m^{-1}]
η_f	Free Charge Density	[C·m$^-$3]
δ	Skin Depth	[m]

R_G	Grounding/earthing resistance	
R_{eq}	Equivalent circuit resistance	
R	Resistance of each phase line	
$\mathbf{J}^e$	vector of perfect earthing currents	
$\mathbf{Y}^n$	network admittance matrix	
$\mathbf{Z}^e$	earthing impedance matrix	
$\mathbf{I}^e$	GICs in earthing connections	
$\mathbf{B}_{mp}$	Magnetic field at the magnetopause nose	[T = V s m^{-2}]
$\mathbf{u}_{mp}$	Solar wind velocity at the magnetopause nose	[km h^{-1}]
$\mathbf{u}$	Solar wind velocity	[km h^{-1}]

Contents

List of Figures

List of Tables

Chapter 1

Introduction

Space Weather is a branch of Space Physics that studies the impact of the solar activity onto the Earth where it can cause issues on our technological systems like disruption of satellite operations or of electric power distribution grids, or even endanger human life or health.

Back on 1839, Gauss had already postulated the possibility of electric currents in space altering the magnetic field observed on the ground. A few decades later, in 1860, Carrington has seen a relation between auroral displays and magnetometer perturbations during the superstorm of that year. They were not the only ones to see a relation between the magnetic field and electric current systems. In 1882, Stewart has come to the conclusion that solar radiation ionizes the upper atmosphere to allow for electric currents to flow in this region. But only in the early 1900's Birkeland found out that there are field-aligned currents from solar wind particles, connecting the magnetosphere to the Earth's ionosphere, leading to the aurora.

Geomagnetic induced currents (GICs) are defined as slowly varying quasi-direct currents induced by variations in the geomagnetic field (through the interaction of the solar wind plasma with the magnetosphere) in a grounded conductive network. This means that due to these variations there will be an electromotive force along the ground and the power lines, leading to currents flowing from the Earth into the power lines and vice versa.

It was in 1989 that these induced currents caused a lot of damage to the power grid in Quebec, Canada, leading to a total collapse of it. At the time it only affected telegraphs but if it happened nowadays the consequences would be much more serious due to our modern way of living, highly dependent on the electric power. It would affect from home supplies to hospital infrastructures.

Consequently, the main objective of this work is to make a first approach to the GIC calculation for real geomagnetic storms and understand how the power network substations in the Portuguese south region respond to these currents.

Since Pirjola (1985) many GICs studies have been done through the world and some examples can be seen in Table 1.1.

Country	Studies
Finland	Pirjola (1985) and Makinen (1993)
Canada	Boteler et al. (1994)
UK	Erinmez et al. (2002), McKay (2004), Turnbull (2010), Turnbull (2011) and Kelly et al. (2017)
USA	Radasky et al. (2006), Arajarvi and Viljanen (2008), Gilbert et al. (2012) and Bernabeu (2012)
South Africa	Koen and Gaunt (2003), Bernhardi et al. (2008), Ngwira et al. (2008) and Tarditi and Harte (2014)
Sweden	Wik et al. (2008)
Norway	Myllys et al. (2014)
Spain	Torta et al. (2014)
France	Kelly et al. (2017)
Australia	Marshall et al. (2011)
New Zealand	Marshall et al. (2012)
Brazil	da Silva Barbosa et al. (2015)
Uruguay	Caraballo et al. (2013)
China	Zheng et al. (2012), Liu et al. (2013), Liu et al. (2014) and Guo et al. (2014)

Table 1.1: Some of the studies already made on GICs in some countries around the world.

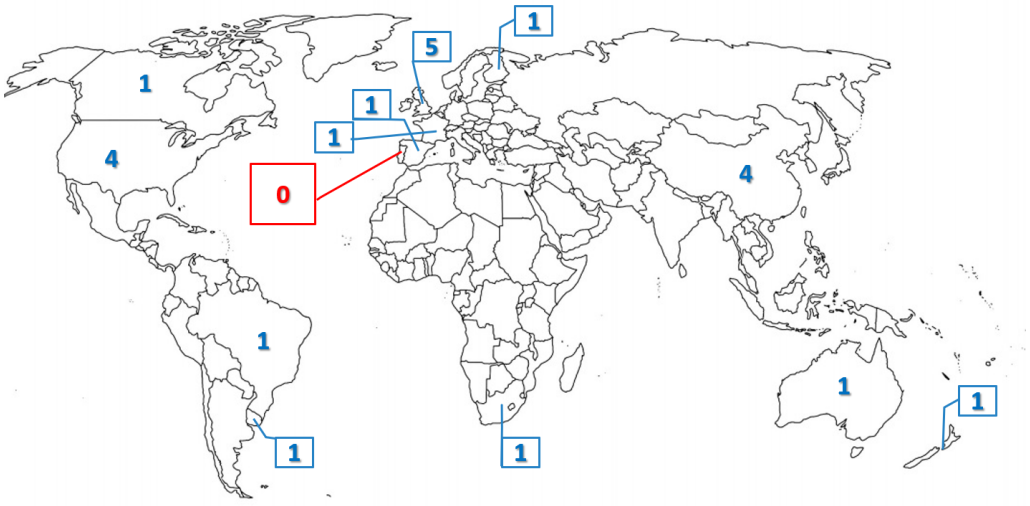

Figure 1.1: Schematic of the number of studies on GICs already made per country as shown in Table 1.1.

The *MAG-GIC* Project (Geomagnetically induced currents in Portugal mainland, PTDC/CTA-GEO/31744/2017) is the first of its kind to study these currents and their effects in Portuguese territory. It has the collaboration of REN (Rede Elétrica Nacional) to build the

power network model. This thesis work has been done in the framework of the *MAG-GIC* project.

The structure that has been chosen to this thesis covers the whole GIC generation process.

Chapter 2 is a journey through the Sun's structure, the solar wind and its interaction with the Earth's magnetosphere. Here lies the theoretical fundamentals to help to understand what are the geomagnetic storms described and characterized in Chapter 4.

Chapter 3 introduces the Geophysics contribution to this work with the description of the Magnetotelluric method from its first principles, through some field considerations to the data processing. Some realistic applications of this model are done for the case of a layered earth (1D model).

The geomagnetic storms precursors and proxies are explained in Chapter 4 to help to understand why and how were the storms of 2015 chosen with the data extracted from NASA/GSFC's OMNI data base and with the local magnetic field provided by COI observatory. In this chapter the induced electric field from each storm is also computed.

The main goal of this work is reached in Chapter 5.3 which starts with a physical explanation of the GICs in the power network system and also has the description of the Lethien-Pirjola method to calculate GICs. This method is used at first with a uniform induced electric field of 1 V km^{-1} that allows to see the direction of the induced field for which each substation has its GIC maximum. The GICs are also computed for the storms analyzed in Chapter 4 and for different values of earthing resistances. Finally, a conclusion is drawn on which set of substations appears to be particularly interesting for future studies and, in particular, for the installation of a GIC sensor.

Chapter 2

Theoretical Background on Sun-Earth interaction

2.1 The Sun

The Sun is a nearly perfect sphere of hot plasma at the center of the Solar System. It is mainly constituted of hydrogen (about 73%) and helium (approximately 25%) and small amounts of heavier elements such as oxygen, carbon, neon, and iron. It has its origin in an interstellar gas cloud with a mass of the order of $10^4 M_\odot$ that collapsed due to some interstellar gravitational perturbation (Koskinen, 2011). The Sun has a spectral classification of *G2* with a photosphere temperature close to 5778 K and a luminosity classification *V*. Both classifications cause the Sun to be in the Main Sequence of the Hertzsprung-Russel Diagram (see Figure 2.1). (Carneiro, 2005)

The structure of the Sun (Figure 2.2) can be divided into the **core** (is the center of the Sun, where nuclear fusion occurs), the **radiative zone** (is the layer immediately after the core, with a lower density and emits the radiation diffused from the core), the **convective zone** (is dominated by convection currents that allow the transport of the energy produced in the Sun's core) and the outer layers that constitute the solar atmosphere (see Subsection 2.1.1).

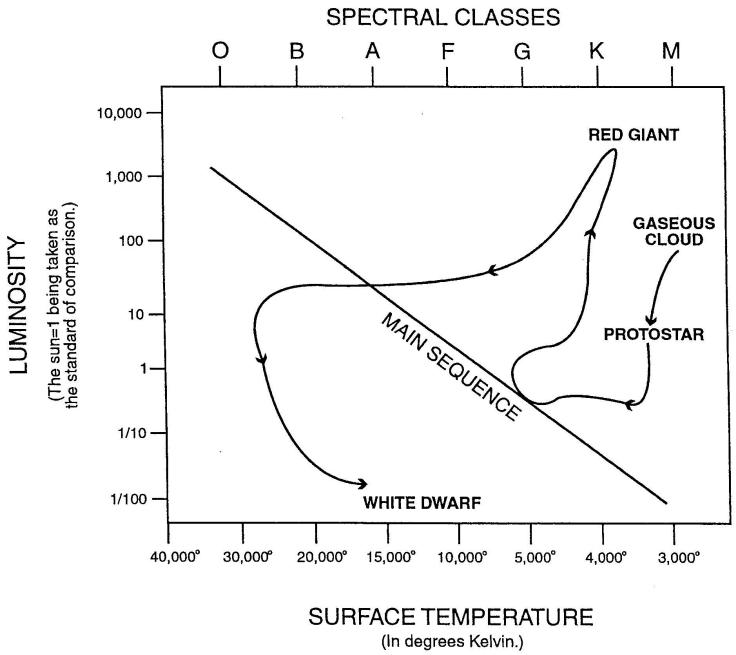

Figure 2.1: The Hertzsprung-Russel Diagram for the Sun, including its birth, the present time and what will come based on its characteristics. It also shows the Main Sequence of the H-R diagram. (Carneiro, 2005)

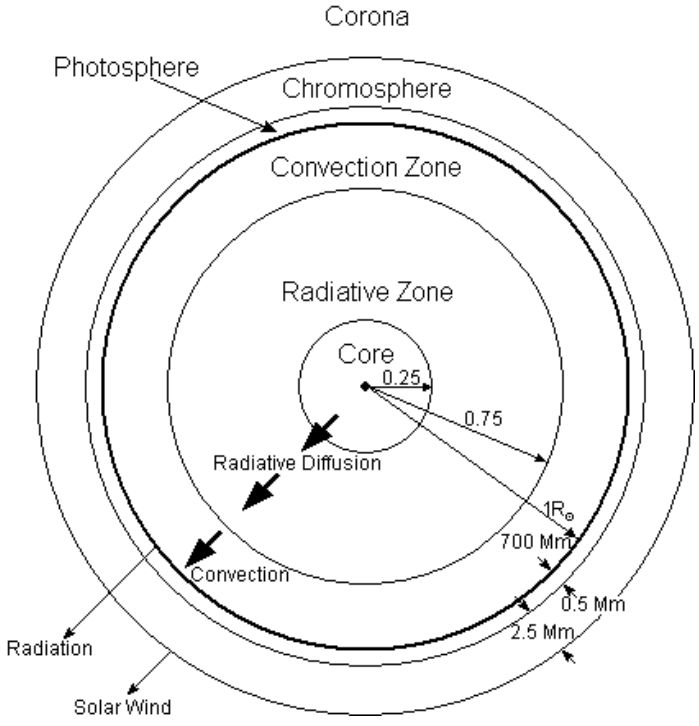

Figure 2.2: The Structure of the Sun. Image taken from https://tinyurl.com/yag66lx5.

Some of the main parameters characterizing the Sun are listed in Table 2.1. The solar constant is defined as the quantity of radiant solar energy received at the outer layer of the Earth's atmosphere.

Quantity	Estimate
Age	$\sim 4.55 \times 10^9$ yr
Mass	1.99×10^{30} kg
Radius	6.96×10^8 m
Luminosity	3.84×10^{26} W
Density (mean)	1.4×10^3 kg m^{-3}
Density (center)	151×10^3 kg m^{-3}
Solar Constant, G_{SC}	1367 W m^{-2}
Temperature (center)	15.6×10^6 K
Temperature (photosphere)	5778 K
Angular velocity of the Sun's rotation	2.7×10^{-6} rad s^{-1}

Table 2.1: Global parameters of the Sun. Values taken from Basu and Antia (2008) and Hughes (2016).

2.1.1 Solar atmosphere

The solar atmosphere consists of the three outer layers seen in Figure 2.2: Photosphere, Chromosphere and Corona. The temperature variation between them can be seen in Figure 2.3.

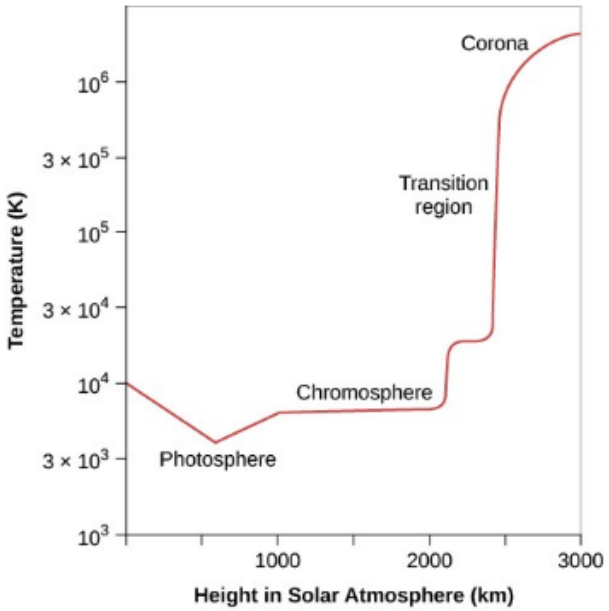

Figure 2.3: Temperature variation in the solar atmosphere. Image taken from `https://tinyurl.com/y5g8xmf3`

The **photosphere** is 500 km thick and absorbs almost all energy carried by convection leading to a decrease of the temperature from 6600 K at the bottom to 4300 K at the top. It radiates at a temperature of 5778 K, the effective black body temperature (Koskinen,

2011). There are some active regions characterized as hot bright areas in the photosphere (plague or faculae) that develop together with sunspots which are cold and dark regions.

The **chromosphere** is 3000 - 5000 km thick with low particle density and an average temperature about 10 000 K. (Kontar et al., 2008; Koskinen, 2011)

The **transition zone** is located between the chromosphere and the corona and it is characterized by a rapid temperature rise in a very short distance.

The **corona** is the outermost part of the Sun's atmosphere, it is usually hidden by the bright light of the Sun's photosphere and for that it can only be seen during a total solar eclipse. It extends far out into space and is the place of origin of the solar wind (Koskinen, 2011). From this region occurs large releases of magnetized plasma into the solar wind, called coronal mass ejections (CME). They occur more often and are more intensely close to the solar maximum in the 11-year solar cycle.

2.2 The Solar Wind

The Solar wind is a continuous stream of plasma that consists mainly of protons, electrons and alpha particles, carrying a weak magnetic field, that escape the corona because the gases in it are hot and moving so rapidly that they cannot be held back by solar gravity. (Caraballo, 2016; Thiel, 2008)

For observations at 1 AU, *i.e.*, at the mean distance between the Earth and the Sun, the solar wind can be divided into two categories: slow and fast solar wind (Table 2.2). They both originate in the Sun, but from different regions. The fast solar wind has its origin in coronal holes, that are regions with low density and temperature where the magnetic field lines arch away and close in infinity. On the other side, the slow solar wind is originated in regions close to the solar equator at the boundary between open and closed field lines. (Antiochos et al., 2011)

	Slow Solar Wind	**Fast Solar Wind**
Velocity	$250 - 400$ km s^{-1}	$400 - 800$ km s^{-1}
Mean proton density at 1AU	8 cm^{-3}	3 cm^{-3}
Proton Temperature	$\sim 3 \times 10^4$ K	$\sim 2 \times 10^5$ K
Electron Temperature	$\sim 8 \times 10^5$ K	$\sim 1 \times 10^5$ K
Origin	regions close to the solar equator (heliospheric sheet)	coronal holes

Table 2.2: Differences between the slow and fast solar wind. Values taken from Kallenrode (2003)

These two sorts of streams interact with each other in the interplanetary medium and alternately pass by the Earth as the Sun rotates. They interact with the Earth's magnetic field and they can produce geomagnetic storms. (Kallenrode, 2003)

2.2.1 Solar wind expansion

Chapman Model

In 1957 Chapman proposed to describe the existence of the continuous solar wind with a static model with the assumption that "the corona and its distant extensions were static and that energy was transferred only by conduction" (Goossens, 2012). The two most important points of this model are that conduction is important for maintaining the corona and its extensions and that the gaseous medium near the Earth is regarded as an extended part of the corona. (Goossens, 2012; Koskinen, 2011)

Considering a sphere around the Sun with a constant thermal flux through the surface (Ambastha, 2020; Koskinen, 2011) given by

$$\mathbf{Q} = -k\nabla T \tag{2.1}$$

with ∇T the temperature gradient and $k = k_0 T^{5/2}$ the thermal conductivity, where $k_0 \approx 1.8 \times 10^{-11}$ W m^{-1} K$^{-7/2}$ (Cairns, 2000). Once there are no heat sources or sinks, $\nabla \cdot \mathbf{Q} = 0$, and it comes

$$\nabla \cdot (k\nabla T) = 0 \Leftrightarrow \nabla \cdot (k_0 T^{5/2} \nabla T) = 0 \tag{2.2}$$

Considering a heat flux radially outward when assuming that coronal heating occurs close to the Sun (Cairns, 2000) it leads to

$$\frac{1}{r^2}\frac{\mathrm{d}}{\mathrm{d}r}\left(r^2 k_0 T^{5/2}\frac{\mathrm{d}T}{\mathrm{d}r}\right) = 0 \tag{2.3}$$

Assuming also that $T \to 0$ when $r \to \infty$, the temperature T at a distance r from the Sun is, from Equation (2.3):

$$T = T_0\left(\frac{R_\odot}{r}\right)^{2/7} \tag{2.4}$$

where $T_0 = 2 \times 10^6$ K is the temperature at the base of the corona, at $r \sim R_\odot$. This has a huge breakthrough since it gives $T \sim 4 \times 10^5$ K at the Earth's location and that is extremely close to the value measured years later ($T \sim 1.2 \times 10^5$ K according to Gosling (2007)).

However, this model had a disadvantage, the pressure solution. According to Chapman's model, an hydrostatic equilibrium for the corona plasma is assumed and it is given by

$$\nabla P = -\nabla U \tag{2.5}$$

where

$$U = -\frac{GM_\odot \rho}{r} \tag{2.6}$$

is the gravitational potential that gives the gravitational force per unit volume with

$$\rho = n(m_e + m_p) \simeq n m_p$$

the density of the plasma where n is the number of proton-electron pairs per unit volume and m_e and m_p the mass of the electron and proton, respectively. Note that the total number of particles per unit volume is $2n$.

From Equations (2.5) and (2.6), in a spherical symmetry it comes

$$\frac{dP}{dr} = -\frac{GM_\odot}{r^2} n m_p \tag{2.7}$$

Using the ideal gas equation for the electrons and protons in the plasma and assuming the same temperature T for both, then

$$P = \frac{N^{moles} RT}{V} = \frac{N^{part} k_B T}{V} \tag{2.8}$$

whit $R = 8.3144621$ J K^{-1}mol^{-1} the perfect gas constant, N^{moles} and N^{part} the total number of moles and particles, respectively, and k_B the Boltzmann constant.

As $N^{part}/V = 2n$ (total number of particles per unit volume) it comes

$$P = 2nk_B T \tag{2.9}$$

Using Equation (2.4) for $T(r)$ in Equation (2.9) it comes

$$P(r) = 2nk_B T_0 \left(\frac{R_\odot}{r}\right)^{2/7} \tag{2.10}$$

Comparing this equation with Equation (2.7) it comes that $n = n(r)$ and by replacing one in the other it yields

$$\frac{d}{dr}\left(\frac{n(r)}{r^{2/7}}\right) = -\frac{GM_\odot m_p}{2k_B T_0 R_\odot^{2/7}} \frac{n(r)}{r^2} \tag{2.11}$$

which can be simplified to

$$\frac{d}{dr}\left(\frac{n(r)}{r^{2/7}}\right) = -K\frac{n(r)}{r^2} \tag{2.12}$$

by defining a constant $K = \dfrac{GM_\odot m_p}{2k_B T_0 R_\odot^{2/7}}$. Equation (2.12) can be solved by using the integrating factor method:

$$\frac{d}{dr}\left(\frac{n(r)}{r^{2/7}}\right) + \frac{K}{r^{12/7}}\frac{n(r)}{r^{2/7}} = 0 \Rightarrow \frac{d}{dr} f(r) + a(r) f(r) = 0 \tag{2.13}$$

with $f(r) = \dfrac{n(r)}{r^{2/7}}$ and $a(r) = \dfrac{K}{r^{12/7}}$. The integrating factor is $e^{\int a(r)dr} = e^{\int Kr^{-12/7}dr} =$ $= \exp\left(-\dfrac{7}{5}Kr^{-5/7}\right)$.

Multiplying Equation (2.13) by the integrating factor it comes

$$\frac{d}{dr}\left[\exp\left(-\frac{7}{5}Kr^{-5/7}\right) f(r)\right] = 0 \Leftrightarrow \exp\left(-\frac{7}{5}Kr^{-5/7}\right) f(r) = constant = C_1 \tag{2.14}$$

and substituting $f(r)$,

$$\exp\left(-\frac{7}{5}Kr^{-5/7}\right)\frac{n(r)}{r^{2/7}} = C_1 \tag{2.15}$$

Defining n_0 as the number density of protons at $r = R_\odot$, *i.e.*, at the base of the corona, the constant C_1 is then

$$C_1 = \exp\left(-\frac{7}{5}KR_\odot^{-5/7}\right)\frac{n_0}{R_\odot^{2/7}} \tag{2.16}$$

Using Equation (2.16) in (2.15) leads to

$$n(r) = n_0\left(\frac{r}{R_\odot}\right)^{2/7}\exp\left[-\frac{7}{5}K(R_\odot^{-5/7} - r^{-5/7})\right] \Leftrightarrow$$

$$\Leftrightarrow n(r) = n_0\left(\frac{r}{R_\odot}\right)^{2/7}\exp\left[-\frac{7}{5}KR_\odot^{-5/7}\left(1-\left(\frac{r}{R_\odot}\right)^{-5/7}\right)\right]$$

substituting K it finally comes

$$n(r) = n_0\left(\frac{r}{R_\odot}\right)^{2/7}\exp\left[\frac{7}{5}\frac{GM_\odot m_p}{2k_BT_0R_\odot}\left(\left(\frac{R_\odot}{r}\right)^{5/7}-1\right)\right] \tag{2.17}$$

Using this result in Equation (2.10) it gives the radial dependence for pressure:

$$P(r) = P_0\exp\left[\frac{7}{5}\frac{GM_\odot m_p}{2k_BT_0R_\odot}\left(\left[\frac{R_\odot}{r}\right]^{5/7}-1\right)\right] \tag{2.18}$$

where $P_0 = 2n_0k_BT_0$ is the pressure at the coronal base (Cairns, 2000). For large distances from the Sun, Equation (2.18) becomes

$$P_\infty = P_0\exp\left(-\frac{7}{5}\frac{GM_\odot m_p}{2k_BR_\odot T_0}\right) \approx 10^{-6}\text{ Pa} \tag{2.19}$$

for coronal values of temperature and densities. This shows a finite pressure at large distances from the Sun, although the pressure of the interstellar medium is thought to be lower than this by a factor of $\sim 10^7$. (Ambastha, 2020; Cairns, 2000)

Parker Model

Looking to the results of Chapman, Eugene Parker concluded that it is not correct to consider the corona in a static equilibrium, that is the corona must be dynamic (either expanding, or collapsing). (Ambastha, 2020)

Parker presented his solution in 1958, showing that because gravity weakens with the increase of the distance to the Sun, the outer coronal atmosphere can escape supersonically into the interplanetary space. The Sun's corona is strongly attracted by solar gravity but due to its large thermal conductivity it is also very hot at large distances, which means that the corona can be taken as approximately isothermal (Ambastha, 2020). Then considering a spherically symmetric flow in steady motion out from the Sun, the acceleration of the

gas due to a pressure gradient and gravity can be described by:

$$\rho \mathbf{u} \cdot \nabla \mathbf{u} = -\nabla P - \nabla U \tag{2.20}$$

The radial component is:

$$\rho u \frac{\mathrm{d}u}{\mathrm{d}r} = -\frac{\mathrm{d}P}{\mathrm{d}r} - \frac{GM_\odot \rho}{r^2} \tag{2.21}$$

which is the momentum conservation equation with u the speed of expansion. (Ambastha, 2020; Cairns, 2000)

Considering that it is a perfect gas and the rate of mass loss is constant, and the expansion is isothermal at temperature T_i, it is possible to obtain the following relation:

$$\begin{aligned} &\left(u - \frac{2k_B T_i}{m_p u}\right)\frac{\mathrm{d}u}{\mathrm{d}r} - \frac{4k_B T_i}{m_p r} + \frac{GM_\odot}{r^2} = 0 \Leftrightarrow \\ &\Leftrightarrow \frac{1}{u}\frac{\mathrm{d}u}{\mathrm{d}r}\left(u^2 - \frac{2k_B T_i}{m_p}\right) = \frac{4k_B T_i}{m_p r} - \frac{GM_\odot}{r^2} \end{aligned} \tag{2.22}$$

The solutions for this equation are represented in Figure 2.4. Different solution curves correspond to different flow speeds at the base of the corona, *i.e.*, $u(R_\odot)$.

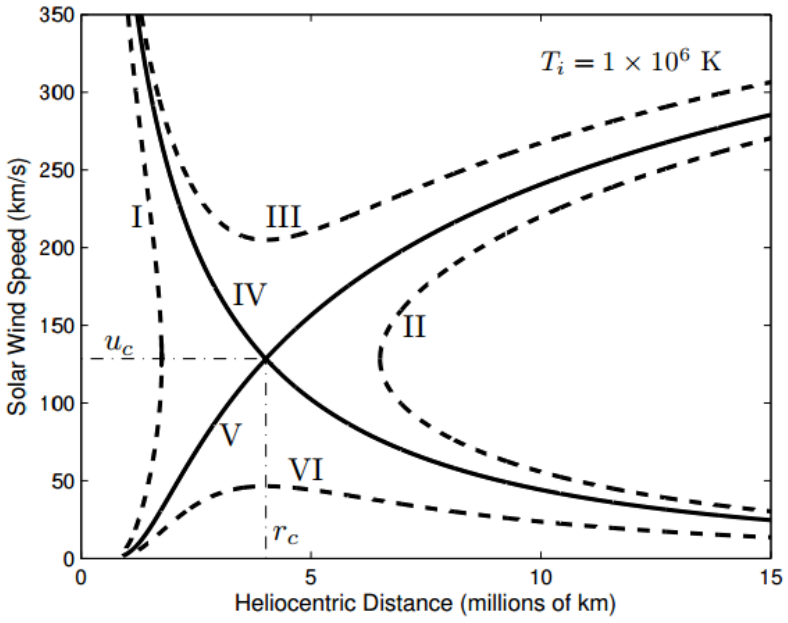

Figure 2.4: Graphic representation of the six solution curves for Equation (2.22) with $T_i = 1 \times 10^6$ K the typical coronal temperature. (Hughes, 2016)

The so-called critical point is where solutions IV and V intersect, and is defined by ($r = r_c$, $u = u_c$). From Equation (2.22) it can be computed r_c when $\mathrm{d}u/\mathrm{d}r = 0$ from solutions III and VI, giving

$$r_c = \frac{GM_\odot m_p}{4k_B T_i} \tag{2.23}$$

Using solutions I and II where $\left.\frac{\mathrm{d}u}{\mathrm{d}r}\right|_{u=u_c, r\neq r_c} = \pm\infty$ it is also possible to define

$$u_c^2 = \frac{2k_B T_i}{m_p} \tag{2.24}$$

The two parameters r_c and u_c are the radial distance and velocity at the critical point. They can be used to simplify Equation (2.22):

$$\frac{1}{u}\frac{\mathrm{d}u}{\mathrm{d}r}(u^2 - u_c^2) = 2\frac{u_c^2}{r^2}(r - r_c) \tag{2.25}$$

where $u_c = \sqrt{\frac{2k_B T}{m_p}}$ has a particular physical meaning: it is the isothermal sound speed in the corona, at temperature T_i.

In order to see which of the six solutions actually represents the solar wind flow it is necessary to analyze them from Figure 2.4. Solution I and II can be ruled out on the basis of having double-valued flow speed values. Solutions III and IV can be rejected because they are supersonic at the base of the corona and do not fit the observations of small Doppler shifts near the base of the corona. (Hughes, 2016; Hundhausen, 2012)

Solutions V and VI appear to be the most plausible ones to explain the solar wind flow. They both start with low flow speeds at the base of the corona as seen in observations, but then they diverge: solution VI remains subsonic and has $u \to 0$ as $r \to \infty$ while solution V is supersonic beyond the critical radius. For solution VI, density and pressure tend to unrealistic large values as $r \to \infty$. Finally, for solution V, the density and pressure tend to zero with increasing r which is in agreement with the solar wind merging into the low pressure, interstellar background. (Hughes, 2016; Hundhausen, 2012)

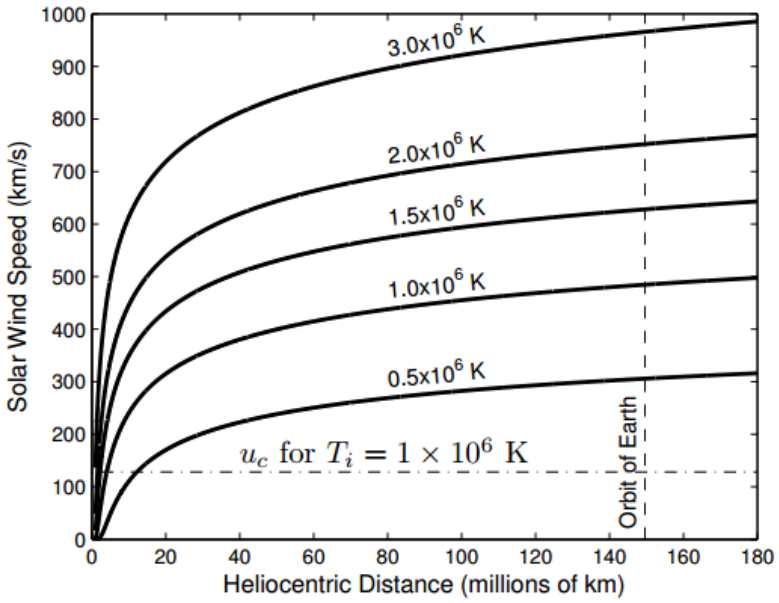

Figure 2.5: Solar wind speed according to solution V for multiple coronal temperatures T_i, as a function of heliocentric distance. (Hughes, 2016)

The explicit expression for this solution is found by integrating Equation (2.25), leading to Parker's solution:

$$\left(\frac{u}{u_c}\right)^2 - \ln\left(\frac{u}{u_c}\right)^2 = 4\ln\left(\frac{r}{r_c}\right) + \frac{4r_c}{r} + C \tag{2.26}$$

with C the integration constant. The solar wind speed for several values of coronal temperatures T_i according to solution V can be seen in Figure 2.5.

2.2.2 The Frozen-in flux Theorem

The frozen-in flux theorem, also known as the **Alfvén's theorem**, states that "in a fluid with infinite electric conductivity, the magnetic field is frozen into the fluid and has to move along with it", (Alfvén, 1942). In other words, it is like if the magnetic field was *frozen in* to the plasma.

Starting with Ohm's law in the rest frame of the plasma:

$$\mathbf{j}' = \sigma\mathbf{E}' \tag{2.27}$$

with $\mathbf{j}'$ and $\mathbf{E}'$ the electric current density and electric field. However, most of the time the solar wind plasma is observed/measured from a different frame than this, typically from Earth relative to which the plasma velocity is $\mathbf{u}$. It is then necessary to apply the Lorentz transformation to the fields (Hughes, 2016). So, considering the typical observed solar wind speed $\mathbf{u}$ then $\mathbf{j}' = \mathbf{j}$ and $\mathbf{E}' = \mathbf{E} + \mathbf{u} \times \mathbf{B}$ for $\frac{u}{c} \ll 1$. The Ohm's law becomes

$$\mathbf{j} = \sigma(\mathbf{E} + \mathbf{u} \times \mathbf{B}) \tag{2.28}$$

with $\mathbf{j}$, $\mathbf{E}$ and $\mathbf{B}$ in the frame where the plasma moves with velocity $\mathbf{u}$.

Considering an essentially infinite conductivity, the current $\mathbf{j}$ will remain finite only if

$$\mathbf{E} + \mathbf{u} \times \mathbf{B} = 0 \tag{2.29}$$

The flux of the magnetic field through an open surface S attached to the plasma is

$$\Phi = \iint_{S(t)} \mathbf{B}(\mathbf{r}, t) \cdot d\mathbf{S} \tag{2.30}$$

This surface may deform, expand or contract when moving with the plasma and the goal is to evaluate how Φ changes with it, *i.e.*,

$$\frac{\mathrm{d}\Phi}{\mathrm{d}t} = \frac{\mathrm{d}}{\mathrm{d}t} \iint_{S(t)} \mathbf{B}(\mathbf{r}, t) \cdot d\mathbf{S} \tag{2.31}$$

Since the limits of the integral are functions of t, the time derivative is not simple, it is

necessary to use the Leibniz integral rule in three dimensions:

$$\frac{\mathrm{d}}{\mathrm{d}t}\iint\limits_{S(t)}\mathbf{B}(\mathbf{r},t)\cdot d\mathbf{S}=\iint\limits_{S(t)}\left(\frac{\partial}{\partial t}\mathbf{B}(\mathbf{r},t)+[\nabla\cdot\mathbf{B}(\mathbf{r},t)]\mathbf{u}\right)\cdot d\mathbf{S}-\oint\limits_{c(t)}[\mathbf{u}\times\mathbf{B}(\mathbf{r},t)]\cdot d\mathbf{c} \quad (2.32)$$

with $c(t)$ a closed contour bounding surface $S(t)$.

Applying the Gauss' law for magnetism ($\nabla\cdot\mathbf{B}=0$) and the Faraday law ($-\frac{\partial\mathbf{B}}{\partial t}=\nabla\times\mathbf{E}$) to the first term on the RHS and the Stokes theorem to the second term, Equation (2.31) becomes

$$\frac{\mathrm{d}\Phi}{\mathrm{d}t}=\iint\limits_{S(t)}-\nabla\times\mathbf{E}\cdot d\mathbf{S}-\iint\limits_{S(t)}\nabla\times(\mathbf{u}\times\mathbf{B})\cdot d\mathbf{S} \quad (2.33)$$

Since the sum of integrals in the same surface is the integral of the sum, and knowing that the same property applies to the curl of a vector, i.e., $\nabla\times\mathbf{A}+\nabla\times\mathbf{B}=\nabla\times(\mathbf{A}+\mathbf{B})$ it means that

$$\frac{\mathrm{d}\Phi}{\mathrm{d}t}=-\iint\limits_{S(t)}\nabla\times(\mathbf{E}+\mathbf{u}\times\mathbf{B})\cdot d\mathbf{S} \quad (2.34)$$

Equation (2.29) then implies that

$$\frac{\mathrm{d}\Phi}{\mathrm{d}t}=0 \quad (2.35)$$

This means that for a perfectly conducting plasma there is a constant flux through an arbitrary surface convecting with the plasma, *i.e.*, there is no relative motion between magnetic field lines and the convecting plasma: the magnetic field is *frozen* into the plasma. (Hughes, 2016)

2.2.3 Parker spiral model

In 1958, Eugene Parker also explained why there is a mass loss of gas streaming outward from the Sun due to coronal heating. He started by assuming that the solar wind velocity, along with the Sun's rotation, define the shape of the magnetic field lines, making them to "draw" a spiraled shape – an Archimedean spiral. He also assumed that due to high conductivity of plasma, the frozen-in theorem applies and because of that the magnetic field is carried through interplanetary space along with the motion of ionized particles in the solar wind and it is called *interplanetary magnetic field* (IMF). (Ambastha, 2020; Goossens, 2012; Hughes, 2016; Vo, 2018)

In Figure 2.6 it can be seen the solar wind parcels launched from four different locations on the source equator. Taking one of them to see in more detail, it is indicated the locations of six parcels launched from the Sun at equally-spaced time intervals (t_0 being the most distant parcel and t_5 the most recent one). (Hughes, 2016) Starting by considering the solar wind speed constant and purely radial, *i.e.*, $u_\phi=0$ and $u_r=u=450$ km/s, the radial and azimuthal positions in spherical coordinates of a certain parcel relative to a fixed point on the surface of the rotating Sun will be, respectively,

$$r(t)=R_\odot+ut \quad (2.36)$$

$$\phi(t)=-\Omega_\odot t+\phi_0 \quad (2.37)$$

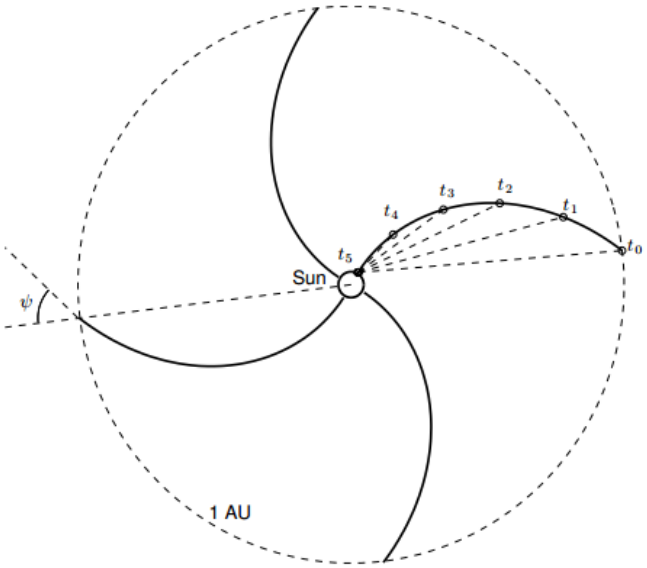

Figure 2.6: Spiral paths of solar wind parcels. (Hughes, 2016)

where $\Omega_\odot = 2.7\times10^{-6}$ rad s^{-1} is the mean angular velocity of solar rotation (Hundhausen, 2012) and ϕ_0 is a constant that specifies the longitude on the Sun's equator from which the parcel was launched. However, it is more useful to identify the shape of the path in space instead of the variation with time and for that it is necessary to solve Equation (2.37) in order of t and substitute it into Equation (2.36), which leads to

$$r = R_\odot - \frac{u}{\Omega_\odot}(\phi - \phi_0) \tag{2.38}$$

Equation (2.38) is the equation of an *Archimedean spiral*. In this context it is known as the *Parker's Spiral*, which is a simple approximation once it is not taken into to account the wind fluctuations after coronal projection. As seen before, the Sun's magnetic field is frozen into these plasma parcels and so, the IMF is expected to take the same shape. (Ambastha, 2020; Koskinen, 2011; Hughes, 2016; Vo, 2018)

The magnetic field must be parallel to the spiral on each of its points. A tangent vector $\mathbf{s}$ to the spiral is obtained from Equations (2.36) and (2.37), making $\mathbf{s} = \frac{\mathrm{d}r}{\mathrm{d}t}\hat{r} + r\frac{\mathrm{d}\phi}{\mathrm{d}t}\hat{\phi}$, which yields

$$\mathbf{s} = u\hat{\mathbf{r}} - r\Omega_\odot\hat{\phi} \tag{2.39}$$

As can be seen in Figure 2.6 it is possible to define an angle between an IMF field line and the Sun-Earth line. For that angle, ψ, Equation (2.39) allows to write that

$$\tan\psi = \frac{B_\phi}{B_r} = -\frac{r\Omega_\odot}{u} \tag{2.40}$$

Although The Parker's spiral gives the shape of the IMF, it is necessary to know its strength as a function of radial distance from the Sun. The equatorial IMF has both radial and azimuthal components that may be solved separately. The IMF must satisfy the Gauss' law for magnetism $\nabla\cdot\mathbf{B} = 0$ which, for spherical coordinates and assuming that $\partial B_\phi/\partial\phi = 0$,

yields

$$\nabla \cdot \mathbf{B} = \frac{1}{r^2}\frac{\mathrm{d}(r^2 B_r)}{\mathrm{d}r} = 0 \tag{2.41}$$

which by integration leads to

$$B_r(r) = B_0\left(\frac{R_\odot}{r}\right)^2 \tag{2.42}$$

for the radial component, with B_0 the magnetic field taken at the reference radius, *i.e.*, at $r = R_\odot$. Using Equation (2.40) it is possible to write the azimuthal component as

$$B_\phi(r) = -\frac{r\Omega_\odot}{u}B_r = -B_0\frac{R_\odot^2\Omega_\odot}{ur} \tag{2.43}$$

The strength of the IMF is then

$$B(r) = B_0\left(\frac{R_\odot}{r}\right)^2\sqrt{1+\left(\frac{\Omega_\odot r}{u}\right)^2} \tag{2.44}$$

From Equations (2.42) and (2.43) it can be seen that the radial component of the field decreases with r^{-2} and that the azimuthal component decreases with r^{-1} which is more slowly than the radial component, also explaining the spiral formation.

2.3 The Earth's Magnetosphere

The magnetosphere was defined by Gold (1959) as a region around the Earth where the geomagnetic field determines the motion of charged particles. It is essentially a magnetic cavity in the solar wind where the magnetic field of the Earth deflects the solar wind particles before they hit the surface of the planet. (Hughes, 2016; Koskinen, 2011)

The magnetosphere protects the Earth from the solar wind. The Earth's magnetosphere is dominated by three elements: the almost dipolar magnetic field originating inside the Earth, the IMF from the Sun and the solar wind properties. Where the IMF distorts the Earth's dipole, there is an electric current flowing. Each current system has a magnetic field topology associated with it, contributing to the global shape of the magnetosphere. Understanding the relative strength and location of each electric current system can help to accurately predict the variations of the magnetic field near the Earth's surface. The different main current systems in the magnetosphere are briefly described in Subsection 2.3.2. (Hughes, 2016; Koskinen, 2011)

The magnetic field measured on Earth is the result of several different sources, divided into three groups: Internal: dynamo effect caused by the currents in the Earth's outer core and remnant magnetization in the crust (Subsection 2.3.1); External: produced by currents in the magnetosphere and ionosphere (Subsection 2.3.2); Induced: produced by currents in the crust that are induced by the external magnetic fields. (Hughes, 2016; Koskinen, 2011)

2.3.1 The Earth's core

As said before, the Earth's magnetic field is the result of several different sources, being the dynamo-generated internal field 90% of it, which makes it the *main field*. Near the Earth surface it is basically a dipole, which is aligned off the rotation axis by about 10 degrees (Figure 2.7) and it is attributed to a dynamo mechanism of circulating current in its interior, by which a rotating, convecting, and electrically conducting fluid can maintain a magnetic field in astrophysical bodies. (Demorest, 2001; Hughes, 2016)

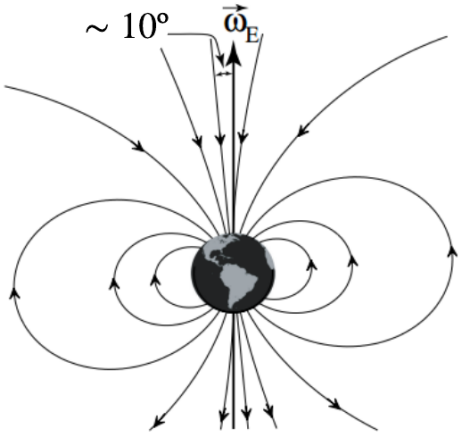

Figure 2.7: The Earth's magnetic field with the North geomagnetic pole located near the North geographic pole and the South geomagnetic pole located near the South geographic pole. (Hughes, 2016)

Convection drives the outer-core fluid which circulates relative to the solid container (the mantle). The electrically conducting material moves relative to the Earth's magnetic field and by Faraday's law a current is produced. Its magnetic field can sustain the primary magnetic dipole like field against Ohmic dissipation. (Demorest, 2001)

In short, the dynamo mechanism requires an electrically conducting fluid medium (liquid iron in the outer core), kinetic energy provided by planetary rotation (Coriolis force) and also by magnetic forces acting on the fluid (Lorentz force) and finally an internal energy source to drive convective motions within the fluid (the original heat resulting from the Earth's formation+). (Demorest, 2001)

2.3.2 Magnetospheric current systems

As the solar wind plasma reaches the the region close to the Earth it exerts a ram pressure (the pressure resulting from the exchange of linear momentum of the plasma bulk motion with magnetosphere), compressing the field on the dayside. This compression causes an increase in the field strength and magnetic pressure until the magnetic pressure equals the ram pressure. Then, the solar wind plasma flows around the magnetosphere creating a "tail" in the nightside, resulting in a magnetosphere that is compressed on the dayside and

elongated on the nightside. (Hughes, 2016; Koskinen, 2011)

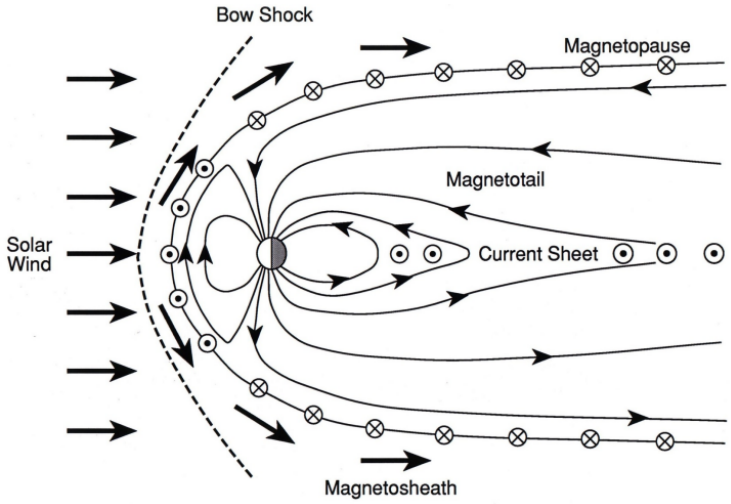

Figure 2.8: Cross section of the global magnetosphere through the day-night meridian, showing the magnetopause current system, the cusps, the magnetotail, and the magnetotail current sheet. Image taken from https://tinyurl.com/y74cf7qp.

The Magnetopause (Figure 2.8) is the surface boundary between the magnetosphere and the solar wind. It moves inward and outward as the solar wind intensity increases and decreases as explained before. Its location is determined by the balance between the pressure of the dynamic planetary magnetic field and the dynamic pressure of the solar wind bulk flow. This equilibrium can be defined by

$$P_{\text{ext}} = P_{\text{int}} \Leftrightarrow P_{\text{sw}} = P_{\text{Earth}} \tag{2.45}$$

where

$$\begin{cases} P_{\text{sw}} = \rho_{\text{sw}} u_{mp}^2 \\ P_{\text{Earth}} = \dfrac{B_{\text{mp}}^2}{2\mu_0} \end{cases} \tag{2.46}$$

so Equation (2.45) becomes

$$\rho_{\text{sw}} u_{mp}^2 = \frac{B_{\text{mp}}^2}{2\mu_0} \Leftrightarrow B_{\text{mp}} = u_{mp}\sqrt{2\mu_0\rho_{\text{sw}}} \tag{2.47}$$

where ρ_{sw} is the mass density of the solar wind and B_{mp} and u_{mp} are the strength of the magnetic field and the solar velocity at the magnetopause nose. (Hughes, 2016; Koskinen, 2011)

Along with the magnetopause, it is also possible to see in Figure 2.8:

- Bow Shock: collisionless shock front formed upstream of the magnetosphere where a decrease in the plasma flow speed occurs. (Hughes, 2016; Koskinen, 2011)
- Magnetosheath: region between the bow shock and the magnetopause where the plasma flows are highly turbulent. (Hughes, 2016; Koskinen, 2011)

- Polar Cusps: high latitude regions in both hemispheres where magnetic field lines transition from dayside field lines to those that goes into the tail. They are elongated in latitude and longitude and they link the magnetopause to the inner magnetosphere and the underlying atmosphere. (Hughes, 2016)

- Magnetotail: region that has open field lines[1] and is characterized by plasma of low electron density and energy. (Hughes, 2016)

- Current Sheet: region of closed field lines near the center of the tail with high electron density and weaker magnetic field. (Hughes, 2016)

The solar wind interaction with the magnetosphere çdrives currents in the system (Figure 2.9) and these currents are the key to study magnetospheric physics. (Koskinen, 2011)

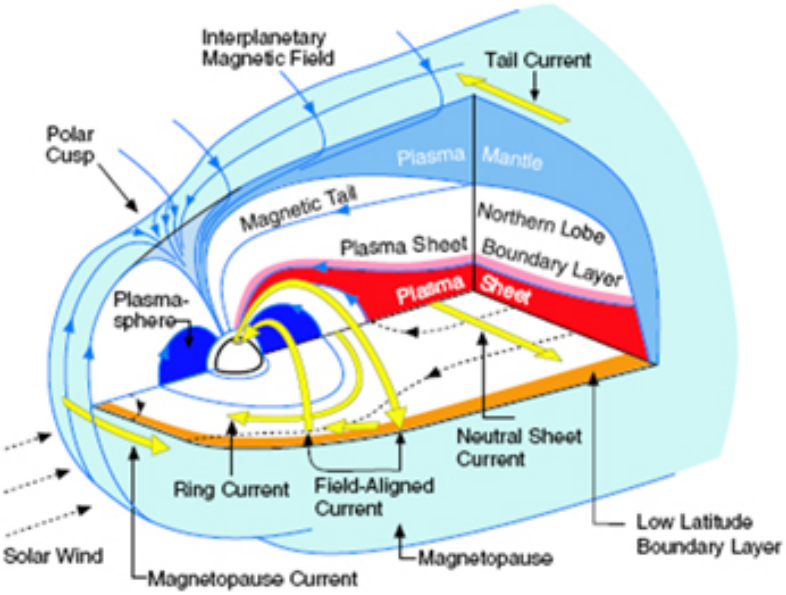

Figure 2.9: Solar wind interaction with Earth's magnetosphere. Image taken from https://tinyurl.com/y9byf4ea.

Magnetopause Current

In 1931 Chapman and Ferraro tried to explain how magnetic storms are driven by corpuscular radiation from the Sun by introducing the description of a magnetic cavity (magnetosphere) shielded from the solar wind by a current sheet (magnetopause current) (Koskinen, 2011; Lopez and Gonzalez, 2017). This current separates the geomagnetic field from the IMF in the magnetosheat and from the linear momentum equation $\rho \mathbf{u}_{mp} \cdot \nabla \mathbf{u}_{mp} = \mathbf{j} \times \mathbf{B}$ and the continuity equation $\nabla \cdot (\rho \mathbf{u}_{mp}) = 0$, in steady state, leads to

$$\mathbf{j}_{\mathrm{CF}} = \frac{\mathbf{B}_{\mathrm{mp}}}{B_{\mathrm{mp}}^2} \times \nabla P_{\mathrm{sw}} \tag{2.48}$$

[1] field lines that 'leave' or 'enter' Earth's surface from one hemisphere and do not connect to the other. Instead, they reconnect with the IMF some hundreds of R_E downstream from Earth. (Hughes, 2016)

also known as the *Chapman-Ferraro current*, where $\mathbf{B}_{\text{mp}}$ is the magnetic field at the magnetopause. The compression on the geomagnetic field caused by it can be seen in Figure 2.10.

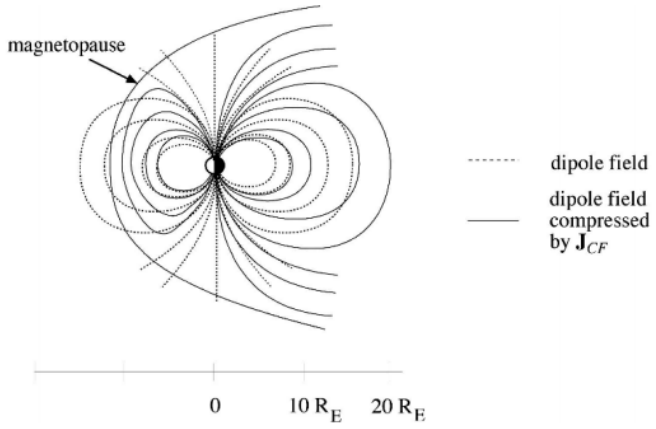

Figure 2.10: Compression of the geomagnetic field caused by the Chapman-Ferraro current. (Hughes, 2016)

Charged particles in the solar wind are deflected in opposite directions by the Earth's main field, creating a boundary current and because of that in the equatorial plane the current flows from dawn to dusk and at high-altitude it flows from dusk to dawn (Figure 2.11).

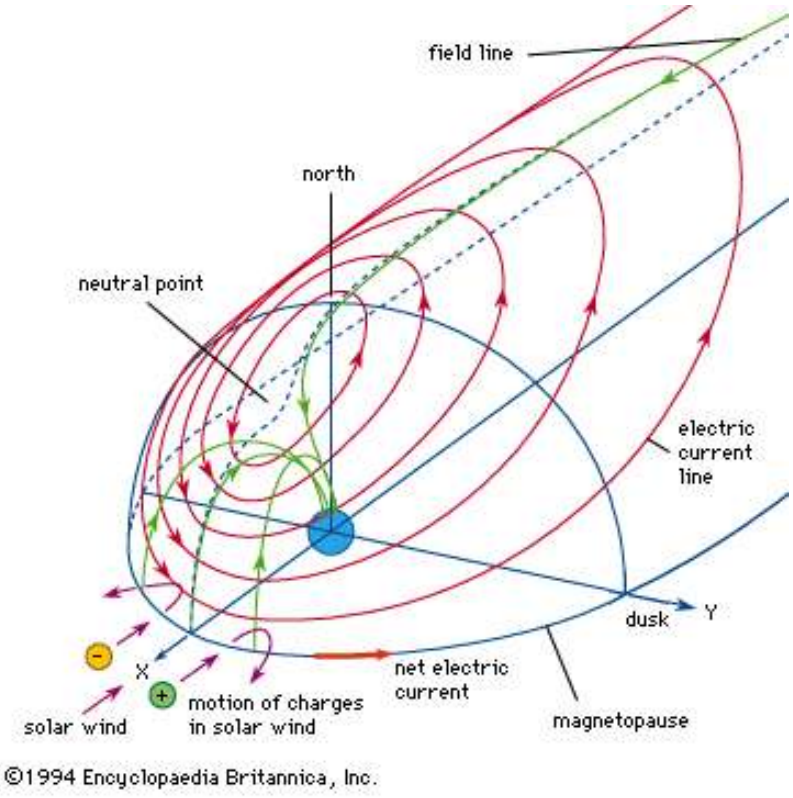

Figure 2.11: A perspective view of the northern portion of the magnetopause current, as seen from above the ecliptic plane. Image taken from https://tinyurl.com/y6urwa8f.

Magnetotail Current

The Magnetotail current is defined as nightside equatorial westward (from dawn to dusk) current outside $6.6R_E$ and that divides the magnetotail into two regions with almost uniform magnetic field of opposite direction, towards the Earth in the northern hemisphere and away from the Earth in the southern hemisphere. It closes on the magnetopause. (Ganushkina et al., 2018)

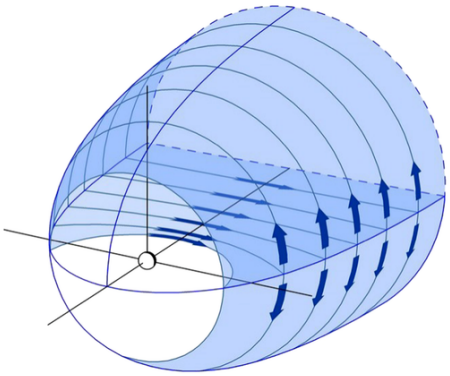

Figure 2.12: The tail current with closure via return currents on the magnetopause. (Ganushkina et al., 2018)

Field-aligned Currents

The Field-aligned currents (or Birkeland currents) are electric currents that flow along geomagnetic field lines. They connect the magnetospheric currents with ionospheric currents and are divided in two types: region 1 (or poleward currents) and region 2 (or equatorward currents). (Ganushkina et al., 2018)

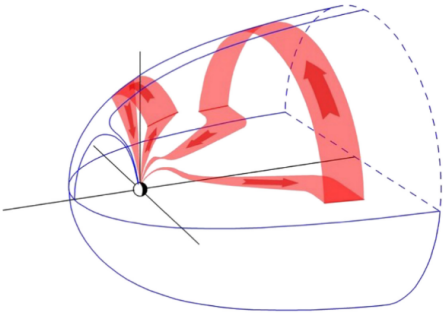

Figure 2.13: Region 1 field-aligned currents with two possible closure paths. (Ganushkina et al., 2018)

While Region 1 currents can close far at the tail (see Figure 2.13), Region 2 Field-aligned currents closes closer to the Earth, in the partial ring current on the nightside (Figure 2.14 (b)). They flow equatorward of the Region 1 currents, directed outward from the ionosphere near dusk and into the ionosphere around dawn.

Ring Current

The ring current is a current flowing around the Earth due to the drift of ions (westward) and electrons (eastward), with the shape of a ring. It lies at a distance of approximately 3 - $8R_E$ on the equatorial plane. The main contribution to its total density comes from the ions in the medium-energy range of $\sim$ 10 keV to a few hundreds of keV.

This current system is also divided in two:

- the symmetric ring current, that goes around the Earth in a closed loop and it flows eastward, i.e., clockwise (Figure 2.14 (a), brown region);
- the partial ring current (Figure 2.14 (b)) that is part of the westward ring current (Figure 2.14 (a), blue region) and its due to interactions between the solar wind and the magnetosphere, that results in an asymmetry of the plasma pressure distribution in the inner magnetosphere during disturbed times.

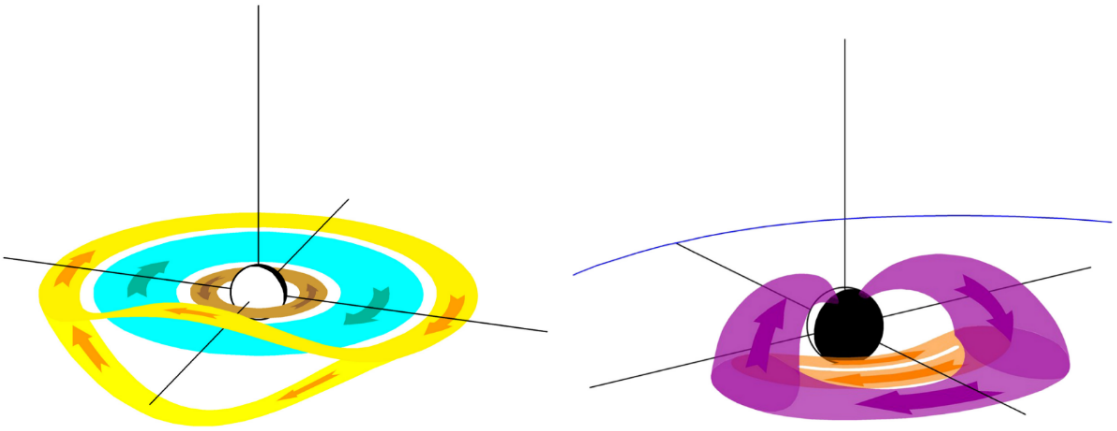

(a) Symmetric ring current

(b) Region 2 field-aligned current and partial ring current.

Figure 2.14: (a) Eastward symmetric ring current (brown disk) and symmetric part of the wesward ring current (blue disk); (b) partial ring current and Region 2 field-aligned current. (Ganushkina et al., 2018)

2.4 Geomagnetic Storms

Each of the current systems explained before has a magnetic field topology associated with it, contributing to the shape of the magnetosphere, so any changes in the solar activity will also change the geomagnetic field felt on Earth. In fact, the geomagnetic activity tends to be proportional to that of the solar activity, so as the Sun goes through its 11-year cycle, it has a 2 to 4 years of a peak (solar maximum) where the solar magnetic filed is most distorted. During this time, the solar activity is also at the peak, leading to a higher number of geomagnetic storms. (Bailey, 2018; Tsurutani and Gonzalez, 1997; Watari, 2017).

Geomagnetic storms are typically caused by a solar coronal mass ejection (CME), by a co-rotating interaction region (CIR) or by a high-speed stream of solar wind originated in

a coronal hole (Tsurutani and Gonzalez, 1997). The CMEs are the most important ones to the study of GICs since they have a higher geoeffectiveness when compared to CIRs, driving the majority of the GICs (Alves et al., 2006; Borovsky and Denton, 2006; Pulkkinen et al., 2017).

These storms are evaluated through geomagnetic activity indices that are helpful to quantify the irregular ground magnetic effects of the coupled ionospheric-magnetospheric currents driven by solar wind-magnetosphere energy transfer. This indices are explained in more detail in Section 4.1. Geomagnetic storm effects can lead to different phenomenon such as ionospheric disturbances that cause radio and radar scintillation, auroral displays at much lower latitudes than normal, disruption of navigation by magnetic compass and geomagnetically induced currents (GIC). (Bailey, 2018; Martini et al., 2016)

The different phases of the storms can be well identified most of the times and that allows to anticipate some of its effects. As satellite measurements give the information that a shock front of the CME approaches, it implies that a storm is coming and with it also an increase the risk of GICs, for instance.

GICs are a main topic in this manuscript, and will be treated in detail in Chapter 5.3, where estimates will be given for the southern Portuguese power network.

Chapter 3

Magnetotellurics

Magnetotellurics (MT) is a prospecting method that consists of probing the electric conductivity (σ) structure of the Earth, through the relation between the natural geomagnetic and natural geoelectric fields at the surface. Within this passive exploration technique, the electric and magnetic fields are measured simultaneously at a certain location and give us information about the electrical conductivity down to hundreds of kilometers. The first studies of MT started in the '40s by two Japanese researchers, but in fact, Tikhonov (1950) and Cagniard (1953) are the most known developers. (Simpson and Bahr, 2005; Blake, 2017)

The MT method measures the electromagnetic response of the Earth from different depths, depending on the type of ground (layer characteristics) at that location and on the period of the input signal.

The electromagnetic (EM) fields used for this method have several natural sources (Chapter 2) and their signal can be divided into two different categories: (Blake, 2017; Simpson and Bahr, 2005)

- $f < 1$ Hz: Low frequency signal due to the interaction between the solar plasma (streams of ions from solar storms) and the Earth's magnetosphere (Blake, 2017; Simpson and Bahr, 2005).
- $f > 1$ Hz: High frequency signal caused by lightning discharges in the Earth's ionosphere (Simpson and Bahr, 2005).

In the middle there is a gap, at $f \approx 1$Hz, because there are no sources of waves in this frequency, creating the *MT dead-band* (Figure 3.1). (Blake, 2017; Simpson and Bahr, 2005)

The EM fields naturally induced by the interactions described above have periods ranging from 10^{-3} to 10^{5}s. Each of these periods will have a different penetration depth, according to the average conductivity (σ) of the portion of land under study. This penetration

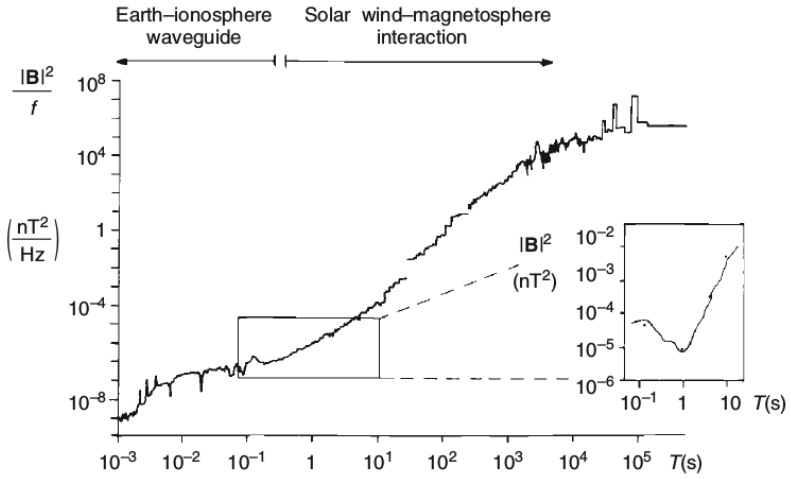

Figure 3.1: Power spectrum of natural magnetic variations. (Simpson and Bahr, 2005)

distance increases with the period (longer period implies greater depth and vice versa, as will be discussed in more detail in Subsection 3.2). (Simpson and Bahr, 2005)

The resistivity values (ρ) can vary for more than 6 orders of magnitude (from $\rho \leq 0.1$ Ωm till $\rho \geq 10^5$ Ωm), depending on the constitution of the soil (see Figure 3.2). It is just necessary a very small amount of water (few ppm) in the soil so that the electric resistivity decreases significantly as it supplies with hydrogen ions (H^+) which are mobile charge carriers (Simpson and Bahr, 2005). Having aqueous solutions within the soil, the resistivity will also depend on the temperature. If the temperature is increased, the resistivity of aqueous solutions decreases because the viscosity decreases, as it leads to a higher ion mobility. (Fantaye et al., 2011)

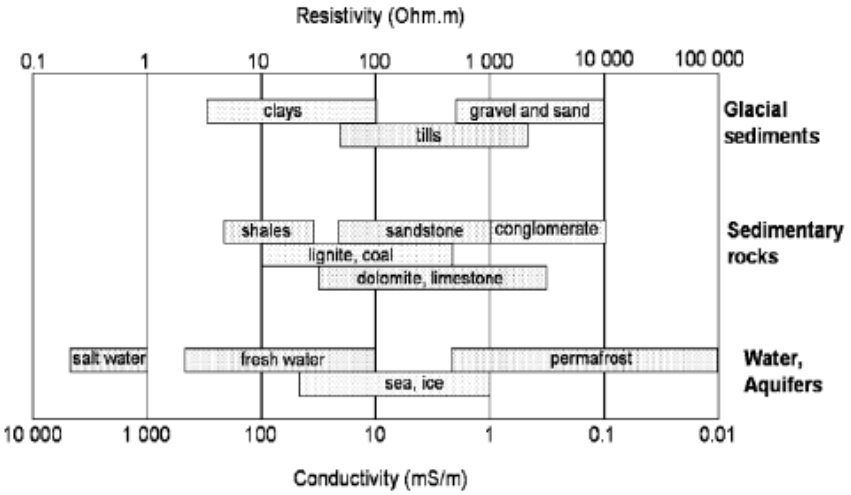

Figure 3.2: Range of values for electrical resistivity (ρ) and conductivity ($\sigma = 1/\rho$) for different types of soil/materials. (Syed et al., 2012)

3.1 MT method's assumptions

To use the MT method, one must take into account the EM induction in the Earth and follow the laws of Physics: (Simpson and Bahr, 2005; Blake, 2017)

(**a**) Maxwell equations for Electromagnetism:

- Faraday's law: establishes that a circulating electric field ($\mathbf{E}$) is produced by a time-varying magnetic field ($\mathbf{B}$):

$$\nabla \times \mathbf{E} = -\frac{\partial \mathbf{B}}{\partial t} \tag{3.1}$$

- Ampère-Maxwell's law: establishes that a circulating magnetic field is produced by an electric conduction current ($\mathbf{j}_f$) and by a variable electric displacement field ($\mathbf{D}$):

$$\nabla \times \mathbf{H} = \mathbf{j}_f + \frac{\partial \mathbf{D}}{\partial t} \tag{3.2}$$

  where $\mathbf{H} = \mathbf{B}/\mu$ and $\mathbf{E} = \mathbf{D}/\varepsilon$ for an isotropic and linear medium.

- Gauss' law for the magnetic field: indicates that the divergence of the magnetic field at any point is zero, i.e. there are no magnetic monopoles:

$$\nabla \cdot \mathbf{B} = 0 \tag{3.3}$$

- Gauss' law: establishes that the electric field created by an electric charge diverges from a positive charge and converges to a negative charge:

$$\nabla \cdot \mathbf{D} = \eta_f \tag{3.4}$$

  where η_f is the free charge density.

(**b**) The Earth works as a ohmic conductor, obeying Ohm's law: $\mathbf{j}_f = \sigma \mathbf{E}$.

Besides, one usually assumes that: (Simpson and Bahr, 2005; Blake, 2017)

(**i**) The Earth doesn't produce EM energy, it can only absorb and dissipate it;

(**ii**) Plane wave model: the natural sources of EM fields are taken as uniform EM waves, plane-polarized, generated at great distance from the Earth's surface, propagating towards Earth with an almost vertical incident angle (with exception for polar and equatorial regions due the complexity of the electrojet current that causes instabilities); (Miensopust, 2010)

(**iii**) The electric displacement field is approximated to quasi-static. That means that time-varying displacement currents ($\partial \mathbf{D}/\partial t$) are negligible compared with conduction currents ($\mathbf{j}_f$). This allows to treat EM induction on Earth as a diffusion process;

(**iv**) Variations of the conductivity (σ) of the bulk rocks are way more important than variations of the electrical permittivity (ε) and magnetic permeability (μ) of rocks which are assumed as being those of vacuum.

These laws and assumptions will be used in Section 3.2 below.

3.2 A simple analytical model – Half-Space

Starting with Maxwell equations as seen in Section 3.1 – Equations (3.1 to 3.4) and taking the assumption (iii) into account (i.e. assuming that time-varying displacement currents are negligible):

$$\frac{\partial \mathbf{D}}{\partial t} = 0 \Rightarrow \nabla \times \mathbf{H} = \mathbf{j}_f \tag{3.5}$$

As mentioned before, Gauss law for the magnetic field says that there are no magnetic monopoles. Besides, for an isotropic and linear medium and having in mind the assumption (iv) that states that $\mu \equiv \mu_0$ and $\varepsilon \equiv \varepsilon_0$:

$$\mathbf{B} = \mu \mathbf{H} \Rightarrow \mathbf{B} = \mu_0 \mathbf{H} \tag{3.6a}$$

$$\mathbf{D} = \varepsilon \mathbf{E} \Rightarrow \mathbf{D} = \varepsilon_0 \mathbf{E} \tag{3.6b}$$

Applying these equations along with Ohm's law, Maxwell's laws can be rewritten as:

$$\nabla \times \mathbf{E} = -\frac{\partial \mathbf{B}}{\partial t} \tag{3.7a}$$

$$\nabla \times \mathbf{B} = \mu_0 \sigma \mathbf{E} \tag{3.7b}$$

$$\nabla \cdot \mathbf{B} = 0 \tag{3.7c}$$

$$\nabla \cdot \mathbf{E} = \frac{\eta_f}{\varepsilon_0} \tag{3.7d}$$

and from assumption (i) (no current or charge sources) it comes:

$$\nabla \cdot \mathbf{j}_f = 0 \tag{3.8}$$

This is shown below, considering the case of a homogeneous *half-space*[1], ($\nabla \sigma = 0$):

$$\nabla \cdot \mathbf{j}_f = \nabla \cdot (\sigma \mathbf{E}) = \sigma \nabla \cdot \mathbf{E} \; + \; \mathbf{E} \cdot \nabla \sigma = \sigma \nabla \cdot \mathbf{E} = \sigma \frac{\eta_f}{\varepsilon_0} = 0 \tag{3.9}$$

For the Earth case, let's consider an external magnetic field inducing an electric field. From Equations (3.7a) and (3.7b),

$$\begin{aligned} \nabla \times (\nabla \times \mathbf{E}) =& \nabla(\nabla \cdot \mathbf{E}) - \nabla^2 \mathbf{E} = -\frac{\partial}{\partial t}(\nabla \times \mathbf{B}) \\ \Leftrightarrow & \nabla^2 \mathbf{E} = \mu_0 \sigma \frac{\partial \mathbf{E}}{\partial t} \end{aligned} \tag{3.10}$$

which takes the form of a diffusion equation. Taking assumption (ii) into account, i.e. plane wave model, and considering an electromagnetic wave propagating with wave functions that can be expressed as

$$\mathbf{E} = \; \mathbf{E}_0 e^{i\omega t - kz} \tag{3.11a}$$

$$\mathbf{B} = \; \mathbf{B}_0 e^{i\omega t - kz} \tag{3.11b}$$

[1] Defined by Simpson and Bahr (2005) as a "*mathematical model in which only one boundary exists, all the others being infinitely far away. The medium under consideration is usually assumed to be perfectly homogeneous and isotropic.*"

where k is the wave number. Then Equation (3.10) can be rewritten as:

$$\nabla^2 \mathbf{E} = i\omega\mu_0\sigma\mathbf{E} \tag{3.12}$$

in the same way it comes that:

$$\nabla^2 \mathbf{B} = \mu_0\sigma\frac{\partial \mathbf{B}}{\partial t} \Rightarrow \nabla^2 \mathbf{B} = i\omega\mu_0\sigma\mathbf{B} \tag{3.13}$$

In the air, the conductivity is close to zero ($\sigma \to 0$), hence the external EM fields are weakly attenuated by the air layer between the ionosphere and the Earth's surface. This means that MT works with EM energy that diffuses through the Earth. (Simpson and Bahr, 2005).

Equations (3.12) and (3.13) are second-order differential equations with general solutions of the form:

$$\mathbf{E} = \mathbf{E}_1 e^{i\omega t - qz} + \mathbf{E}_2 e^{i\omega t + qz} \tag{3.14a}$$
$$\mathbf{B} = \mathbf{B}_1 e^{i\omega t - qz} + \mathbf{B}_2 e^{i\omega t + qz} \tag{3.14b}$$

where q refers to the penetration of the wave into the ground, as shown below.

Taking into account that the Earth doesn't produce energy, only absorbs and dissipates it, it comes that $\mathbf{E}_2 = 0$ and $\mathbf{B}_2 = 0$, *i.e.*, the fields must vanish when $z \to \infty$.

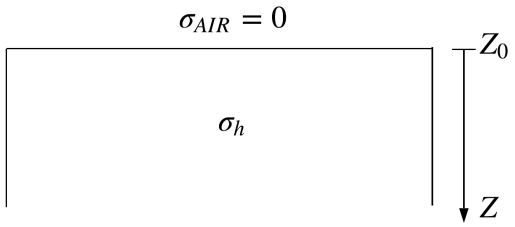

Figure 3.3: Schematic model of the *half-space* model: an air layer with zero conductivity overlapping to a layer with an homogeneous conductivity, σ_h. (Simpson and Bahr, 2005)

The *half-space* model is simply an air layer with zero conductivity overlapping an infinite medium $z > 0$, with an homogeneous conductivity σ_h, which means $\frac{\partial \mathbf{E}}{\partial x} = \frac{\partial \mathbf{E}}{\partial y} = 0$ and $\frac{\partial \mathbf{B}}{\partial x} = \frac{\partial \mathbf{B}}{\partial y} = 0$. It is now possible to take the second derivative of Equation (3.14a),

$$\nabla^2 \mathbf{E} = \frac{\partial^2 \mathbf{E}}{\partial z^2} = q^2 \mathbf{E}_1 e^{i\omega t - qz} \Leftrightarrow \nabla^2 \mathbf{E} = q^2 \mathbf{E} \tag{3.15}$$

From Equation (3.12) it comes:

$$i\omega\mu_0\sigma_h\mathbf{E} = q^2\mathbf{E} \Leftrightarrow \; q = \sqrt{i\omega\mu_0\sigma_h} = (1+i)\sqrt{\frac{\omega\mu_0\sigma_h}{2}} \tag{3.16}$$

The inverse of the real part of q is known as the electromagnetic *skin depth*: the depth at

which an EM wave having angular frequency ω will penetrate into a medium with electric conductivity σ_h, before its amplitude is attenuated by a factor of $1/e$ and it is given by: (Blake, 2017; Simpson and Bahr, 2005)

$$\delta(\omega) = \sqrt{\frac{2}{\omega\mu_0\sigma_h}} \tag{3.17}$$

This equation shows that for higher frequencies the skin depth is smaller, meaning that to study deeper layers it will be necessary EM waves with smaller frequencies. (Blake, 2017; Simpson and Bahr, 2005)

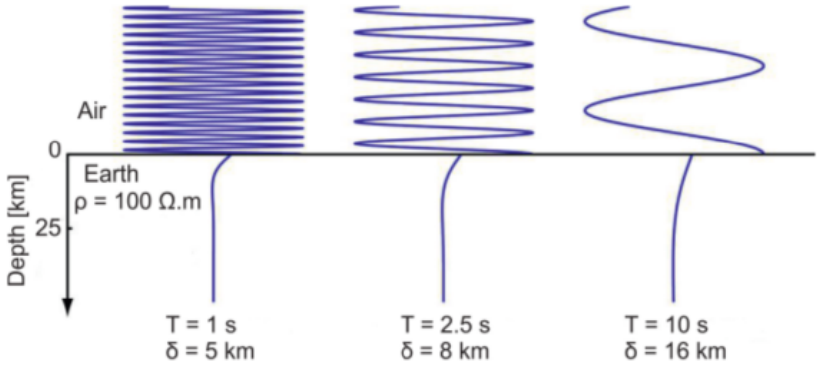

Figure 3.4: Example for the penetration of different frequencies according to Equation (3.17). (Alves Ribeiro, 2018)

Using $\mu_0 = 4\pi \times 10^{-7}$ H/m and $\rho_h = \frac{1}{\sigma_h}$, Equation (3.17) can also be written (in m): (Thiel, 2008)

$$\delta(T) \approx 500\sqrt{T\rho_h} \tag{3.18}$$

where $T = 2\pi/\omega$ is the period in [s]. This equation stipulates that the skin depth δ is both dependent on the magnitude of the conductivity of the overlying material and the period range used (Thiel, 2008).

Knowing that for a homogeneous Earth, $E_x = E_{x1}e^{i\omega t - qz}$ and $B_y = B_{y1}e^{i\omega t - qz}$, it comes from Equation (3.7a) that $qE_x = i\omega B_y$ and $qE_y = -i\omega B_x$. It is possible to write the relation between electric field and magnetic field components as:

$$C = \frac{E_x}{i\omega B_y} = -\frac{E_y}{i\omega B_x} = \frac{1}{q} \tag{3.19}$$

where C is a complex transfer function named *Schmucker-Weidelt function*.

Taking Equation (3.16) and knowing that $\rho = 1/\sigma$ it comes:

$$\rho_h = \frac{1}{\sigma_h} = \frac{1}{|q|^2}\mu_0\omega \Leftrightarrow \rho_h = |C|^2\mu_0\omega \tag{3.20}$$

which give us the resistivity of the *half-space* in terms of the Schmucker-Weidelt transfer function (ρ_h in [Ωm]). (Blake, 2017; Simpson and Bahr, 2005; Thiel, 2008)

An angle is also defined, the impedance phase, as

$$\phi = \arg \frac{E_x}{B_y} = \arg C + \frac{\pi}{2} \tag{3.21}$$

As a reference value ϕ, one can consider the half-space conductivity model. From Equation (3.16) it comes that

$$\arg q = \arg(1+i) = \frac{\pi}{4} \tag{3.22}$$

which implies that, from Equation (3.19),

$$\arg C = \arg\left(\frac{1}{q}\right) = -\frac{\pi}{4} \tag{3.23}$$

leading to

$$\phi = \frac{\pi}{4} \tag{3.24}$$

3.3 MT impedance tensor – Dimensionality

The MT impedance tensor $\mathbf{Z}$ relates the electric and magnetic fields at a certain location on the Earth's surface according to:

$$\mathbf{E}(\omega) = \frac{1}{\mu_0}\mathbf{Z}(\omega)\mathbf{B}(\omega) \Leftrightarrow$$

$$\Leftrightarrow \begin{pmatrix} E_x(\omega) \\ E_y(\omega) \end{pmatrix} = \frac{1}{\mu_0} \begin{pmatrix} Z_{xx}(\omega) & Z_{xy}(\omega) \\ Z_{yx}(\omega) & Z_{yy}(\omega) \end{pmatrix} \begin{pmatrix} B_x(\omega) \\ B_y(\omega) \end{pmatrix} \tag{3.25}$$

The impedance tensor ($\mathbf{Z}$) has information not only on the resistivity of the soil but also on the dimensionality and direction of the fields (Blake, 2017) (Simpson and Bahr, 2005). For each element of the impedance tensor $\mathbf{Z}$, the apparent resistivity and impedance phase are, respectively:

$$\begin{cases} \rho_{ij} = \dfrac{1}{\mu_0 \omega}|Z_{ij}|^2 \\ \phi_{ij} = \arctan\left(\dfrac{\mathrm{Im}(Z_{ij})}{\mathrm{Re}(Z_{ij})}\right) \end{cases}$$

Depending on the dimensionality of the conductivity model, the impedance tensor has different symmetry properties (Figure 3.5). The four different types of conductivity models are: The *Homogeneous Half-Space* model, that has already been considered in Section 3.2, *The Layered Earth* – 1D Model, (subsection 3.3.2), the *2D Earth* model and the *3D Earth* model (subsection 3.3.4).

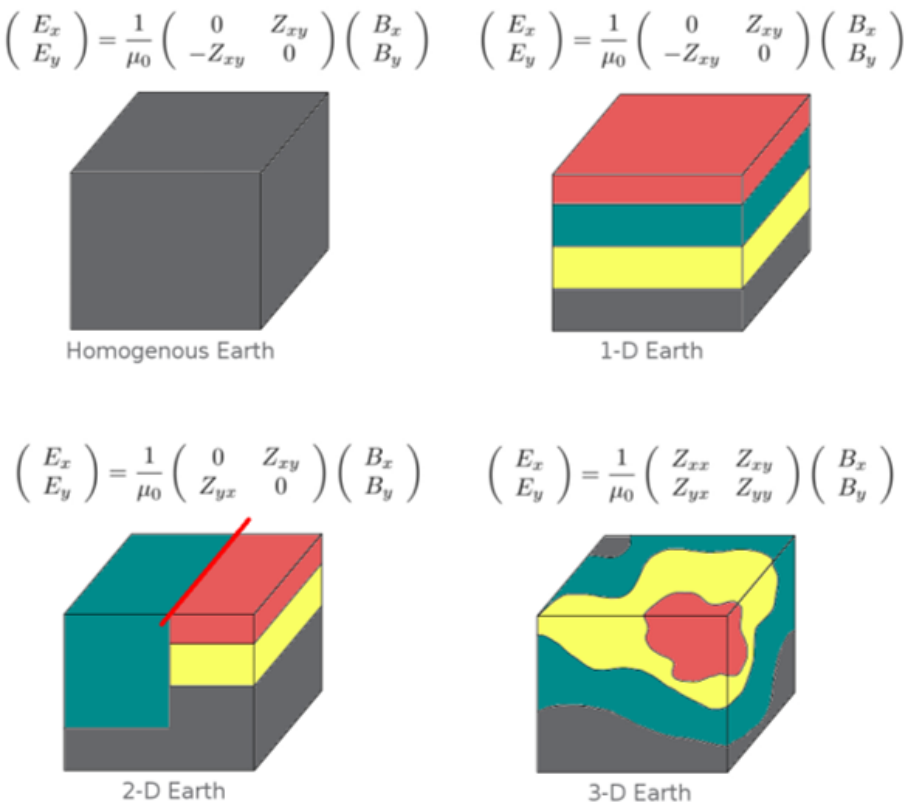

Figure 3.5: The four different models for MT studies when considering different symmetries and its consequences on the impedance tensor. Each color stands for different resistivities. (Blake, 2017)

3.3.1 Homogeneous Half-Space Model

Applying Equations (3.16) and (3.19) to Equation (3.25) it comes

$$Z_{xx} = Z_{yy} = 0 \text{ and } Z_{yx} = -Z_{xy} \tag{3.26}$$

with

$$Z_{yx} = -\frac{i\omega\mu_0}{q} = -i\omega\mu_0 C \Leftrightarrow Z_{xy} = i\omega\mu_0 C \tag{3.27}$$

3.3.2 1D Model – Layered Earth

In this model it is considered a layered Earth where each layer has a certain conductivity, i.e. the conductivity values only vary with depth and not horizontally (Fig. 3.6), (Blake, 2017)

$$\frac{\partial}{\partial x} = \frac{\partial}{\partial y} = 0 \tag{3.28}$$

This means that, in each layer n, the equations relating $\mathbf{E}$ and $\mathbf{B}$ are the same as those obtained in Section 3.2.

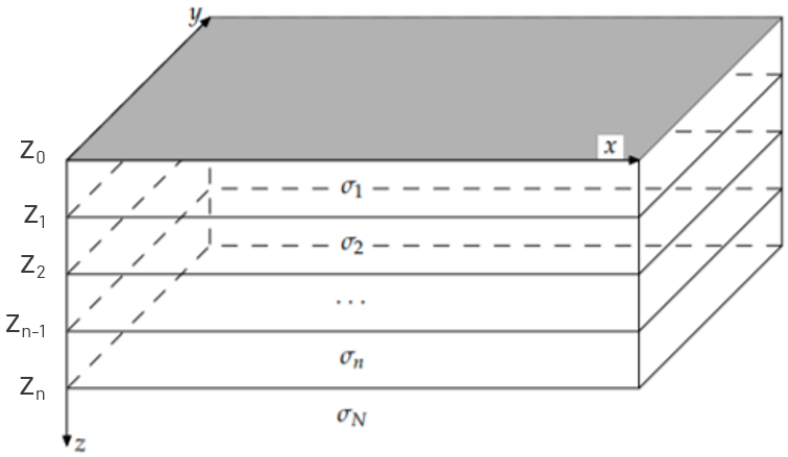

Figure 3.6: Schematic of a 1D model: Layered Earth with σ varying in the z-direction. (Thiel, 2008)

In order to calculate the impedance tensor for this model, considering that the Earth has N layers each with a resistivity ρ_n, one must start by writing for each layer (see Section 3.2),

$$\begin{cases} C_n(z) = \dfrac{E_{xn}(z)}{i\omega B_{yn}(z)} \\ q_n = \sqrt{i\omega\mu_0\sigma_n} \end{cases} \tag{3.29}$$

Being $C_n(z_n - 1)$ and $C_n(z_n)$ the transfer functions at the top and bottom of the n^{th} layer, respectively (see Figure 3.6), it can be derived from Equations (3.29) that

$$C_n(z_{n-1}) = \frac{1}{q_n} \frac{q_n C_n(z_n) + \tanh[q_n(z_n - z_{n-1})]}{1 + q_n C_n(z_n) \tanh[q_n(z_n - z_{n-1})]} \tag{3.30}$$

At the transition between the n^{th} and $(n+1)^{\text{th}}$ layer, the field components and, subsequently, the *Schmucker-Weidel transfer functions* are assumed to be continuous. It then follows that $C_n(z_n) = C_{n+1}(z_n)$ and substituting $l_n = z_n - z_{n-1}$ into Equation (3.30) yields: (Simpson and Bahr, 2005)

$$C_n(z_{n-1}) = \frac{1}{q_n} \frac{q_n C_{n+1}(z_n) + \tanh(q_n l_n)}{1 + q_n C_{n+1}(z_n) \tanh(q_n l_n)} \tag{3.31}$$

This equation, known as *Wait's recursion formula*, can be used to calculate the transfer C function at the top of the nth layer. In order to do that it is necessary to know the transfer function at the top of the $(n+1)$th layer. As been said before, using Wait's recursion formula and through $(N-1)$ iterations, it is possible to obtain the transfer function at the Earth's surface from the transfer function at the top of the lowermost layer N.This gives the relation between the components of the electric and magnetic fields at the Earth surface:

$$C_1(Z_0) = \frac{E_x(Z_0)}{i\omega B_y(Z_0)} = -\frac{E_y(Z_0)}{i\omega B_x(Z_0)} \tag{3.32}$$

It is now possible to define *apparent resistivity* as the average resistivity of an equivalent

uniform half-space, by analogy with to Equation (3.20):

$$\rho_a = |C_1(Z_0)|^2 \mu_0 \omega \tag{3.33}$$

The diagonal elements of the impedance tensor in Equation (3.25) are zero ($Z_{xx} = Z_{yy} = 0$) and the other two elements have the same magnitude but opposite signs ($Z_{xy} = -Z_{yx}$) (Blake, 2017; Simpson and Bahr, 2005). Therefore, Equation (3.25) becomes, for each layer:

$$\begin{pmatrix} E_x \\ E_y \end{pmatrix} = \frac{1}{\mu_0} \begin{pmatrix} 0 & Z_{xy} \\ -Z_{xy} & 0 \end{pmatrix} \begin{pmatrix} B_x \\ B_y \end{pmatrix} \tag{3.34}$$

where $Z_{xy} = i\omega\mu_0 C_1(Z_0)$.

3.3.3 2D Earth Model

This model is typically used to represent regions with distinct conductivities along only one of the horizontal directions and with depth. This discontinuity may occur along a geologival fault or dyke. Assuming that the conductivity is constant along the x-axis (called a geo-electric strike) it comes $\frac{\partial \mathbf{B}}{\partial x} = \frac{\partial \mathbf{E}}{\partial x} = 0$ and implies that, from Maxwell's Equations ($\nabla \times \mathbf{E} = -i\omega\mathbf{B}$ and $\nabla \times \mathbf{B} = \mu_o \sigma \mathbf{E}$),

$$\begin{cases} \dfrac{\partial E_x}{\partial y} = i\omega B_z \\ \dfrac{\partial E_x}{\partial z} = -i\omega B_y \\ \dfrac{\partial B_z}{\partial y} - \dfrac{\partial B_y}{\partial z} = \mu_0 \sigma E_x \end{cases} \tag{3.35}$$

$$\begin{cases} \dfrac{\partial B_x}{\partial y} = -\mu_0 \sigma E_z \\ \dfrac{\partial B_x}{\partial z} = \mu_0 \sigma E_y \\ \dfrac{\partial E_z}{\partial y} - \dfrac{\partial E_y}{\partial z} = -i\omega B_x \end{cases} \tag{3.36}$$

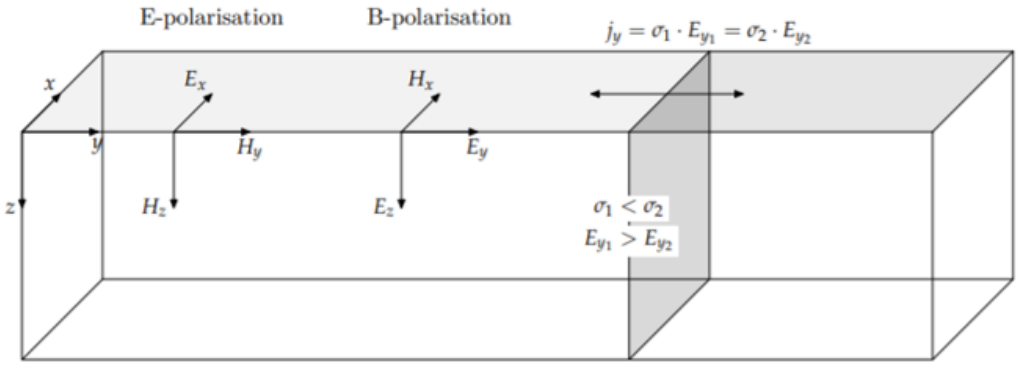

Figure 3.7: Schematic of a 2D model with a lateral contact striking in the x-direction. In the y-direction there are a boundary separating two regions with different conductivities. (Thiel, 2008)

As can be seen above, it is possible to decompose the previous equations into two modes, depending on how the fields are aligned:

- E-polarisation or Transverse Electric Mode (TE mode): once the E-field is parallel to the strike (Equations (3.35));
- B-polarisation or Transverse Magnetic Mode (TM mode): once the B-field is parallel to the strike (Equations (3.36));

The discontinuity in the conductivities is responsible for a jump in the electric field normal to the boundary (E_y in Figure 3.7). The tangential components of the electric field are continuous (E_x and E_z). So, as a result, in the TE mode there is no discontinuous behavior in the curve of apparent resistivity and impedance phase when going through the vertical wall. In the TM mode, a discontinuity is visible and helps to locate the strike. (Thiel, 2008)

3.3.4 3D Earth Model

In a 3D model the process is by far more complicated once it is the real situation, which means that the conductivity values vary with depth and both horizontal directions (Blake, 2017; Simpson and Bahr, 2005), implying that all the components of the electric and magnetic field are related among them (Thiel, 2008). Therefore, the impedance tensor becomes:

$$\begin{pmatrix} E_x \\ E_y \end{pmatrix} = \frac{1}{\mu_0} \begin{pmatrix} Z_{xx} & Z_{xy} \\ Z_{yx} & Z_{yy} \end{pmatrix} \begin{pmatrix} B_x \\ B_y \end{pmatrix}$$

Since the conductivity distribution fluctuates with the three dimensions, the impedance tensor will not have any diagonal elements approaching zero. In another words, all the components of the impedance tensor are nonzero. (Miensopust, 2010)

	Dimensionality		
	1-D	2-D	3-D
tensor components	$Z_{xx} = Z_{yy} = 0$ $Z_{xy} = -Z_{yx}$	$Z_{xx} = -Z_{yy}$ $Z_{xy} \neq -Z_{yx}$	$Z_{xx} \neq -Z_{yy} \neq Z_{xy} \neq Z_{yx}$
impedance tensor Z	$\begin{pmatrix} 0 & Z_n \\ -Z_n & 0 \end{pmatrix}$	$\begin{pmatrix} 0 & Z_\parallel \\ Z_\perp & 0 \end{pmatrix}$	$\begin{pmatrix} Z_{xx} & Z_{xy} \\ Z_{yx} & Z_{yy} \end{pmatrix}$

Figure 3.8: Impedance tensor **Z** *vs* dimensionality and isotropic conductivity distribution. (Thiel, 2008)

Figure 3.8 summarizes the impedance tensor properties for the 1D, 2D and 3D cases. For the 2D case, the diagonal zeros only apply when x (or y) direction is aligned along electromagnetic strike and then $Z_\parallel$ and $Z_\perp$ are the TE mode and TM mode impedances, respectively. In a real situation the diagonal impedance tensor will never be zero because of the data errors in the inductive response. (Simpson and Bahr, 2005; Thiel, 2008)

There are several kinds of dimensionality analysis of the impedance tensor that allow to determine the dimensionality of the structure under investigation, thus allowing to decide what is the best approach to follow (1D, 2D or 3D models).

3.4 Data Acquisition

As stated before, the MT method measures the natural variations on the Earth's surface of the electric and magnetic fields in order to deduce the electrical resistivity structure in the subsurface (Fantaye et al., 2011). In order to make the measurements, the following equipment is required (see Fig.(3.9)): 5 electrodes buried in the ground to measure the electric field (four for E_x and E_y – 2 perpendicular dipoles – and one to ground the data logger) and 3 induction coils to measure the magnetic field: for H_x, H_y and H_z. (Simpson and Bahr, 2005; Fantaye et al., 2011)

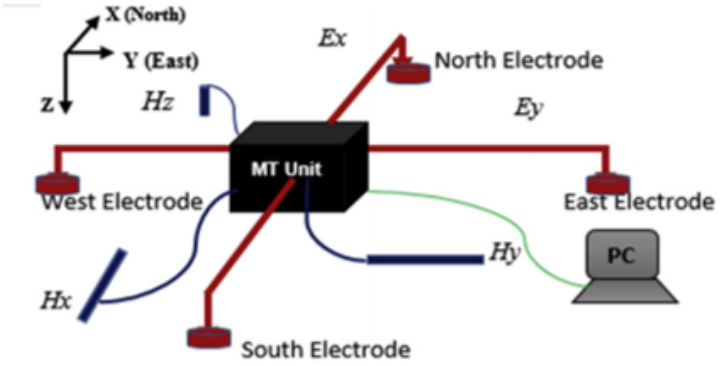

Figure 3.9: Magnetotelluric method's typical setup with the magnetic field measured in three orthogonal directions (x, y, z) and the electrodes aligned with magnetic north-south and east-west directions. (Cherkose and Mizunaga, 2018)

The time-varying **B** field is the primary source and propagates through the Earth's surface and subsurface. Along with its propagation it induces an electric field, **E**, which spreads in depth. The two halves of the coils' cores will have equal and opposite magnetic fields induced by the alternating currents. If there is no external magnetic field, those which are induced will cancel causing no flux variations. On the other hand, adding an external field will cause a saturation in the direction of that field leading to a net change of flux, inducing a voltage that will be proportional to the strength of the external magnetic field (Blake, 2017). As for the electric field components, their values are set by measuring the potential difference, U, between pairs of electrodes and will be proportional to it:

$$E = \frac{U}{d} \tag{3.37}$$

with $d = 10$ to 100 m being the distance between electrodes.

Temperature fluctuations can influence the results so, in order to minimize that, the magnetometer is typically buried at $\approx$ 90 cm into the ground and the electrodes at $\approx$ 1 m (Blake, 2017; Simpson and Bahr, 2005). Another thing to have into account during data acquisition is the sources of noise that can perturb the results. In order to mitigate these

effects it is necessary to choose the ideal location for the setup having attention that they may be caused mainly by human interference through DC train lines, electric fences, power lines and mining activity. (Miensopust, 2010)

3.5 Data Processing

During a MT campaign a large quantity of data is collected and there is the need to interpret it. This data consists in information about periods and, consequently, about penetration depths. The best way to process these data is through an iterative process in the frequency domain which requires creating a time series x_j by sampling a signal x(t) at equal intervals of time Δt, from $j = 1$ to N, where $T_0 = (N-1)\Delta t$ is the duration of the signal (Travassos and Beamish, 1988). All these methods/techniques used in order to go from time series to spectral information in the frequency domain result in a Fourier transformation (Simpson and Bahr, 2005). Within spectral analysis of time series there are several methods (Travassos and Beamish, 1988), such as:

- Fourier Harmonic Analysis: The time series of length T_0 is cyclic or periodic with fundamental period T_0 so that $x(t) = x(t + T_0)$.

- Fourier Transient Analysis: Fourier transform for the time series over all time and not just for a periodic interval.

- Power Spectral Analysis: Fourier transform of the auto-correlation or cross-relation function in the time domain.

- Band-pass filtering: Allows to analyze the data as a function of time enabling to select the sections with high or low signal and not making a raw average of it all.

3.6 Real applications of the MT method – original analysis

In this section some examples of impedance matrices will be given for one-dimensional models as described in Section 2.4. Several examples are discussed in order to understand the behavior of the signal through the ground considering different depths and resistivities.

3.6.1 1D Model - Layered Earth

For a one-dimensional Earth conductivity model, I have used Pethick (1999) code (Figure 3.10). It allows to model the response of 1D Earth for different layer depths on a given frequency interval. These results can be seen for different study cases in Figures 3.11 to 3.13.

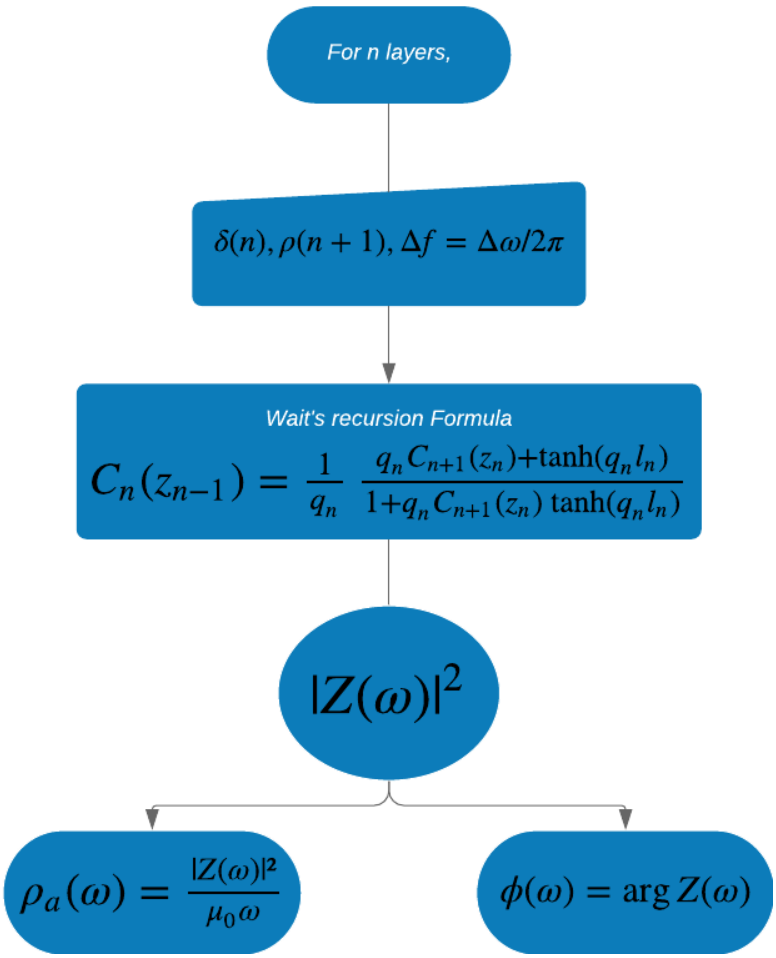

Figure 3.10: Flowchart for Pethick (1999) code to model 1D Layered Earth.

As can be seen in Figure 3.10, using the equations of Section 3.3.2, the calculation of the impedance tensor is followed by the calculation of the respective apparent resistivity and phase, with values in the plots of Figures 3.11 to 3.13 shown as red and blue lines, respectively. From Section 3.2, Equation (3.17) can be rewritten as:

$$\omega = \frac{\rho}{2\pi \times 10^{-7}\sigma^2} \Leftrightarrow f = \frac{\rho}{4\pi^2 \times 10^{-7}\delta^2} \tag{3.38}$$

and it is possible to infer a theoretical value for the frequency above which all EM signals are absorbed in the upper layer of thickness δ. This value is shown in the Figures 3.11 to 3.13 as the green dashed line.

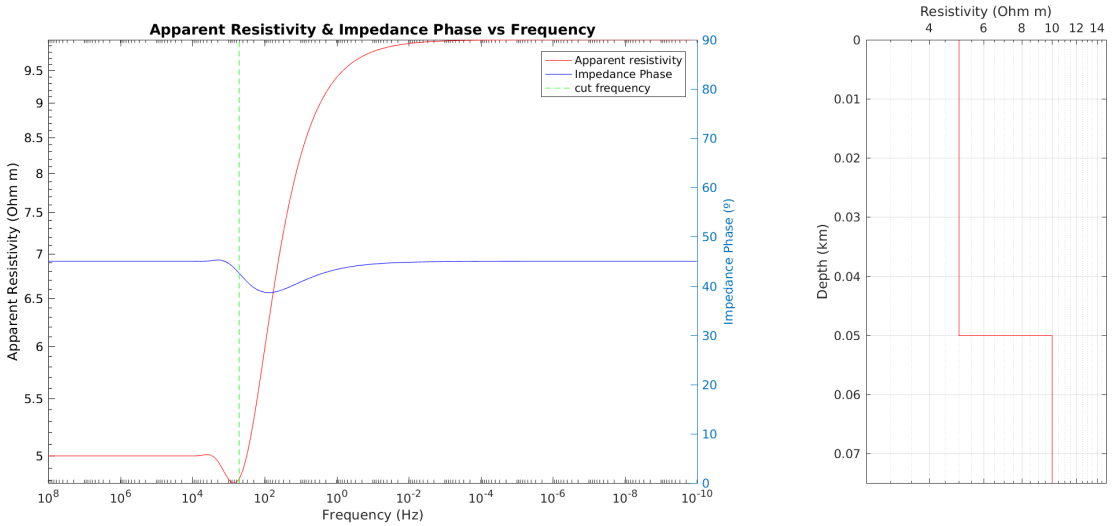

(a) Layer 1: $\rho = 5$ Ωm and $z = 50$ m; Layer 2: $\rho = 10$ Ωm and $z = \infty$

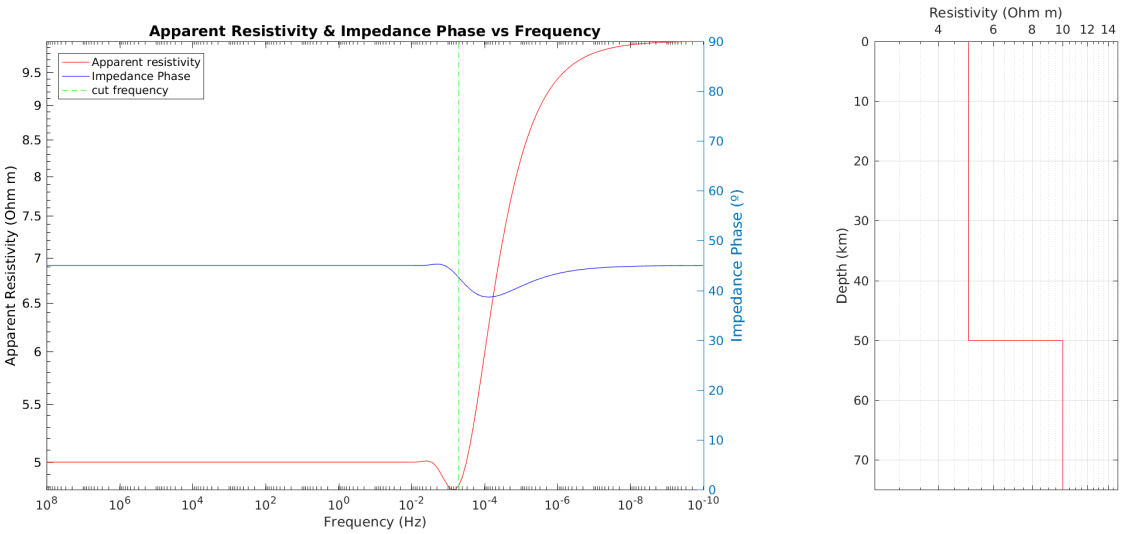

(b) Layer 1: $\rho = 5$ Ωm and $z = 50$ km; Layer 2: $\rho = 10$ Ωm and $z = \infty$

Figure 3.11: Plot for 1D-model using Pethick (1999) code with two layers. The two plots have the same values for the resistivity but different depths. The resistivity for both cases increases with depth.

Figure 3.11 shows the difference on the behavior of the frequency response for the same resistivity but different values for the first layer thickness. The plots on this figure also show the impedance phase variation along the frequency. Regarding the apparent resistivity it is seen that for a larger top layer with the same resistivity, low frequencies are totally absorbed while for a smaller one, it only absorbs high frequencies. The impedance phase is smaller than 45º for frequencies that 'see' the transition between the two layers.

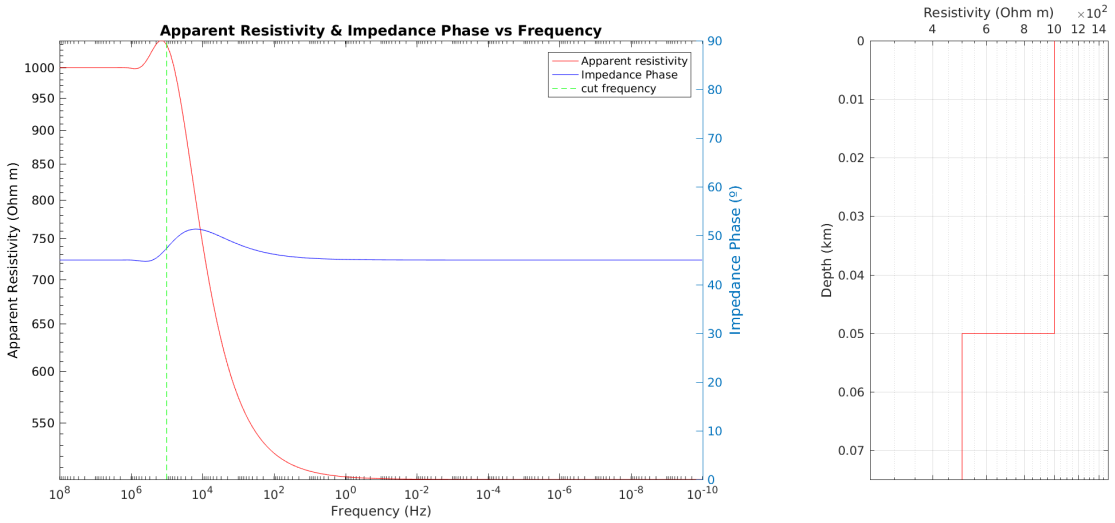

(a) Layer 1: $\rho = 1000$ Ωm and $z = 50$ m; Layer 2: $\rho = 500$ Ωm and $z = \infty$

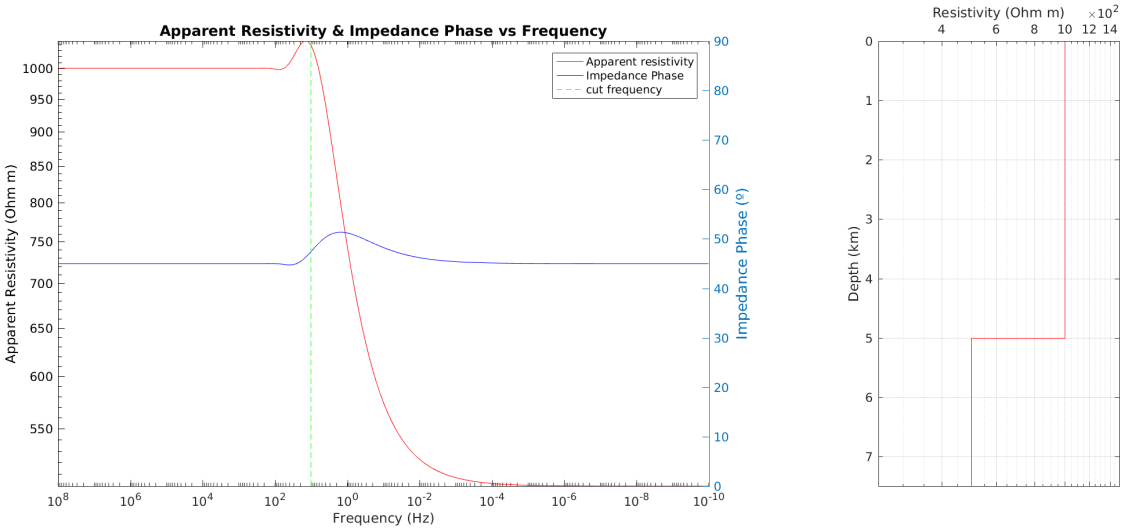

(b) Layer 1: $\rho = 1000$ Ωm and $z = 5$ km; Layer 2: $\rho = 500$ Ωm and $z = \infty$

Figure 3.12: Plot for 1D model using Pethick (1999) code with two layers. The two plots have the same values for the resistivity but different depths. The resistivity for both cases decreases with depth.

Just like Figure 3.11, Figure 3.12 shows the difference on the behavior of the frequency response for the same resistivity but different values for the first layer thickness. The plots on this figure also show the impedance phase variation along the frequency. In this case the resistivity of the layers decreases with depth. It is possible to see that for a larger top layer, a large range of frequencies get 'stuck' inside the the upper conductivity layer. The impedance phase is higher than 45° except for a little bump where it is smaller than 45° which corresponds to a phase transition between layers (i.e. where is an overlap of the two layers effects), rapidly stabilizing to $\phi = 45°$ in the half-space zone.

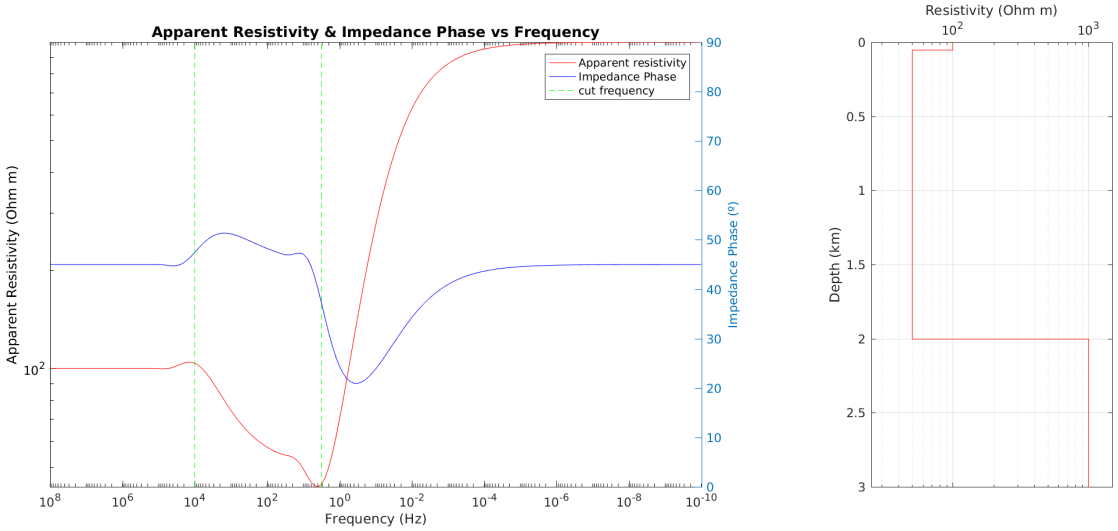

(a) Layer1: $\rho = 100$ Ωm and $z = 50$ m; Layer2: $\rho = 50$ Ωm and $z = 2$ km; Layer3: $\rho = 1000\Omega m$ and $z = \infty$.

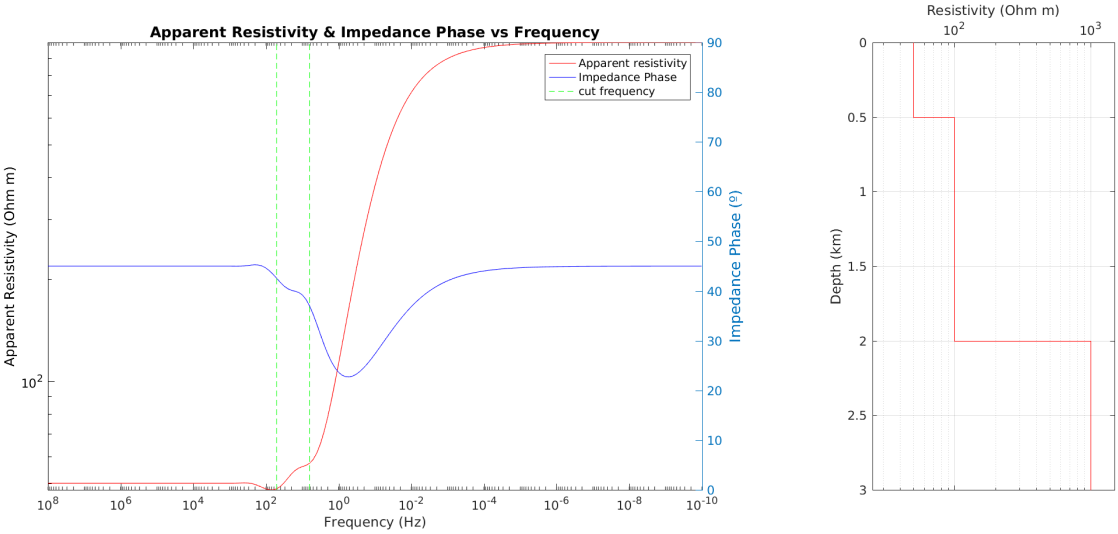

(b) Layer1: $\rho = 50$ Ωm and $z = 500$ m; Layer2: $\rho = 100$ Ωm and $z = 2$ km; Layer3: $\rho = 1000\Omega m$ and $z = \infty$.

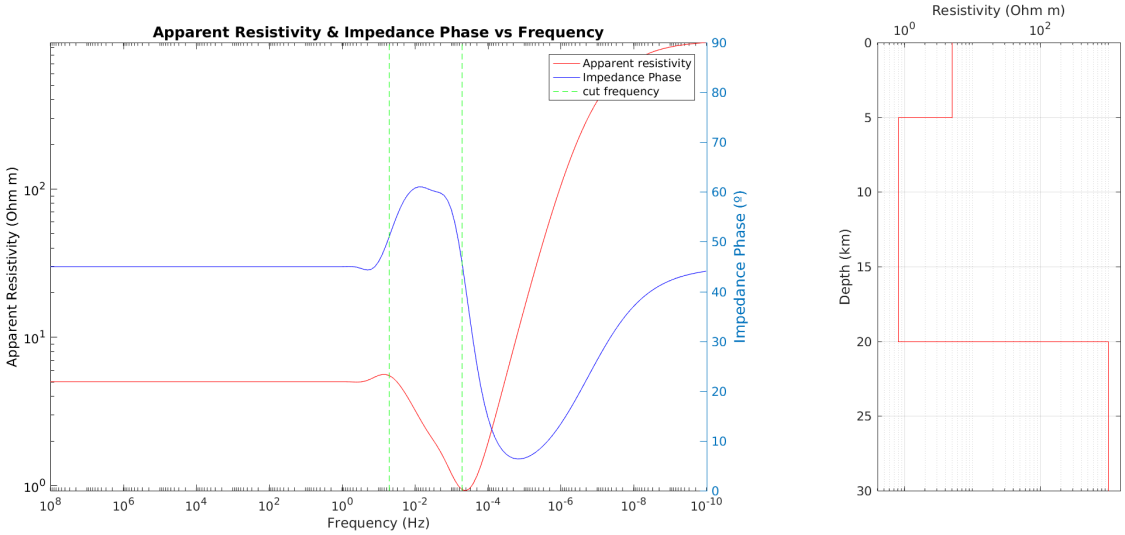

(c) Layer1: $\rho = 5$ Ωm and $z = 5$ km; Layer2: $\rho = 0.8$ Ωm and $z = 20$ km; Layer3: $\rho = 1000\Omega m$ and $z = \infty$.

Figure 3.13: Plot for 1D MT model using Pethick (1999) code with three layers.

Using multiple layers (Figure 3.13) it can be seen an increase complexity in the apparent resistivity behavior. As been seen before, the first layer will always absorb the higher frequencies in agreement with Equations (3.17) and (3.38). It is possible to see the behavior of the apparent resistivity in the transition regions between layers. Analyzing the impedance phase for Figure 3.13(a) and (c) it can be seen that from the first to the second layer, $\phi > 45^{o}$ which is in agreement with the resistivity decreasing with depth. From the second to the third layer is the opposite, i.e. $\phi < 45^{o}$ since the resistivity increases. On the other hand, for Figure 3.13(b), from the first to the second layer, $\phi < 45^{o}$ which is in agreement with the resistivity increasing with depth. From the second to the third layer is the opposite, i.e. $\phi > 45^{o}$ since the resistivity decreases.

Taking into account the typical lithosphere structure with the continental and oceanic crust, it is possible to model this structure using Pethick (1999) code and the results can be seen in Figure 3.14.

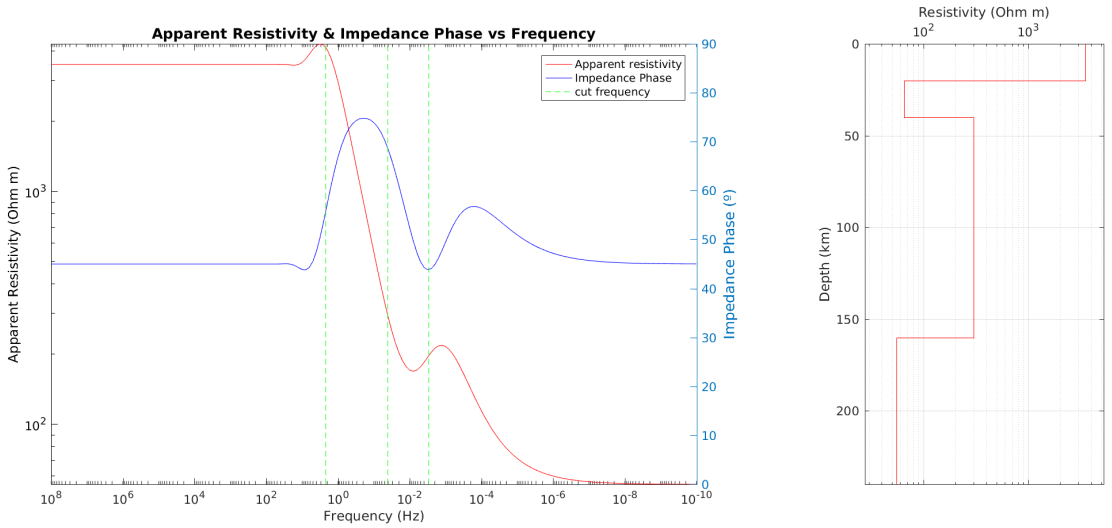

(a) Layer1: $\rho = 3500$ Ωm and $z = 20$ km; Layer2: $\rho = 65$ Ωm and $z = 20$ km; Layer3: $\rho = 300\Omega m$ and $z = 160$ km; Layer4: $\rho = 55\Omega m$ and $z = \infty$.

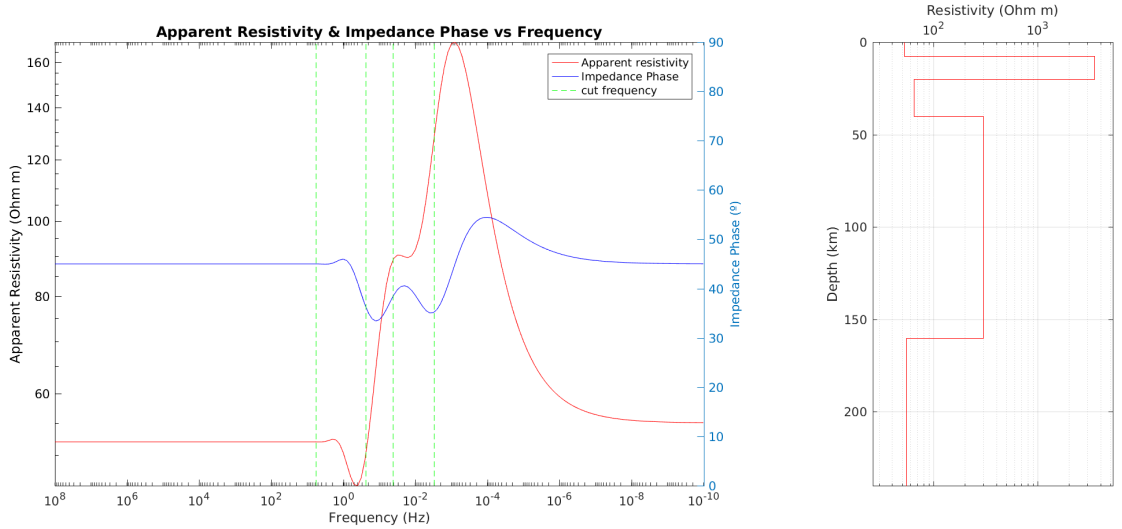

(b) Layer1: $\rho = 52$ Ωm and $z = 7.5$ km; Layer2: $\rho = 3500$ Ωm and $z = 12.5$ km; Layer3: $\rho = 65$ Ωm and $z = 20$ km; Layer4: $\rho = 300$ Ωm and $z = 160$ km; Layer5: $\rho = 55$ Ωm and $z = \infty$.

Figure 3.14: Plot for 1D MT model using Pethick (1999) code with typical values of resistivity for the lithosphere and asthenosphere taken from Unsworth (2015). The first one (a) corresponds to the case of a general upper crust with a high resistivity and the second one (b) is having in the upper crust a sedimentary basin with a relatively low resistivity.

It is possible to see in Figure 3.14, (a) and (b), the differences in the apparent resistivity and impedance phase for the typical lithosphere and asthenosphere structure with and without the sedimentary basin, respectively. The first difference that can be seen is the apparent resistivity values, they are smaller for the case (b) because the sedimentary basin has a lower resistivity due the presence of aqueous fluids. The first jump in ρ_a occurs for a smaller frequency in the first case where the first layer is largest and has a bigger resistivity due to the dry and relatively cold crystalline rocks in it constitution, which is in agreement with Equation (3.38).

Adapting the 2D model of Monteiro Santos et al. (2003) to a 1D model, it is possible to see the differences in the apparent resistivity and impedance phase for the typical lithosphere and asthenosphere structure with the continental and oceanic crust (Figure 3.15).

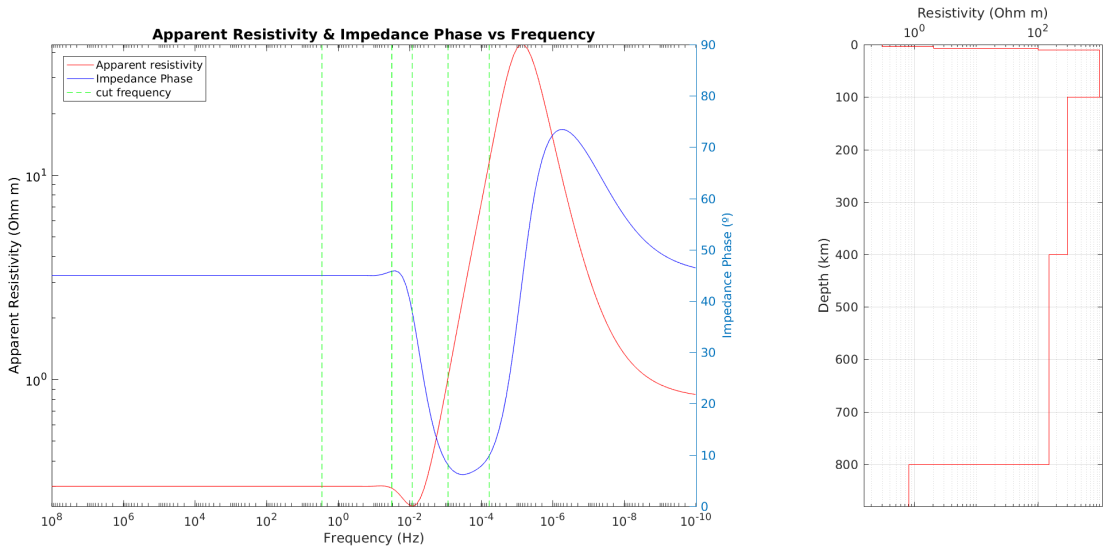

(a) Layer1: $\rho = 0.3$ Ωm and $z = 3$ km; Layer2: $\rho = 2$ Ωm and $z = 4$ km; Layer3: $\rho = 100$ Ωm and $z = 3$ km; Layer4: $\rho = 1000$ Ωm and $z = 90$ km; Layer5: $\rho = 300$ Ωm and $z = 300$ km; Layer6: $\rho = 150$ Ωm and $z = 800$ km; Layer6: $\rho = 0.8$ Ωm and $z = \infty$.

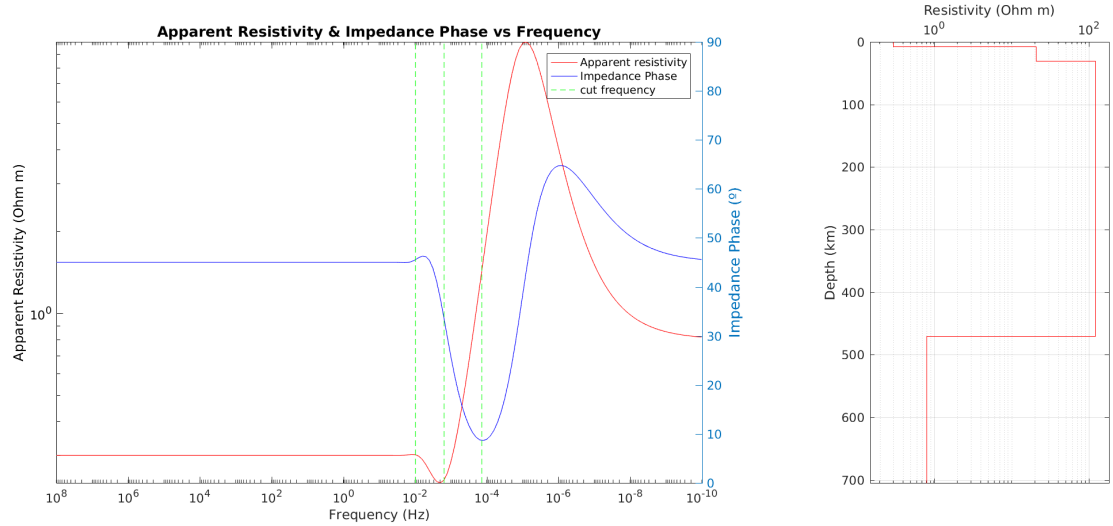

(b) Layer1: $\rho = 0.3$ Ωm and $z = 7$ km; Layer2: $\rho = 20.5$ Ωm and $z = 23$ km; Layer3: $\rho = 120$ Ωm and $z = 470$ km; Layer4: $\rho = 0.8$ Ωm and $z = \infty$.

Figure 3.15: Plot for 1D MT model with data adapted from Monteiro Santos et al. (2003) using Pethick (1999) code.

Figure 3.15 shows the effect in the MT response of a highly conducting upper layer (the ocean).

The results presented above show the following general behavior: the effect of layers at increasing depth is seen at smaller frequency values. When going from a less conductive layer (top) to a more conductive layer (bottom), the apparent resistivity decreases and

the impedance phase shows a bump over 45°. The inverse occurs when going from a more conductive layer (top) to a less conductive layer (bottom). For a 1D model with multiple layers, the apparent resistivity curve shows an asymptotic behavior towards the resistivity values of the uppermost and lowermost layers, at either end of the period range.

Chapter 4

Geomagnetic Storms and Induced $\vec{E}$ field

4.1 Precursors and Proxies of the storms

The irregular current systems described in Subsection 2.3.2 cause variations in the Geomagnetic Field measured on Earth, as stated before. These variations can be empirically described by the Geomagnetic Activity Indices (GAI) (the proxies) and, for values of GAI above certain values, be identified as geomagnetic storms (Martini et al., 2016). As geomagnetic storms occur because of the interaction of the solar wind and the interplanetary magnetic field with the magnetic field of the Earth, solar wind and the IMF parameters can be used as precursors of geomagnetic storms.

In the following subsections are presented some precursors (subsections 4.1.1 to 4.1.5) and some proxies (subsections 4.1.7 to 4.1.10).

4.1.1 GSM Coordinate System

In order to characterize the orientation of the Interplanetary Magnetic Field (IMF) (subsection 4.1.2), the Geocentric Solar Magnetic (GSM) coordinate system must be introduced. This coordinate system has its origin at the center of the Earth and its x-axis is the line connecting that point to the center of the Sun (see Figure 4.1). The y-axis is positive towards dusk and perpendicular to both the Earth's magnetic dipole axis and the Earth-Sun line. The z axis, which consequently is in the plane containing both the Earth-Sun line and the dipole axis, completes a right-handed system. (Caraballo, 2016; Laundal and Richmond, 2017)

The GSM coordinate system allows to reduce the three dimensional motion of the Earth's magnetic dipole to a two dimensional motion in the x-z plane. Because of that, it is used

in regions strongly controlled by the solar wind and the interplanetary magnetic field since the orientation of the magnetic dipole axis alters the otherwise cylindrical symmetry of the solar wind flow. (Laundal and Richmond, 2017)

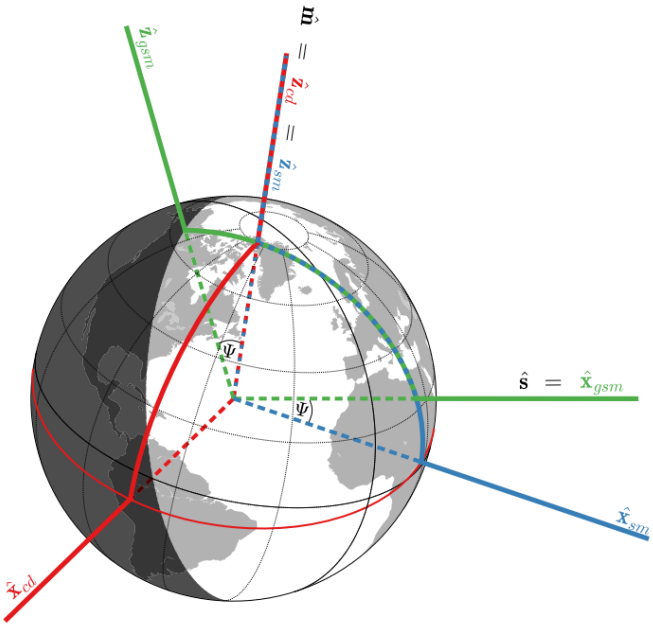

Figure 4.1: Illustration of the x and z axis of the GSM coordinate system (green). The xz plane is spanned by the vectors $\hat{m}$ (along the Earth magnetic dipole axis) and $\hat{s}$ (pointing to the Sun). The GSM x-axis is along $\hat{s}$, and the z-axis intersects the sunlight terminator (shaded side of the Earth). The y-axis is perpendicular to the plane containing the GSM x-axis and the magnetic dipole, and points towards dusk. Laundal and Richmond (2017)

4.1.2 IMF parameters

The IMF (also known as Heliospheric Magnetic Field, HMF) is defined as the component of the solar magnetic field that is dragged out from the solar corona frozen to the solar wind flow into the interplanetary space. It originates in regions on the Sun where the magnetic field lines are "open", i.e. where field lines emerging from one region extend virtually indefinitely into space. Like the solar wind, the IMF travels outward in a spiral pattern because of the sun's rotation (Figure 4.2). (Smith et al., 1978)

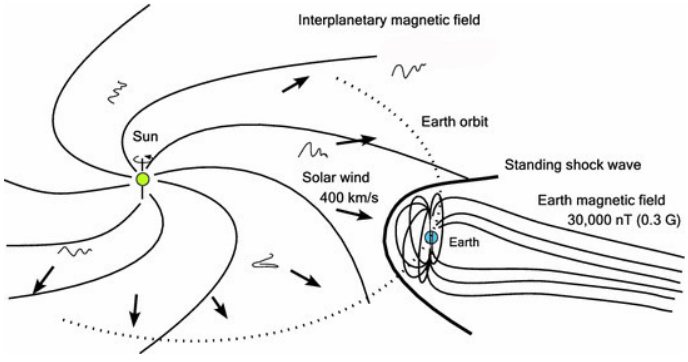

Figure 4.2: Schematic representation of the IMF. (Narita, 2012)

It takes, on average, about 4.5 days for a radially flowing solar wind to transport the solar magnetic field to a position near the earth, considering the solar wind velocity approximately 380 km/s (Schatten et al., 1969). The transfer of energy, mass and momentum from the solar wind flow to the magnetosphere occur when the geomagnetic field lines and the IMF are oriented opposite to each other (Smith et al., 1978) and the field strength is $B_{IMF} \simeq 15-30$ nT at 1AU – values from actual observations from the IMP-8 and ISEE-3 spacecraft. (Lepping et al., 1990)

4.1.3 Solar Wind parameters

As explained in Section 2.2, the solar wind influences the Earth's magnetosphere environment, and sometimes it causes geomagnetic storms. So, there is a relation between solar wind parameters and storms. The solar wind parameters that will be used to study the storms of 2015 (Section 4.2) are: velocity, V [km/s]; proton density, N_p [cm^{-3}] and proton flux temperature, T [K]. These parameters are obtained by multiple spacecrafts whose mission is to measure the properties of the solar wind before it reaches the Earth. The ones that provide the data for OMNIWeb Data (omniweb.gsfc.nasa.gov/) are **ACE**[1], **Wind Spacecraft**[2] and **ISEE-3** [3] with orbit around the L1 Lagrange Point and also: **IMP-8**[4] also known as Explorer 50, with apogee of $\sim 45r_E$, perigee of $\sim 25r_E$ and orbital inclination between 0° and 55°; **IMP-7**[5] with a roughly circular orbit with apogee of $\sim$ 200 000 km; **IMP-6**[6] elliptical orbit with apogee $>$ 200 000 km and **Geotail**[7] apogee of 200 000 km, perigee of 57 000 km and orbital inclination of 29°.

4.1.4 Dipole Tilt angle

The dipole tilt angle is defined as the angle between the geomagnetic dipole axis and the GSM z-axis (Ψ in Figure 4.1) (Cnossen et al., 2012). It has two types of variations: diurnal and annual. The diurnal variation is due to precession of magnetic dipole axis with respect to the Earth's rotation axis. This value is dependent on time, being $\pm 9.7°$ at present. The annual variation ($\pm 23.5°$) comes from the precession of the Earth's axis with respect to the normal to the solar ecliptic (Balan et al., 2017).

[1] www.srl.caltech.edu/ACE/
[2] wind.nasa.gov/
[3] nssdc.gsfc.nasa.gov/nmc/spacecraft/display.action?id=1978-079A
[4] science.nasa.gov/missions/imp-8
[5] heasarc.gsfc.nasa.gov/docs/heasarc/missions/imp7.html
[6] heasarc.gsfc.nasa.gov/docs/heasarc/missions/imp6.html
[7] solarsystem.nasa.gov/missions/geotail/in-depth/

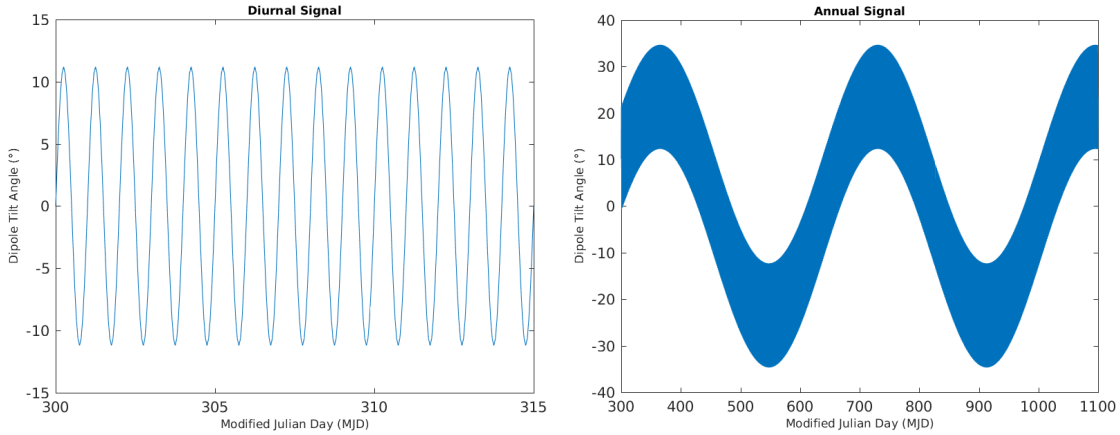

(a) Diurnal variation (±11.2° at time 2010) of the dipole tilt angle. (Balan et al., 2017)

(b) Annual variation (±23.5°) of the dipole tilt angle. (Balan et al., 2017)

Figure 4.3: Diurnal and annual variations of the dipole tilt angle. Both plots adapted from Kunagu and Chandrasekhar (2013). The total variation is between (±34.7° at time 2010) (Balan et al., 2017).

According to Cnossen et al. (2012), the annual Ψ values can be grouped into three types:

- $\Psi > 0$ – occurs at summer solstice, when the northern hemisphere (NH) is tilted toward the Sun;
- $\Psi = 0$ – at the equinoxes (when the geomagnetic activity will be higher (Nowada et al., 2009));
- $\Psi < 0$ – occurs at winter solstice, when the northern hemisphere (NH) is tilted away from the Sun.

This angle can cause variations on:

- the coupling efficiency between the magnetosphere and the solar wind (on which will depend the transfer of energy, mass, and others, as seen in the previous subsection); (Cnossen et al., 2012)
- the ionospheric convection and conductance over the polar caps[8] leading to changes in how much Joule heating occurs. This means variations in the thermospheric temperature structure caused by the change of the vertical component of ionospheric plasma diffusion along the magnetic field. (Cnossen et al., 2012; Cnossen and Richmond, 2012)

4.1.5 Newell's Coupling function

Newell's coupling function (***NLL***) is an universal coupling function developed by Newell et al. (2007) that is related with the rate of IMF magnetic flux entering the magnetosphere taking into account three factors: (Newell et al., 2007)

[8] polar caps: regions around the magnetic poles that are the places on Earth most sensitive to distant magnetic effects.

- the rate at which field lines are convected toward the magnetopause (determined by the solar wind velocity V);
- the probability of solar wind and geomagnetic field lines merging at the magnetosphere, calculated by a sine function of the clock angle θ_c (angle defined by IMF_y and IMF_z components of the IMF in the GSM coordinate system) that is $\theta_c = \arctan(\mathrm{IMF}_y/\mathrm{IMF}_z)$;
- the strength of the transverse IMF i.e. $B_T = \sqrt{\mathrm{IMF}_y^2 + \mathrm{IMF}_z^2}$.

In the end, ***NLL*** yields,

$$\mathrm{NLL} = 10^{-4} V^{4/3} B_T^{2/3} \sin^{8/3}(\frac{\theta_c}{2}) \tag{4.1}$$

where V is the solar wind velocity in km/s, B_T is the transverse IMF in nT and θ_c is the clock angle. (Newell et al., 2007)

4.1.6 The local geographic coordinate system

The proxies for geomagnetic storms are based on a local coordinate system contrary to the precursors. The local geographic coordinate system (Figure 4.4) has the x-axis pointing to the north and the y-axis to the east. The z-axis is consequently pointing to the center of the Earth.

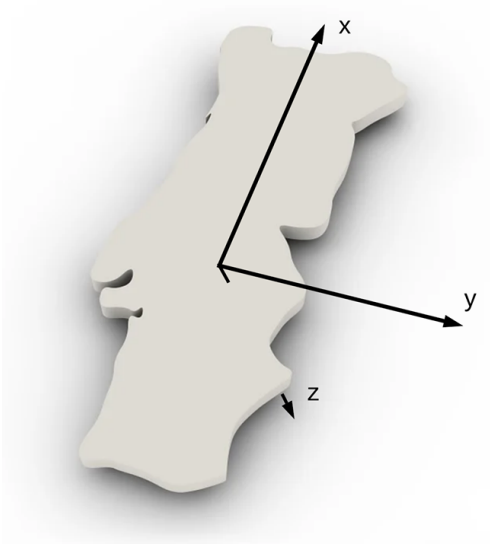

Figure 4.4: Local geographic coordinate system with the xy plane tangent to the surface of the Earth and the z-axis pointing to the center.

4.1.7 K-Index

The ***K-index*** quantifies the level of disturbance in the horizontal component of Earth's magnetic field caused by the influence of the solar wind, during each 3-hour interval. This index is obtained at a given location, using magnetic measurements on Earth. It scales

from 0 (completely quiet conditions) to 9 (severe storm) and gives eight three-hour interval values per day. (Blake, 2017)

Being S_q the solar-regular or solar-quiet curve, i.e. the daily variation in the magnetic field due to thermal convection of ionospheric plasma, the K-index does not take it into account by removing its contribution from the data. The S_q curve must be determined before calculating the K-index. It is a smooth curve for quiet days, but for disturbed days it is obscured by magnetospheric and ionospheric activity (Blake, 2017). After removing S_q, for the remainder of the horizontal magnetic signal, 3-hours K values are computed from the logarithm of the difference between the maximum and the minimum values during each 3-hours interval.

4.1.8 Kp-Index

The ***Kp-index*** is the planetary K-index and was introduced by J. Bartels in 1949. It is used to show the disturbance of the Earth's magnetic field on a global scale (at low and mid latitude) through the average at the NOAA Space Weather Prediction Center of local K-indices taken from the observatories marked in Figure 4.5 (Blake, 2017). This proxy has a scale of 28 values (Kp = 0o, 0+, ..., 9−, 9o, 9+) – Table 4.1.

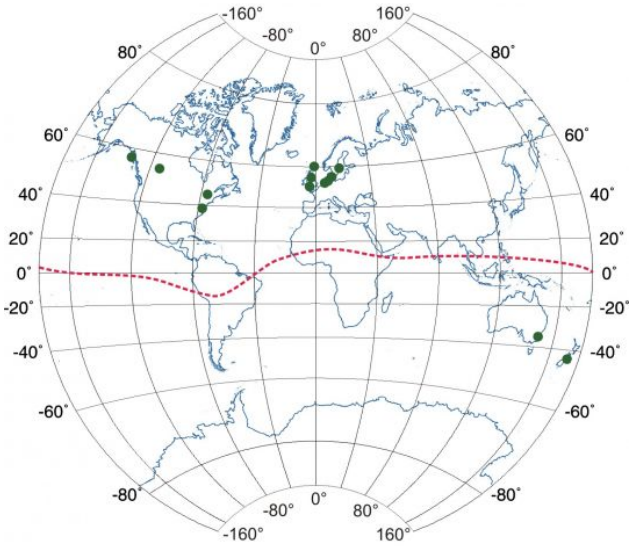

Figure 4.5: Observatories in the United States, Canada, United Kingdom, Germany and Australia that are part of NOAA/SWPC and contribute for the Kp values. (Azzarone, 2003b)

The G-scale is a qualitative scale that indicates the severity of both observed and predicted geomagnetic activity and every G-level has a certain K-value associated as can be seen in Table 4.1. (SpaceWeatherlive, 2003).

G-Scale	Auroral Activity	Kp
G0	Quiet	0*o* to 2+
	Unsettled	3− to 3+
	Active	4− to 4+
G1	Minor Storm	5− to 5+
G2	Moderate Storm	6− to 6+
G3	Strong Storm	7− to 7+
G4	Severe Storm	8− to 8+
G5	Extreme Storm	9− to 9+

Table 4.1: Table adapted from SpaceWeatherlive (2003) using values of the Kp-index and respective G-scale from NOAA/SWPC.

According to the NOAA/SWPC table for geomagnetic storm classification (available on `https://www.swpc.noaa.gov/noaa-scales-explanation`), the effects caused by a geomagnetic storm in the power systems are:

- *G1* level: "Weak power grid fluctuations can occur."
- *G2* level: "High-latitude power systems may experience voltage alarms and long-duration storms may cause transformer damage."
- *G3* level: "Voltage corrections may be required, false alarms triggered on some protection devices."
- *G4* level: "Possible widespread voltage control problems and some protective systems will mistakenly trip out key assets from the grid."
- *G5* level: "Widespread voltage control problems and protective system problems can occur, some grid systems may experience complete collapse or blackouts. Transformers may experience damage."

4.1.9 Dst-Index

The ***K*** and ***Kp*** indexes have a 3-hour resolution. With a higher resolution, there is the ***Dst-index***, Disturbance storm time index, that is given in nT and indicates the hourly perturbation in the horizontal component of the magnetic field at four equatorial magnetic observatories (Blake, 2017; Rosales, 2017) – see Figure 4.6. As for ***K*** and ***Kp*** indexes, the S_q curve is also subtracted. Hourly values are available since 1957 (Hathaway, 2015). The Dst variations during storms are mainly due to the effect of globally symmetrical ring current, but they are also influenced by the partial ring current, the near-tail current, the dayside magnetopause currents and the field-aligned currents (FACs). (Hamilton et al., 1988; Turner et al., 2000)

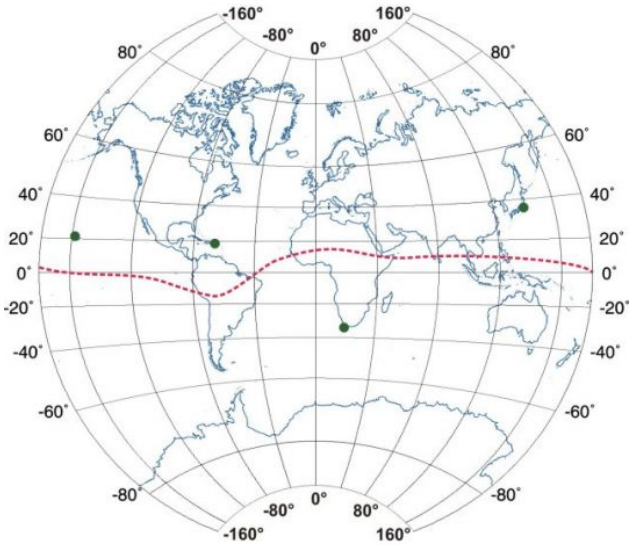

Figure 4.6: Near equatorial magnetic observatories that contribute to the ***Dst-index***. From left to right: Honolulu (Hawaii), San Juan (Puerto Rico), Hermanus (South Africa) and Kakioka (Japan). (Azzarone, 2003a)

This index is used to classify each geomagnetic storm (Table 4.2) and to identify its different phases:

- **Sudden Storm Commencement** (SSC): a rapid increase in field strength (and in Dst) as the field is compressed by the incoming plasma due to ram pressure, i.e. due to the pressure exerted on Earth's magnetic field by incoming plasma; (Bailey, 2018; Gonzalez et al., 1999)
- **Initial phase**: continuous increase of the horizontal component of the geomagnetic field worldwide, with plasma being sent from the neutral sheet of the magnetosphere toward the night side of Earth. (Gonzalez et al., 1999)
- **Main phase**: when the horizontal field component (and Dst) decreases to strongly negative values and this is when sub-storms and the largest geomagnetic variations tend to occur. The extent of the field strength decrease and the magnitude of the variations depend primarily on the solar wind-magnetosphere coupling as given for instance by NLL. (Bailey, 2018; Gonzalez et al., 1999)
- **Recovery phase**: the horizontal field component and Dst gradually return to the normal value. (Bailey, 2018; Gonzalez et al., 1999)

Storm Classification	**Dst (nT)**
Super	< -200
Intense	$[-200, -100]$
Moderate	$[-100, -50]$
Weak	$[-50, -30]$

Table 4.2: Classification of the Geomagnetic Storms. (Azzarone, 2003a)

4.1.10 SYM-H geomagnetic index

The ***SYM-H index*** is the Symmetric Disturbance Horizontal index. As it is computed from the average of values longitudinally distributed, it mainly represents the contribution from the longitudinal symmetric component of the ring current (Bhaskar and Vichare, 2019). It is computed as *Dst* but with a higher temporal resolution since it is obtained from 1 min data of the magnetic field while *Dst* consists in hourly values.

4.2 Geomagnetic storms at COI – original analysis

In order to identify storms during 2015, the local Geomagnetic K indices provided by the Geophysical and Astronomical Observatory of the University of Coimbra (OGAUC) were used (Figure 4.7). The five most important storms found are plotted in Figures 4.8 and 4.9, for 17th March, 22nd June, 7th October, 14th December and 20th December.

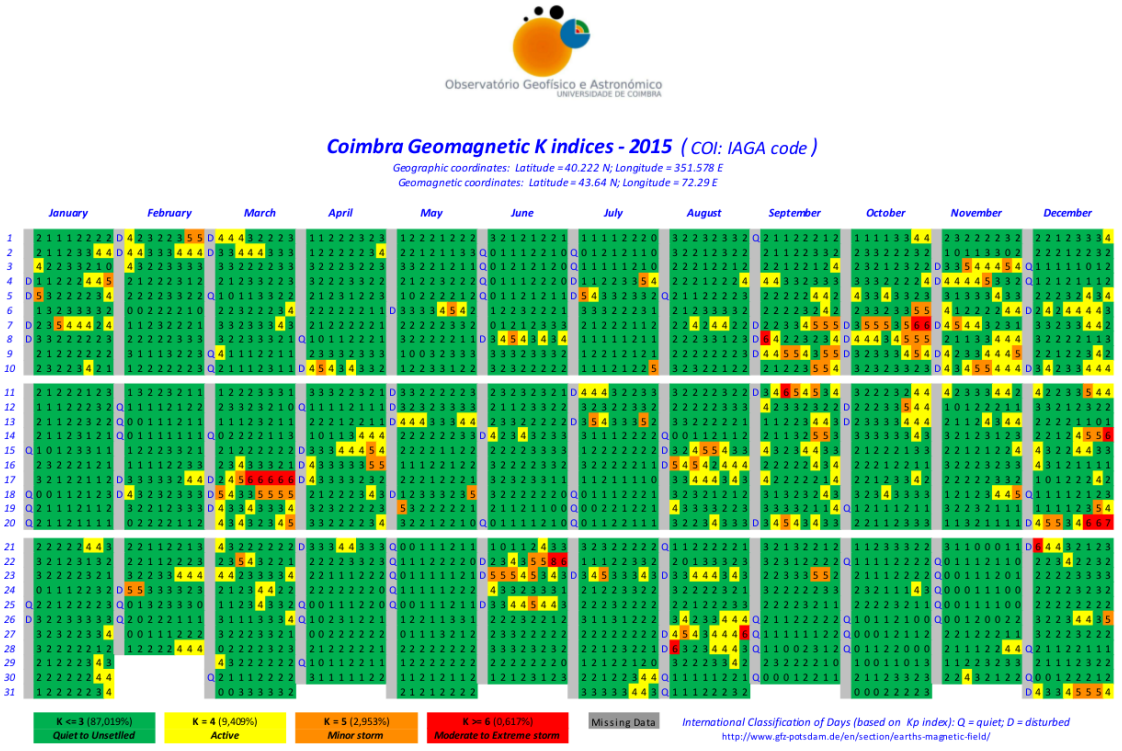

Figure 4.7: Geomagnetic *K-index* measured at COI during 2015. The data squares marked as orange are for $K = 5$, while red squares represent $K \geqq 6$.

Figures 4.8 and 4.9 represent the local K index during the selected storms and have the same color code as Figure 4.7.

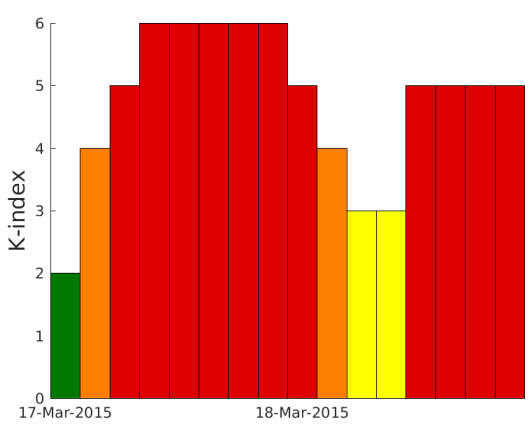

(a) Storm of March.

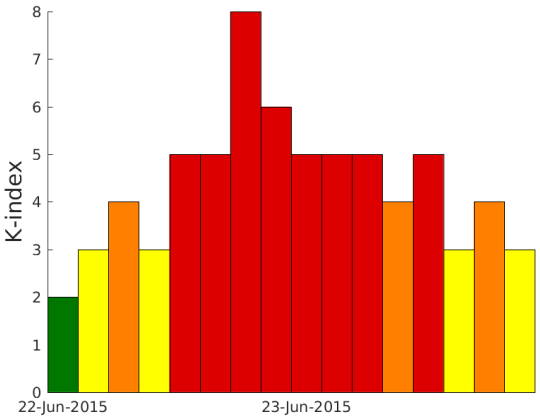

(b) Storm of June.

Figure 4.8: Geomagnetic Storms identified using the K index table of Figure 4.7 for the first semester of 2015.

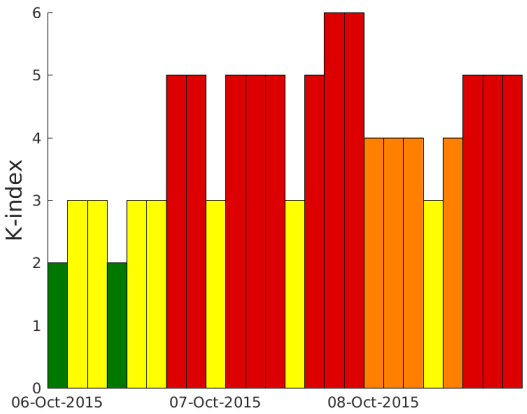

(a) Storm of October.

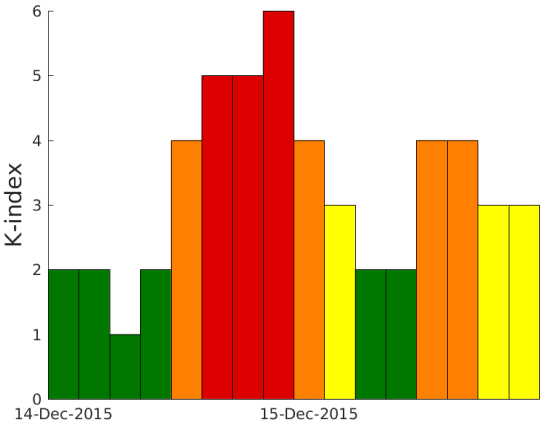

(b) First storm of December.

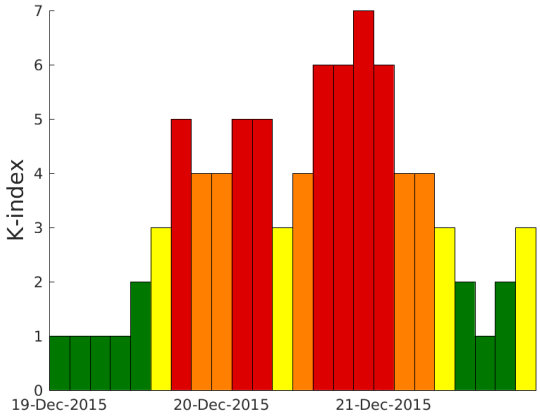

(c) Second storm of December.

Figure 4.9: Geomagnetic Storms identified using the K index table of Figure 4.7 for the second semester of 2015.

With the storms of interest already identified, it is time to look at the proxies and precursors

explained in Section 4.1 for each one of them. The proxies and precursors ploted below were extracted from NASA/GSFC's OMNI data base through OMNIWeb with data of 5-minutes intervals and with the storms phases (subsection 4.1.9) highlighted and identified with the help of the SYM-H curve. The local storm data (with 1-minute intervals) came from the Coimbra observatory (COI)[9].

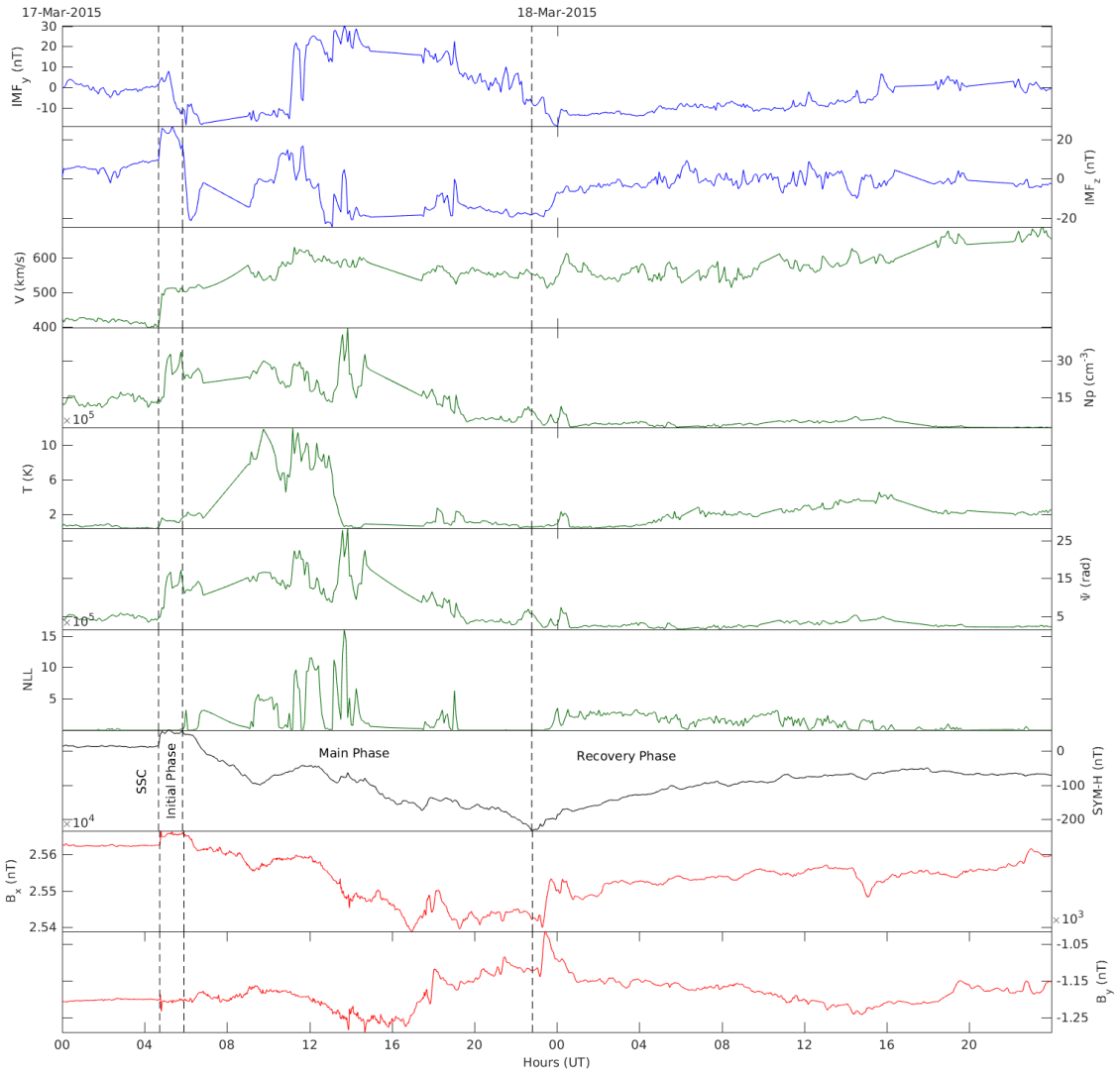

Figure 4.10: Precursors and Proxies for the Storm of March 2015 with SYM-H$_{min}$ = −233 nT which corresponds to a super storm (Table 4.2).

The storm in Figure 4.10 was the most intense one, globally, in the rising-maximum phase of cycle 24 and it is called as the *St. Patrick's Day* storm. (Watari, 2017)

[9]The data from Coimbra was provided by Eng. Paulo Ribeiro from CITEUC and OGAUC.

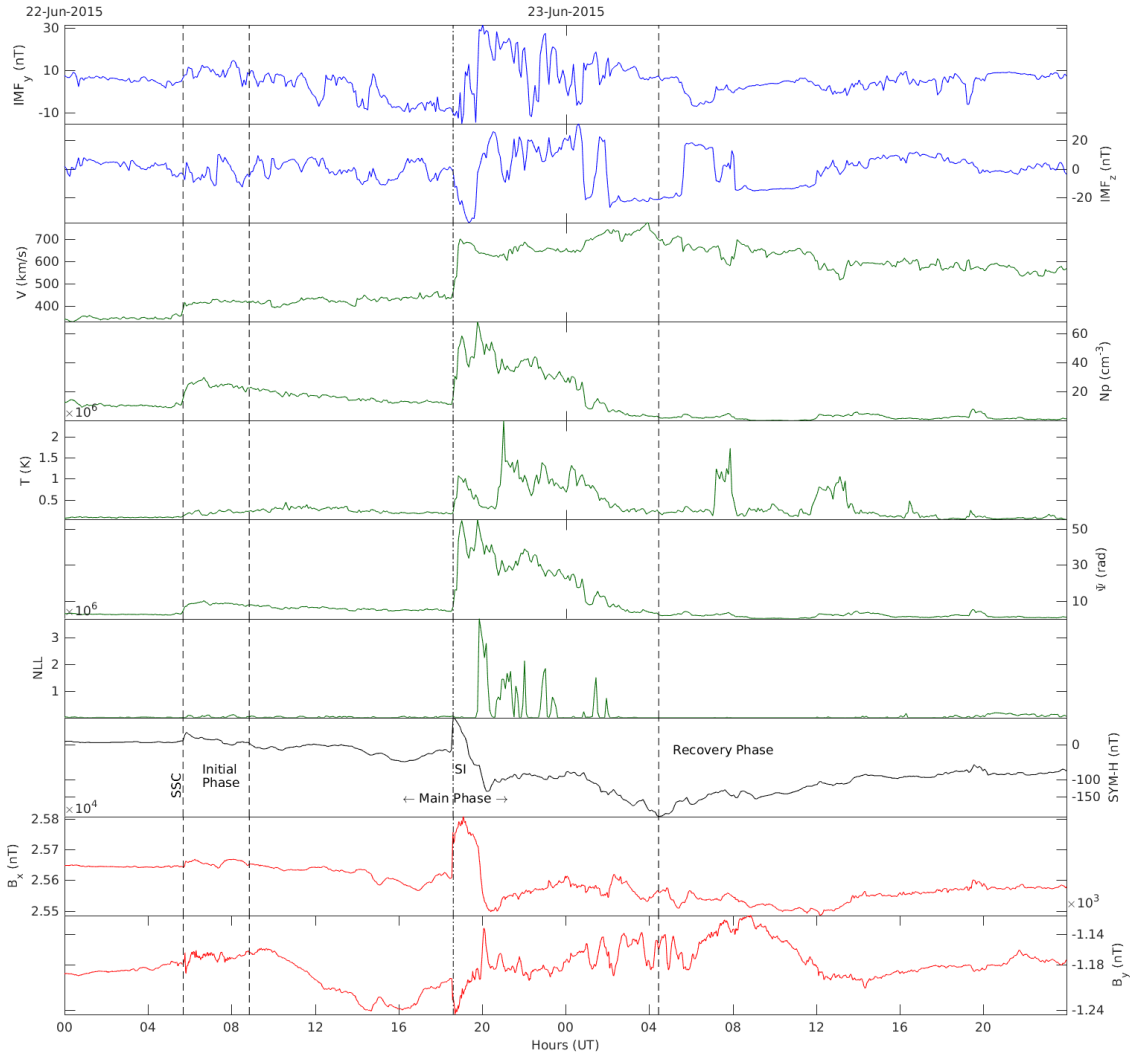

Figure 4.11: Precursors and Proxies for the Storm of June 2015 with SYM-H$_{min}$ = −207 nT which correspond to a super storm (Table 4.2).

The storm in Figure 4.11 is a more complex situation due to successive inputs of energy which results in an overlap of phases. There are two ways to "work" with this types of storms: either by separating the sub-storms or by encompassing all activity in a single one. In this case was chosen the second way considering that it has a sudden impulse (SI) in the middle of the main phase.

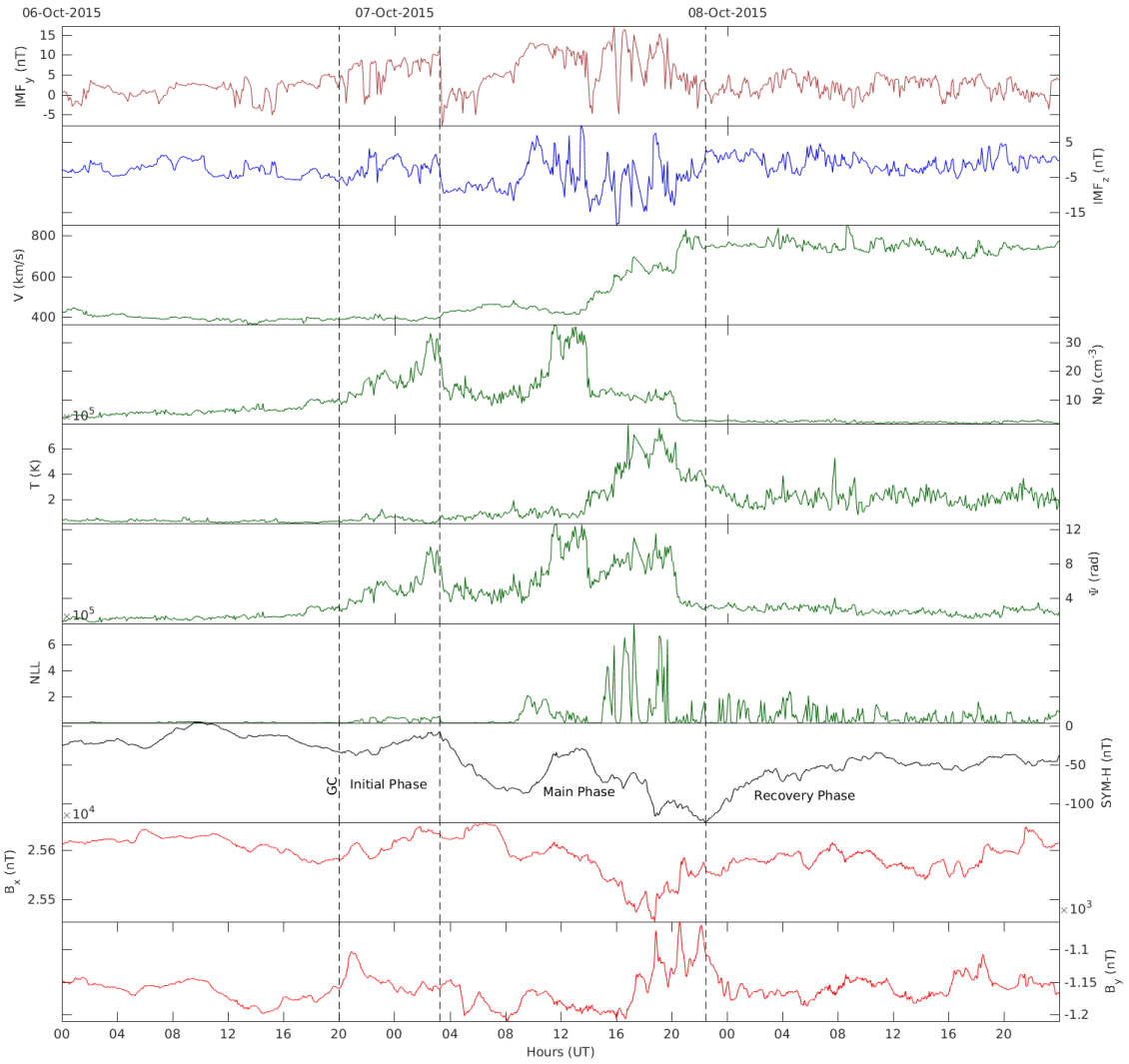

Figure 4.12: Precursors and Proxies for the Storm of October 2015 with a gradual commencement and SYM-H$_{min}$ = −124 nT which corresponds to an intense storm (Table 4.2).

The storm in Figure 4.12 does not have a sudden storm commencement. In these cases it is difficult to define precisely the beginning, so it is defined a gradual commencement (GD) with the help of the magnetic field values.

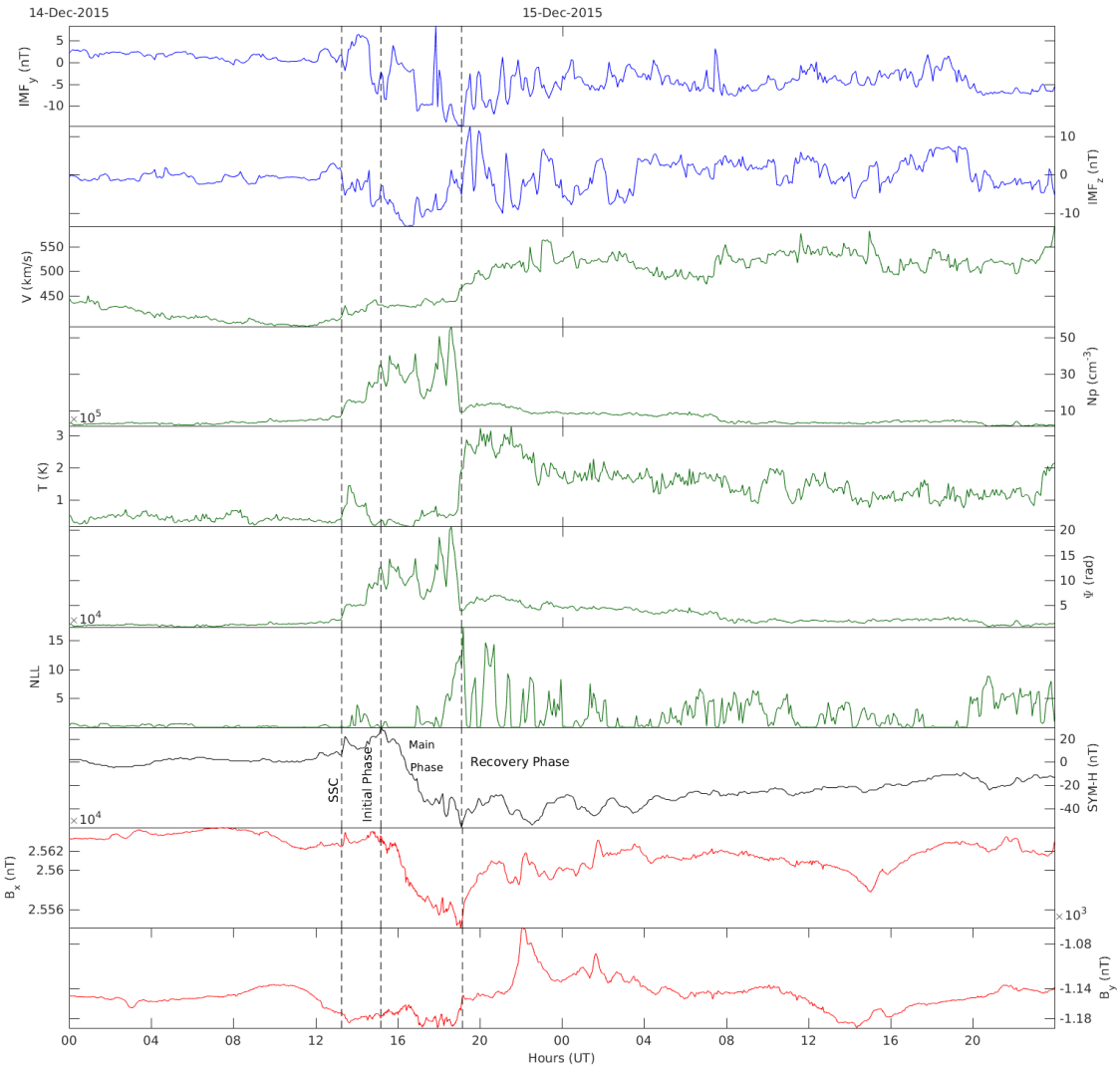

Figure 4.13: Precursors and Proxies for the first storm of December 2015 with SYM-H$_{min} = -54$ nT which corresponds to a weak storm (Table 4.2).

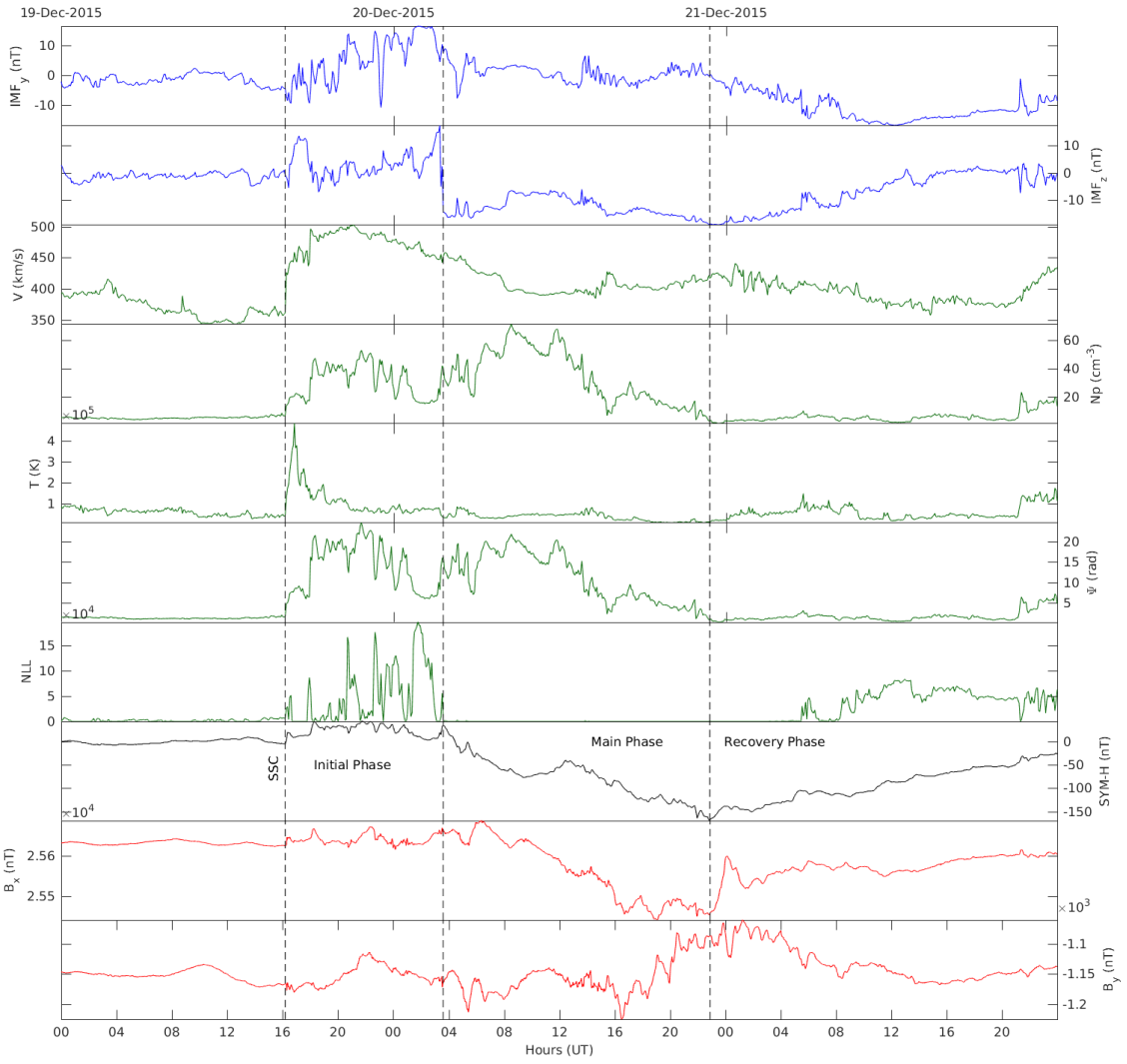

Figure 4.14: Precursors and Proxies for the second storm of December 2015 with SYM-H$_{min}$ = −169 nT which corresponds to an intense storm (Table 4.2).

As explained on Section 2.2, the storms have different origins. For these storms, their sources are listed in Table 4.3.

Storm	Type	Solar Sources
March	SC	Partial halo CME (sheath, MC) coronal hole?
June	SC	Full halo CME (sheath, MC) multiple
October	GC	(MC) coronal hole
December	SC	Full halo CME (MC)

Table 4.3: Solar sources that caused the analyzed storms. Table adapted from Watari (2017).

4.3 Induced Electric Field

To understand how geomagnetic storms can cause GICs it is necessary to apply the theory for electromagnetic induction, starting with Maxwell's equations (Equations (3.1) to (3.4)). The diffusion of an oscillating magnetic field with direction along the x-axis (for instance) into an half-space along the z-axis is a solution of Equation (3.13). From Equation (3.14) with $\mathbf{B}_2 = 0$ it came

$$B_x(z,t) = B_{0,x}e^{iwt - z/\delta} \tag{4.2}$$

where it is assumed that $\frac{\partial}{\partial z} \gg \frac{\partial}{\partial x}, \frac{\partial}{\partial y}$ and the definition of skin depth (δ) from Equations (3.16) and (3.17) is used.

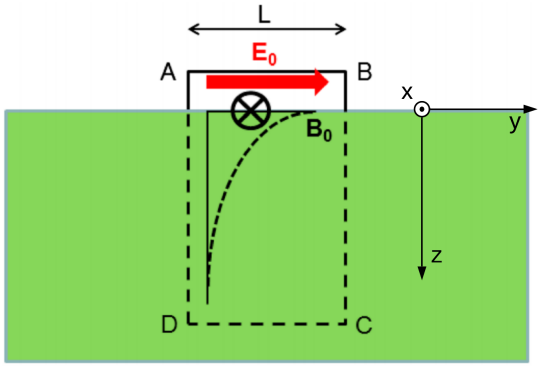

Figure 4.15: Powerline AB with lenght L with $\mathbf{E}_0$ and $\mathbf{B}_0$ the electric and magnetic fields at the Earth surface, respectively. (Boteler and Pirjola, 2017)

$B_{0,x}e^{iwt}$ is the geomagnetic storm signal felt on the Earth surface, for frequency ω. The magnetic flux Φ_B through the loop $ABCD$ (Figure 4.15) where segment DC is at $z \to \infty$ is, by Ampère-Law,

$$\Phi_B = \int_0^\infty B_x dz L = \delta B_{0,x} L e^{iwt} \tag{4.3}$$

By Faraday's Law, the f.e.m in the loop is

$$\begin{aligned} \oint_{ABCD} E_y dl &= -\frac{d\Phi_B}{dt} \Leftrightarrow \\ \Leftrightarrow \mathrm{E}_{0,y} L e^{iwt} &= -i\omega\delta B_{0,x} L e^{iwt} \end{aligned} \tag{4.4}$$

Since $\mathbf{E}$ field is horizontal, it means that there is no electric field E_y along BC ou DA (Boteler and Pirjola, 2017) it finally yields

$$\mathrm{E}_{0,y} = -i\omega\delta B_{0,x} \tag{4.5}$$

The above results refer to a single frequency ω. The geomagnetic storm signal $B(t)$ contains an interval of frequencies. In the special case of an half-space model with uniform conductivity σ for $z > 0$, applying the inverse Fourier transform to Equation (3.25) yields (Blake, 2017):

$$E_{x,y}(t) = \pm\frac{1}{\sqrt{\pi\mu_0\sigma}} \int_0^\infty \frac{1}{\sqrt{\tau}} dB_{x,y}(t-\tau)d\tau \tag{4.6}$$

In the general case there won't be such a simple analytical expression, but in any case the method to calculate E fields time series for GIC studies is to inverse Fourier transform Equation (3.25).

4.4 The induced E-field for the portuguese south region – Original calculation

ModEM stands for Modular System for EM inversion and is a code to compute 3D inversion models for MT studies (available on `http://www.modem-geophysics.com/`), which means that it allows to obtain the impedance tensor **Z** (see Section 3.3) in a certain region from the 3D conductivity model (Figure 4.16). In this case, the region of interest is the portuguese south region (Figure 4.17).

Having the impedance matrix on a grid (Figure 4.17), and the magnetic field from COI storms, it is possible to get the induced electric field for the region.

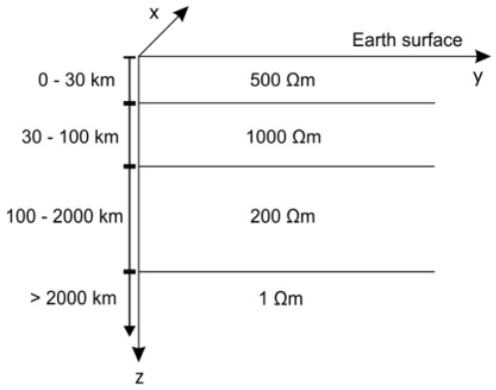

Figure 4.16: Simplified model of the electric conductivity. (Pinheiro et al., 2020)

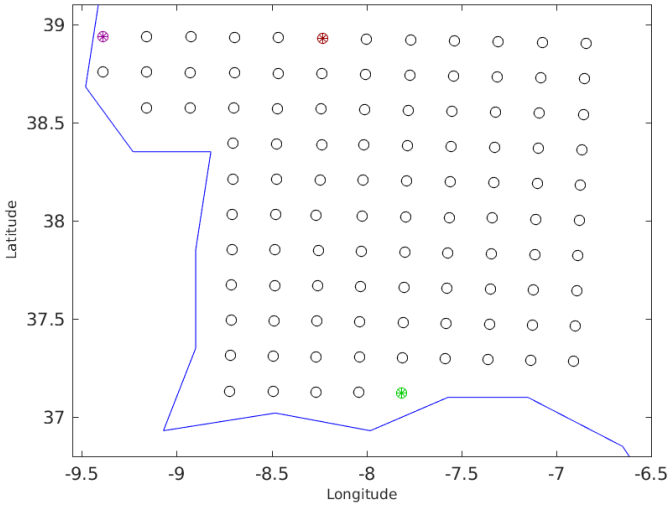

Figure 4.17: Geographic location of the grid used in **ModEM**. The three highlighted points (purple, red and green) are the locations where the induced **E** field is calculated – Figures 4.20 to 4.24.

The induced **E** field calculation was done with a Python script explained in Figure 4.18, fed with the ModEM output. (Alves Ribeiro et al., 2020)

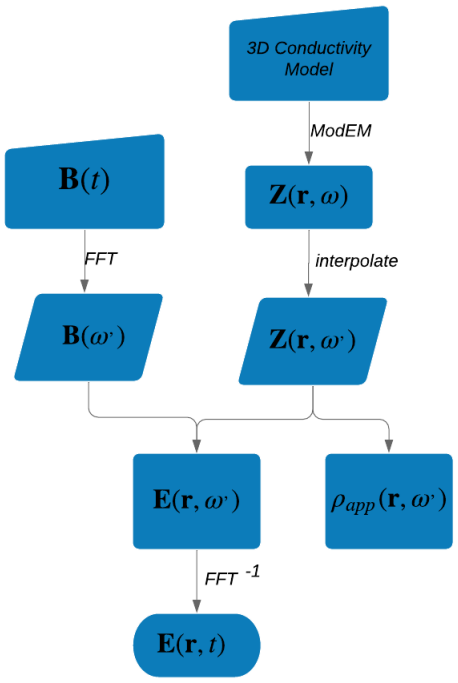

Figure 4.18: Flowchart of the algorithm to calculate de induced E-field.

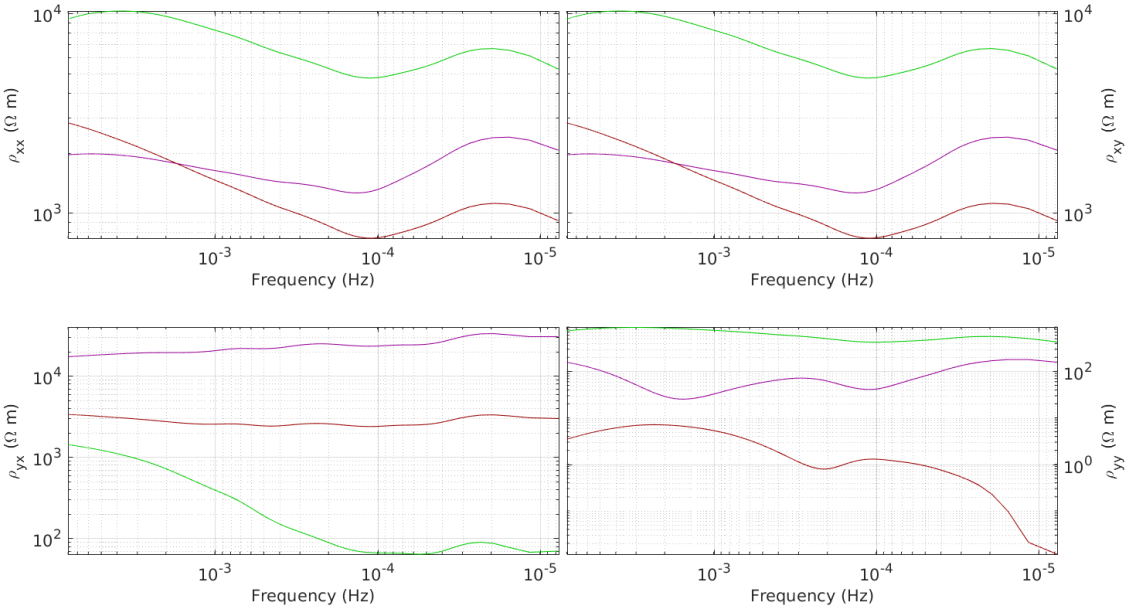

Figure 4.19: ModEM apparent resistivity responses as shown in the flowchart of the Figure 4.18 for the three points highlighted in Figure 4.17.

Taking the geomagnetic field of each storm (B_x and B_y in Figures 4.10 to 4.14) the induced **E** field was computed as explained in Figure 4.18, using a 3D conductivity model for the south region of Portugal (Alves Ribeiro et al., 2020; Pinheiro et al., 2020). For this study,

the induced **E** field was calculated for the entire grid and only the results for the three points are shown (Figures 4.20 to 4.24). These points were chosen due their location: near both coasts (one at the west coast and the other at the south) and one far from the ocean.

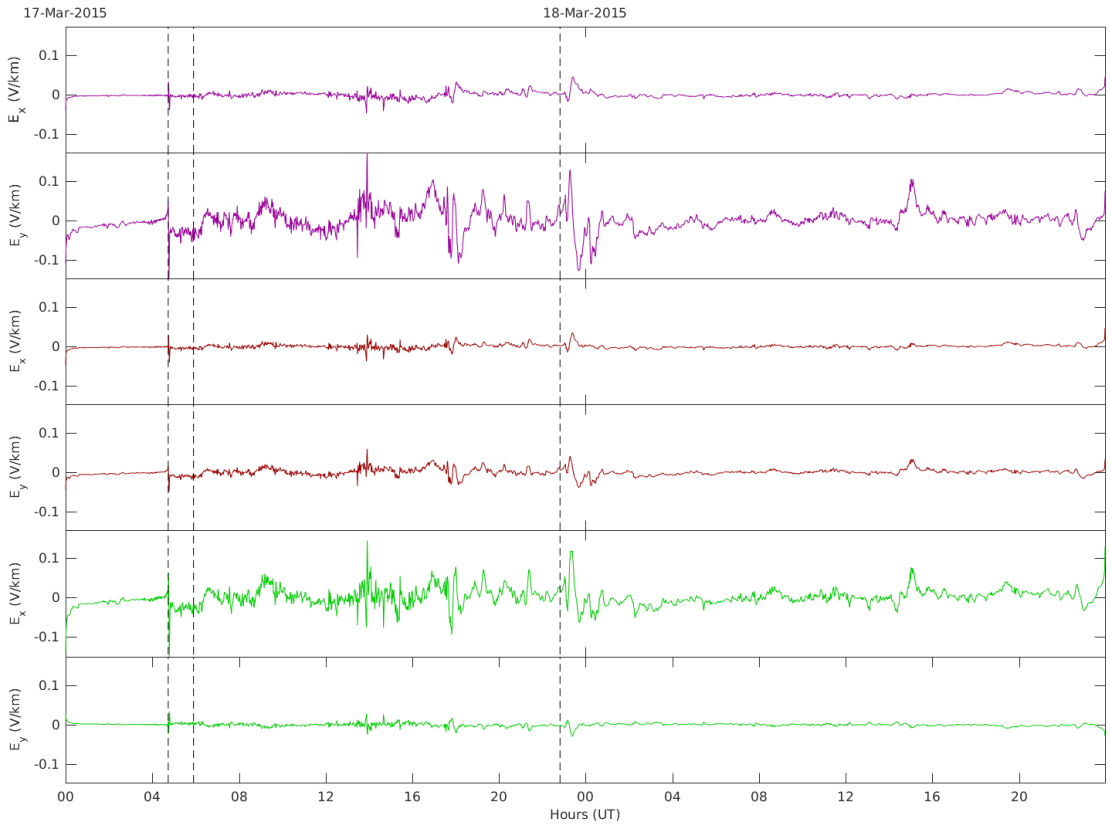

Figure 4.20: Induced Electric Field for the storm of March 2015 for the three points highlighted in Figure 4.17.

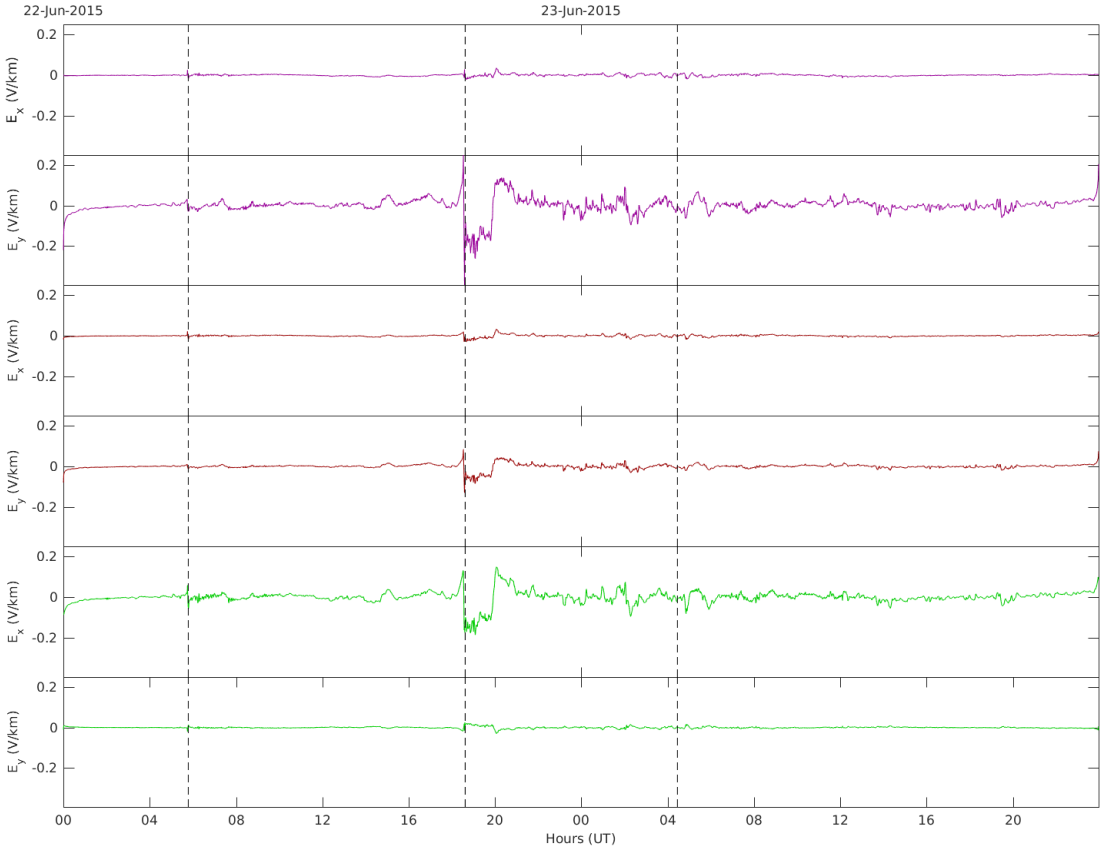

Figure 4.21: Induced Electric Field for the storm of June 2015 for the three points highlighted in Figure 4.17.

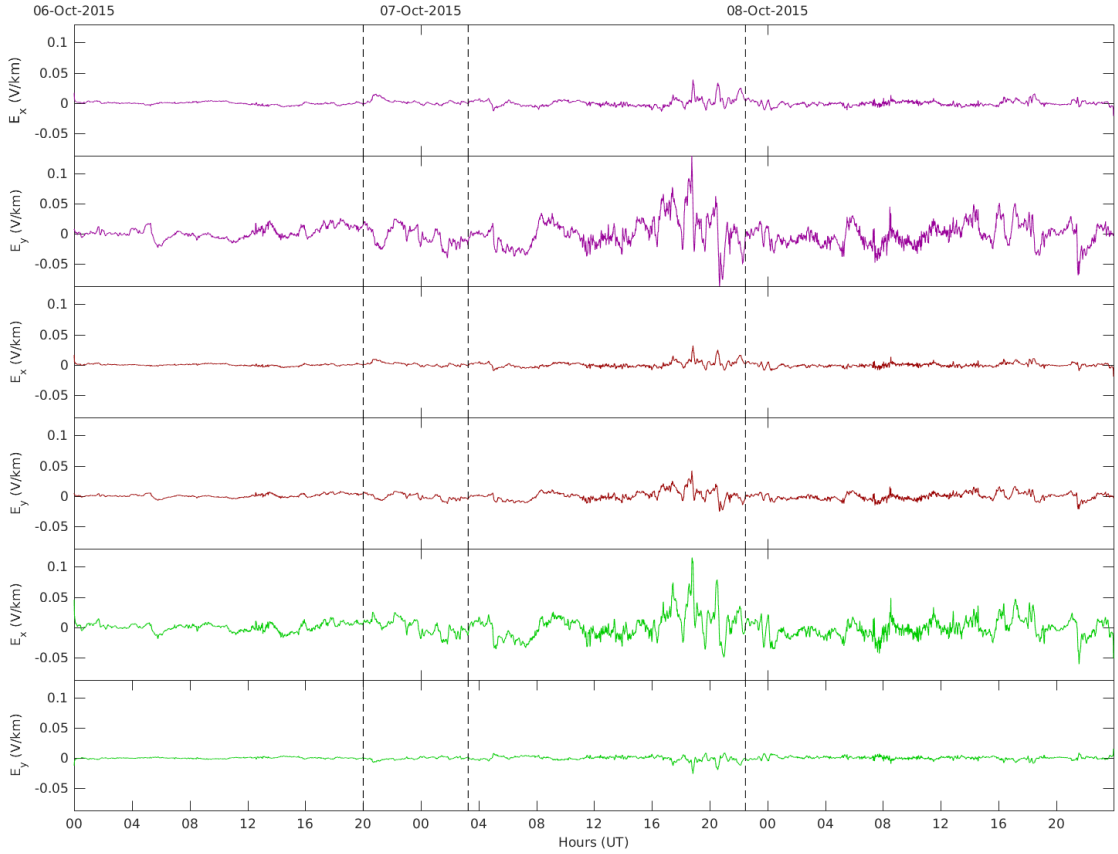

Figure 4.22: Induced Electric Field for the storm of October 2015 for the three points highlighted in Figure 4.17.

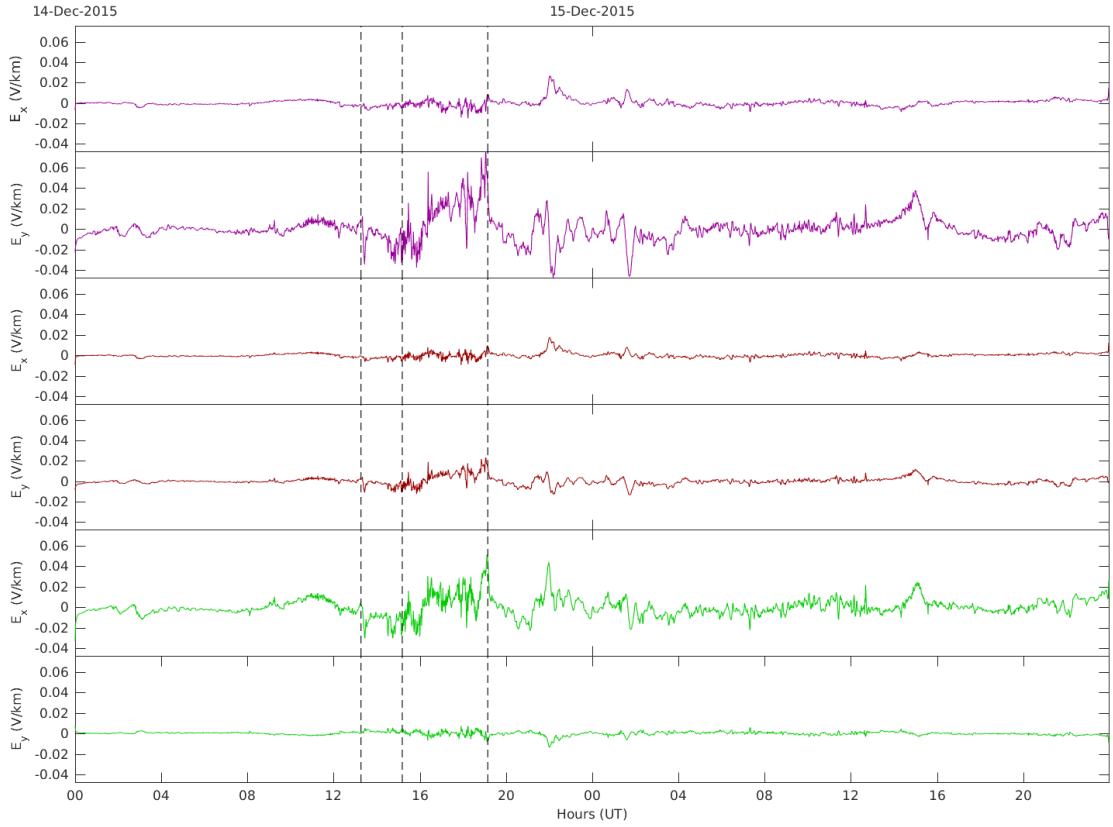

Figure 4.23: Induced Electric Field for the first storm of December 2015 for the three points highlighted in Figure 4.17.

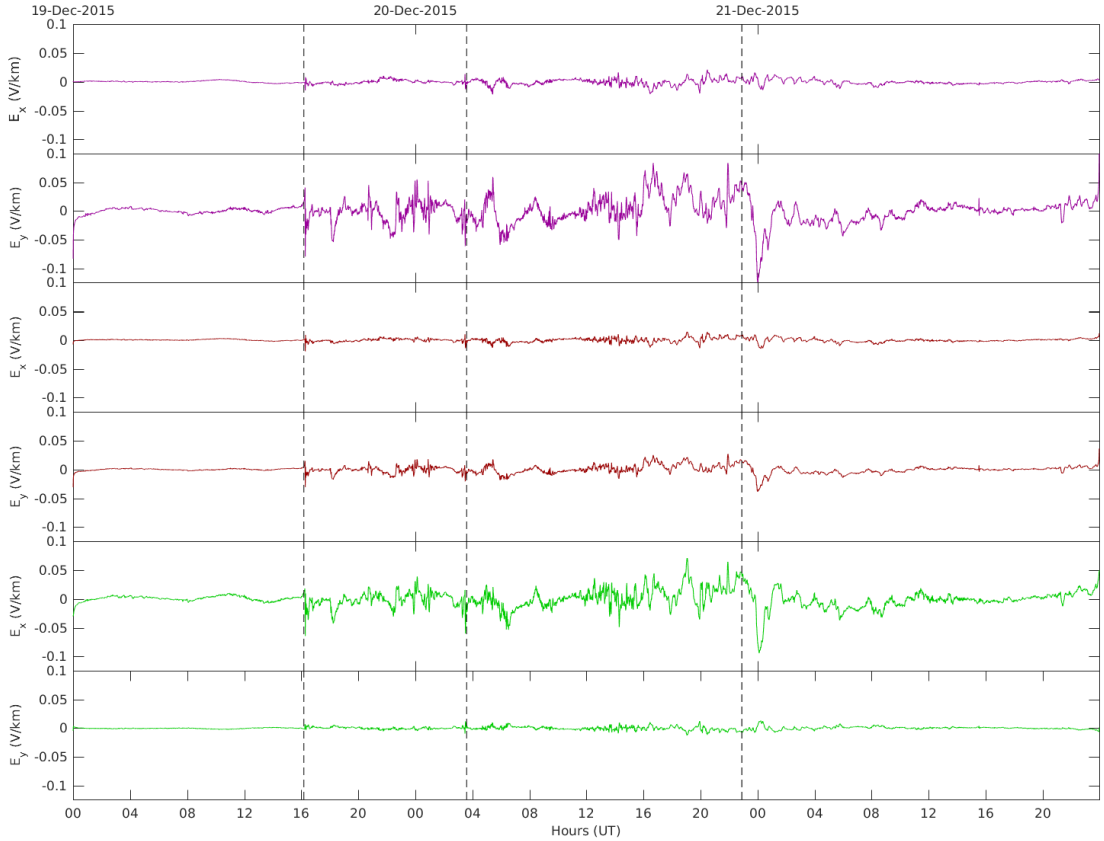

Figure 4.24: Induced Electric Field for the second storm of December 2015 for the three points highlighted in Figure 4.17.

Being the E_x the north-south and E_y the east-west components of the geoelectric field, some differences between the considered points can be observed on the plots on Figures 4.20 to 4.24. For the point in the west coast (purple), the E_y component is larger than E_x, while for the point on the south coast (green) the opposite is true. This is explained by their proximity to discontinuities in the conductivity values (separation between two regions with different conductivities). The electric field at the point located far from the coast (red) and from conductivity discontinuities, has both components with the same order of magnitude. This behavior for each point was verified for every storm in this study.

As can be seen in Figure 3.7 (subsection 3.3.3), the following condition applies at coastlines:

$$\mathbf{j} \cdot \hat{n} = \sigma_1 \mathbf{E}_1 \cdot \hat{n} = \sigma_2 \mathbf{E}_2 \cdot \hat{n} = constant \tag{4.7}$$

due to the continuity of the conduction currents (Equation(3.8)) and where $\hat{n}$ is normal to the discontinuity surface. This relation explains that when there is a discontinuity ($\sigma_1 \neq \sigma_2$) there is also a change in the electric field in order to compensate and maintain the continuity of the conduction currents. This relation explains the variations in the induced electric field observed above: for the point near the west coast there is a change in the y-component, due to a smaller conductivity in the continent an leading to a higher electric field there; on the other hand, for the point at the south coast, that difference is

in the x-component, leading to a higher x-component of the induced electric field.

Another way to see the results for the induced electric field is to plot the induced horizontal electric field over southern Portugal for a certain instant. The time instants chosen are the ones marked in the plots above, which corresponds to the instant that define the SSC, i.e. the begin of the initial phase, the one that defines the end of the initial phase and beginning of the main phase and, at last, the one that defines the end of the main phase.

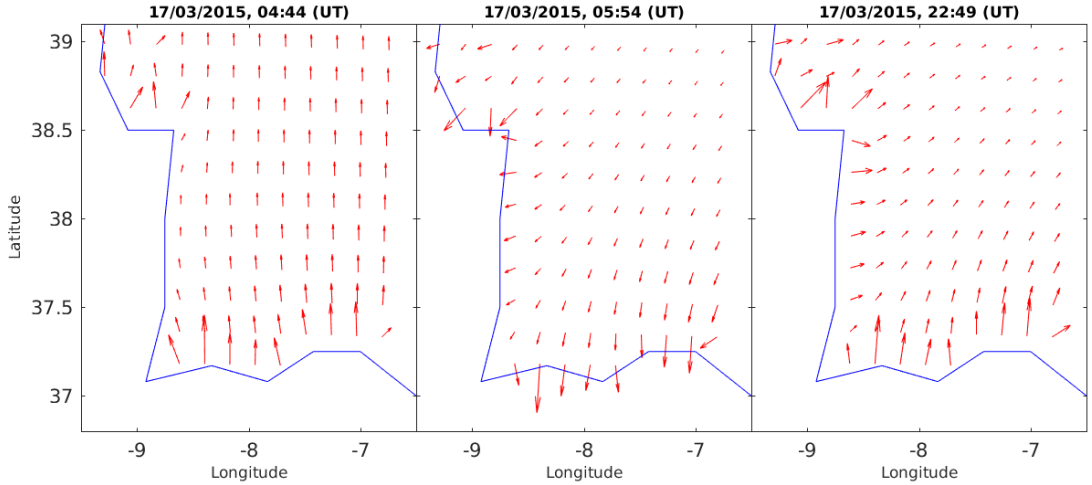

Figure 4.25: Grid of the induced horizontal electric field over southern Portugal for the storm of March 2015.

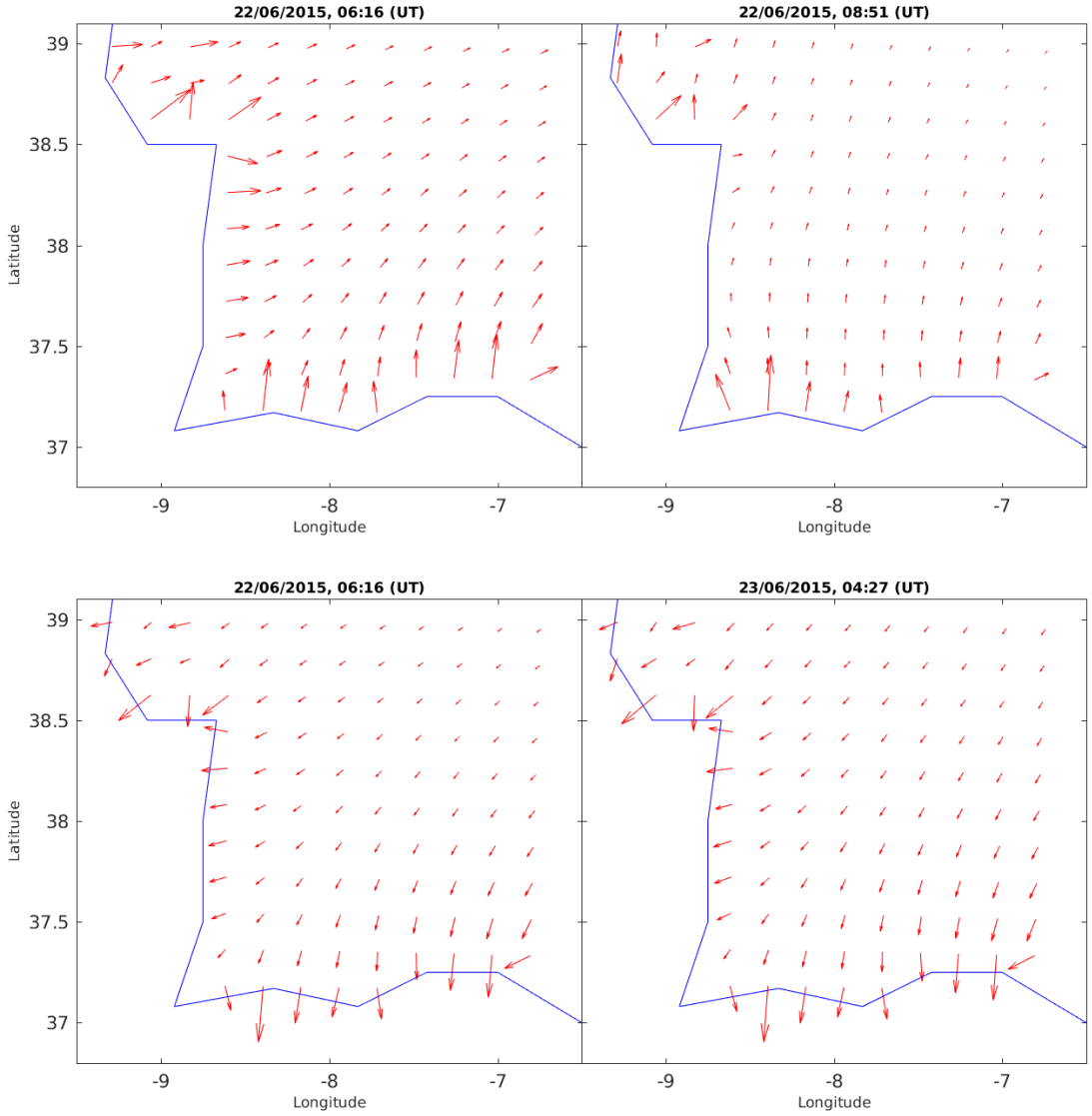

Figure 4.26: Grid of the induced horizontal electric field over southern Portugal for the storm of June 2015.

As can be seen in Figure 4.11, this storm shows an overlap of phases, resulting in a sudden impulse in the middle of the main phase that other storms do not have, making Figure 4.26 to have one more instant when it is relevant to show the behavior of the induced electric field.

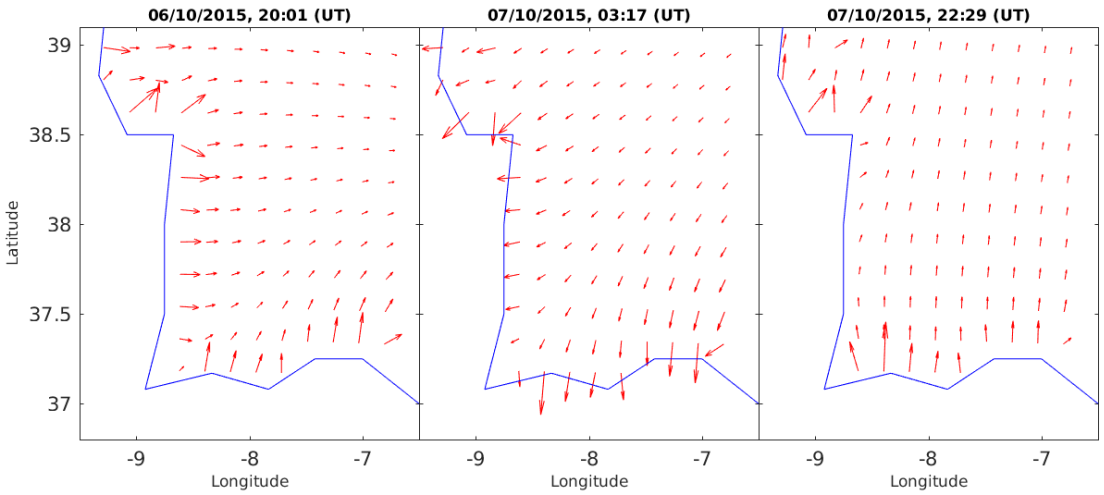

Figure 4.27: Grid of the induced horizontal electric field over southern Portugal for the storm of October 2015.

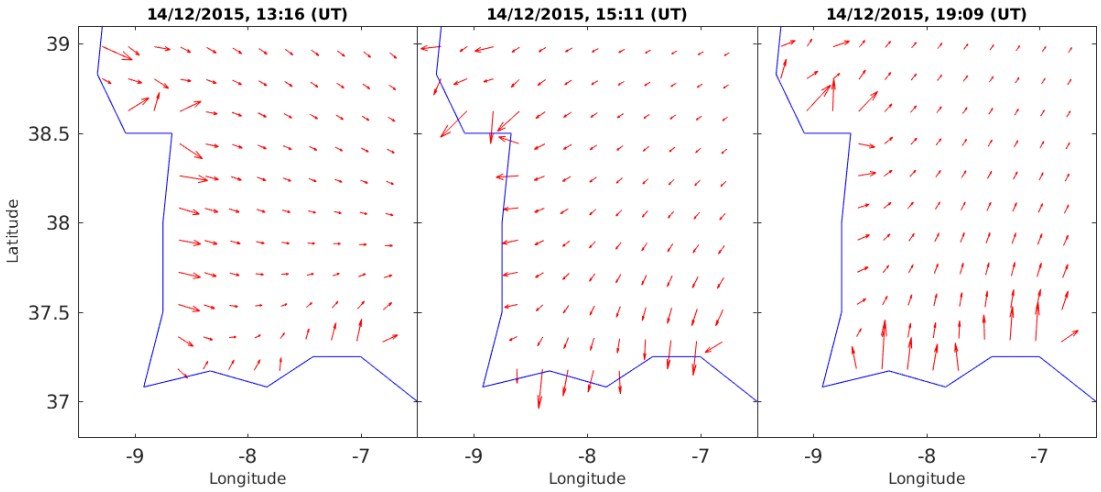

Figure 4.28: Grid of the induced horizontal electric field over southern Portugal for the first storm of December 2015.

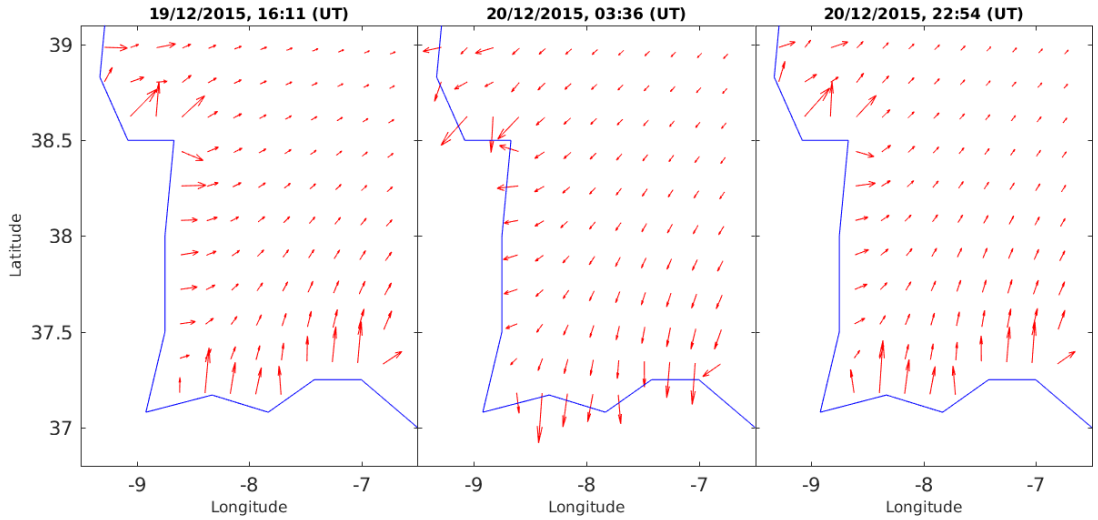

Figure 4.29: Grid of the induced horizontal electric field over southern Portugal for the second storm of December 2015.

As can be seen in Figures 4.25 to 4.29, the horizontal electric field has the same behavior for all storms. The first and last instants (left and right plot on each Figure, respectively) display the same direction of the horizontal component of the electric field, while the opposite direction is observed at the end of the initial phase and beginning of the main phase (middle plot on each Figure). This can be explained through the behavior of the SYM-H variation in time, with the first and last instants having a minimum (local or absolute) followed by an increase in this parameter, while the intermediate instant displays a maximum (local or absolute) followed by a decrease of the SYM-H.

Chapter 5

Geomagnetic Induced Currents

Geomagnetic Induced Currents (GICs) are currents induced in the Earth and grounded conductors, by the time variations of the magnetic flux associated to the electric currents in the magnetosphere and ionosphere, during space weather events. To study these GIC currents there are two inputs needed: an Earth conductivity model (MT method, Chapter 3) and the time-dependent magnetic field (Geomagnetic Storms, Chapter 4).

Frequencies in the GIC spectrum usually range from 10^{-5} to 1.0 Hz, at lower frequencies the variations are too slow to produce significant GIC, while at higher frequencies the power system inductances will have a damping effect (Boteler and Pirjola, 2017). As a result they can be treated as quasi-DC currents.

5.1 GICs on Power Systems

When the Earth's magnetic field changes with time due to solar effects, an electric field is induced in the ground (see Chapter 4). The grounded transformers and the low resistance transmission lines to which they are connected do effectively serve as a short-circuit for ground currents (see Figure 5.1). Once the GIC flows through the network, it is distributed according to Kirchoff and Ohm's laws, which depend on the topology and resistance of the network. It is the current flowing through the transformers that can cause damage and disruption to the network. (Blake, 2017)

The core saturation on a transformer, caused by the flowing of GICs, can cause: (Boteler and Pirjola, 2014; Pulkkinen et al., 2017; Thorberg, 2012)

- increased reactive power consumption;
- high levels of harmonics in the power system, i.e. distortion of the alternating current (AC), which can lead to loss of production and local or widespread blackouts;
- localized heating of the transformer, that eventually may lead to permanent damage.

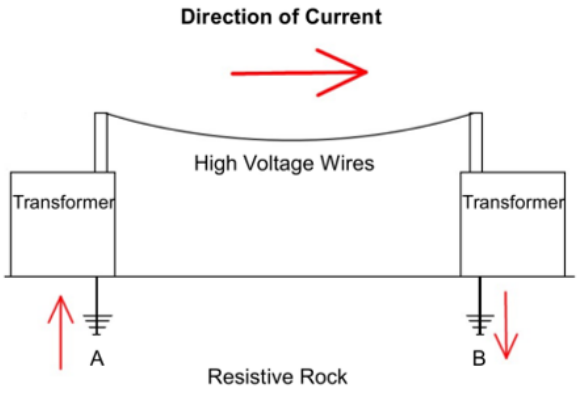

Figure 5.1: Schematics of the GICs flowing through a power system. (Blake, 2017)

5.1.1 Types of transformers

The path through which the GICs flow within the power system network, will depend on the type of transformers on site. There are three types of transformers most commonly used: delta-wye (or 'ΔY' transformers), wye-wye (or 'YY' transformers) and auto-transformers. The 'Δ' configuration does not have a connection to the ground, not allowing GICs to flow. So, ΔY transformers can not couple different network lines (with DC current) and because of that they have no interest for this study (it only be considered the other two types). (Boteler and Pirjola, 2014; Koen and Gaunt, 2003)

The YY transformers and the auto-transformers are both Y-connected transformers where the windings for the three phases are connected together at a neutral point, which is connected to ground (Figure 5.2), providing a path for GIC. The main difference between them is that for the 'YY' there are separate windings for the high and low voltage sides while the auto-transformers have a common winding for both voltages. (Boteler and Pirjola, 2014)

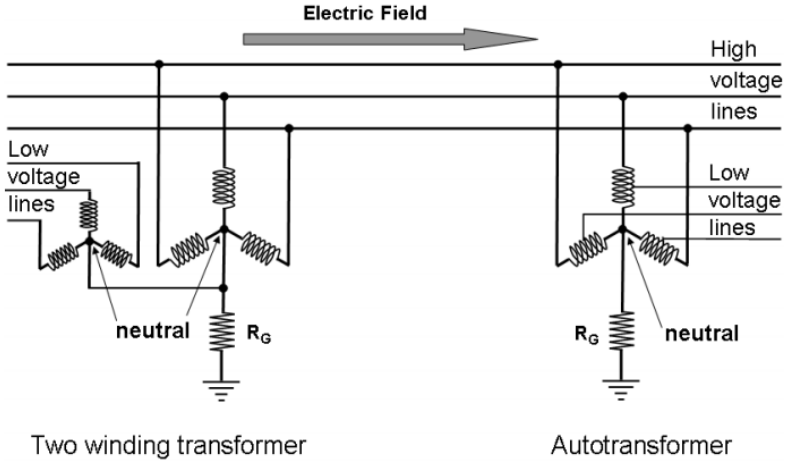

Figure 5.2: Three-phase transmission lines and substations with a two-winding transformer and an auto-transformer. (Boteler and Pirjola, 2014)

The AC power currents in the three-phase transmission lines have the same amplitude but are out of phase and sum to zero at the neutral point. This implies that there is no AC flowing from the neutral point to the ground. During the storms there is an increase of DC currents in the lines and transformers, and the neutral-ground connections are there to provide a safe discharge path for these currents, allowing GIC to flow out of the transformer windings to the ground. (Boteler and Pirjola, 2014)

5.2 GIC Modeling

In order to build a network model for calculating GICs in a power system it is necessary to set up the electric circuit, for which it is required the position of transformers, the transformer winding resistances, the substation grounding resistances, the connections between substations and the resistances of the connections between substations. (Blake et al., 2018)

However, it is possible to simplify the model, on a first look, by noticing that the impedances of each phase of the power system are identical, experiencing the same levels of GIC. This means that it is only necessary to make calculations for a single phase by combining the parallel paths of the three-phase transmission lines and transformer windings into equivalent combined values and then dividing their resistances by three to give the GIC value per phase (Boteler and Pirjola, 2014):

$$\frac{1}{R_{eq}} = \sum_{n=1}^{3} \frac{1}{R_n} \Leftrightarrow R_{eq} = \frac{R}{3} \tag{5.1}$$

where R_{eq} is the equivalent circuit resistance and R the resistance of each phase line.

5.2.1 The Lehtinen and Pirjola (LP) method

The LP method is the way to compute GICs introduced by Lehtinen and Pirjola in 1985 (Lehtinen, 1985) and consists in treating the power grid as a discretely earthed network and applying Ohm and Kirchhoff's laws to it. This method can be used on any power network once the network's transformers and connections are known. (Blake, 2017)

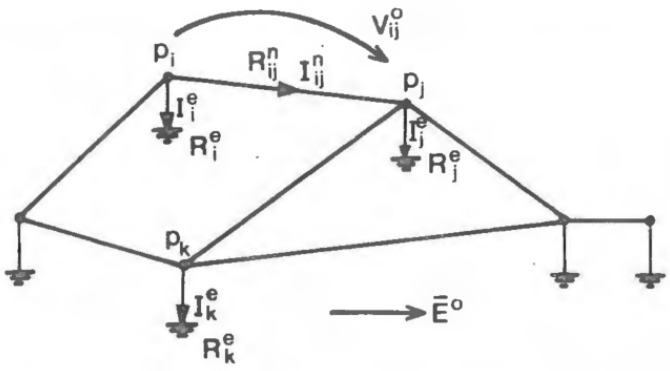

Figure 5.3: Example of a power circuit by Lehtinen (1985) in order to introduce the used nomenclature.

The Figure 5.3 symbols are:

- p_i ,p_j, p_k: nodal (earthing) points;
- s_{ij}: path on the earth's surface which lies directly below (or above) the network segment from p_i to p_j;
- R_i^e: earth resistance of nodal point p_i;
- $R_{ij}^n = R_{ji}^n$: resistance in the network segment (n) that connects nodal points p_i and p_j. When the two nodal points are not connected, $R_{ij}^n \to \infty$;
- $\mathbf{E}^0(\mathbf{r}, t)$: horizontal electric field induced at the earth's surface;
- $V_{ij}^0 = \int_i^j \mathbf{E}^0 \cdot dl = -V_{ji}^0$: the open-circuit ddp between nodal points p_i and p_j. When $V_{ij}^0 > 0$ it means that the electric potential of p_i is larger than p_j;
- $V_{ij} = -V_{ji}$: close-circuit ddp between nodal points p_i and p_j;
- U_i^{cur}: electric potential of nodal point p_i with respect to earth;
- I_i^e: current flowing from node p_i to the ground;
- I_{ij}^n: current flowing from node p_i to node p_j, along segment n.

Recalling the Kirchhoff Law's:

- *Kirchhoff's voltage law* (or loop rule): the sum of all voltage differences around any closed loop in a circuit must equal zero.
- *Kirchhoff's current law* (or nodal rule): the whole current flowing into the node must be equal to the whole current flowing out of it.

and applying them to the circuit in Figure 5.3 it comes, respectively:

$$V_{ij} + U_j^{cur} - V_{ij}^0 - U_i^{cur} = 0 \tag{5.2a}$$

$$\sum_{j \neq i} I_{ji}^n = I_i^e \tag{5.2b}$$

According to Faraday's law of induction, the line integral of the electric field along the loop is given by (as seen in Equation (4.4)):

$$\oint \mathbf{E}^0 \cdot d\mathbf{l} = -\int \frac{\partial \mathbf{B}}{\partial t} \cdot d\mathbf{a} \tag{5.3}$$

where, in this case, the loop integral reduces to the line integral between nodal points p_i and p_j (see Section 4.3 and Figure 5.4):

$$V_{ij}^0 = \int_i^j \mathbf{E}^0 \cdot \mathrm{d}\mathbf{l} \tag{5.4}$$

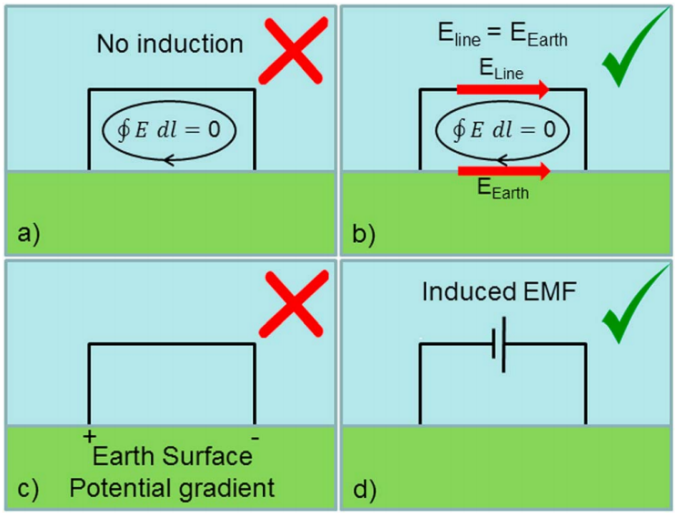

Figure 5.4: Schematic explanation of the Faraday's law for the induced electric field on the surface of the Earth. (Boteler and Pirjola, 2017)

As seen before, with Faraday's law it is possible to relate the electric field through a loop that goes deep into the ground with the variation rate of the magnetic field through that same loop (Boteler and Pirjola, 2017). Figure 5.4 shows that even if the integral is null along the much smaller loop connecting the line and the Earth surface, there can be induction. In other words, the integral is null because the electric field in the transmission line has the same magnitude and direction than the electric field along the surface. (Boteler and Pirjola, 2017)

Using Ohm's Law,

$$V_{ij} = R^n_{ij} I^n_{ij} \tag{5.5a}$$
$$U^{cur}_i = R^e_i I^e_i \tag{5.5b}$$
$$U^{cur}_j = R^e_j I^e_j \tag{5.5c}$$

that can be used in Equation (5.2a) leading to

$$I^n_{ij} = \frac{1}{R^n_{ij}}(V^0_{ij} + R^e_i I^e_i - R^e_j I^e_j) \tag{5.6}$$

Replacing Equation (5.6) in Equation (5.2b):

$$I^e_i = -\sum_{j \neq i} \frac{1}{R^n_{ij}}(V^0_{ij} + R^e_i I^e_i - R^e_j I^e_j) \Leftrightarrow$$

$$\Leftrightarrow I^e_i = R^e_j I^e_j \sum_{j \neq i} \frac{1}{R^n_{ij}} - R^e_i I^e_i \sum_{j \neq i} \frac{1}{R^n_{ij}} - \sum_{j \neq i} \frac{V^0_{ij}}{R^n_{ij}} \tag{5.7}$$

The last element of this equation was introduced by Lehtinen (1985) as the vector of perfect earthing currents,

$$J^e_i = -\sum_{j \neq i} \frac{V^0_{ij}}{R^n_{ij}} \tag{5.8}$$

Lehtinen (1985) also introduced the network admittance matrix,

$$Y_{ij}^n = \begin{cases} -\dfrac{1}{R_{ij}^n}, & i \neq j \\ \sum\limits_{k \neq i} \dfrac{1}{R_{ik}^n}, & i = j \end{cases} \tag{5.9}$$

Replacing Equations (5.8) and (5.9) in Equation (5.7):

$$I_i^e = J_i^e - \sum_j Y_{ij}^n R_j^e I_j^e \tag{5.10}$$

and using the Kronecker's Delta:

$$\delta_{kj} = \begin{cases} 0, & i \neq j \\ 1, & i = j \end{cases} \tag{5.11}$$

it comes

$$R_j^e I_j^e = \sum_k \delta_{jk} R_k^e I_k^e = \sum_k Z_{jk}^e I_k^e \Rightarrow Z_{ij}^e = \delta_{ij} R_j^e \tag{5.12}$$

Z is the earthing impedance matrix (Lehtinen, 1985). It also came that $I_i^e = \sum_k \delta_{ik} I_k^e$ which replacing in Equation (5.10) together with the impedance gives:

$$J_i^e = \sum_k \delta_{ik} I_k^e + \sum_j \sum_k Y_{ij}^n Z_{jk}^e I_k^e \tag{5.13}$$

This equation it is just for one node, so considering all of them it gives a matrix system: (Lehtinen, 1985)

$$\mathbf{I}^e = (\mathbf{1} + \mathbf{Y}^n \mathbf{Z}^e)^{-1} \mathbf{J}^e \tag{5.14}$$

where $\mathbf{1}$ is the identity matrix, $\mathbf{Y}^n$ the network admittance matrix that contains information on the resistances for connections between the nodes, $\mathbf{Z}^e$ the earthing impedance matrix that includes the earthing resistances, $\mathbf{I}^e$ the GICs in earthings connections and $\mathbf{J}^e$ the vector of the perfect earthing currents which has the information on the currents arising from the geoelectric field.

5.3 The Portuguese south region network case

The portuguese south region has in its power network 20 substations to the south of Palmela (Figure 5.5) and all the information about them that is required to apply the LP-method (as stated in Section 5.2) was given by the national power network operator REN (portuguese acronym for National Energy Networks).

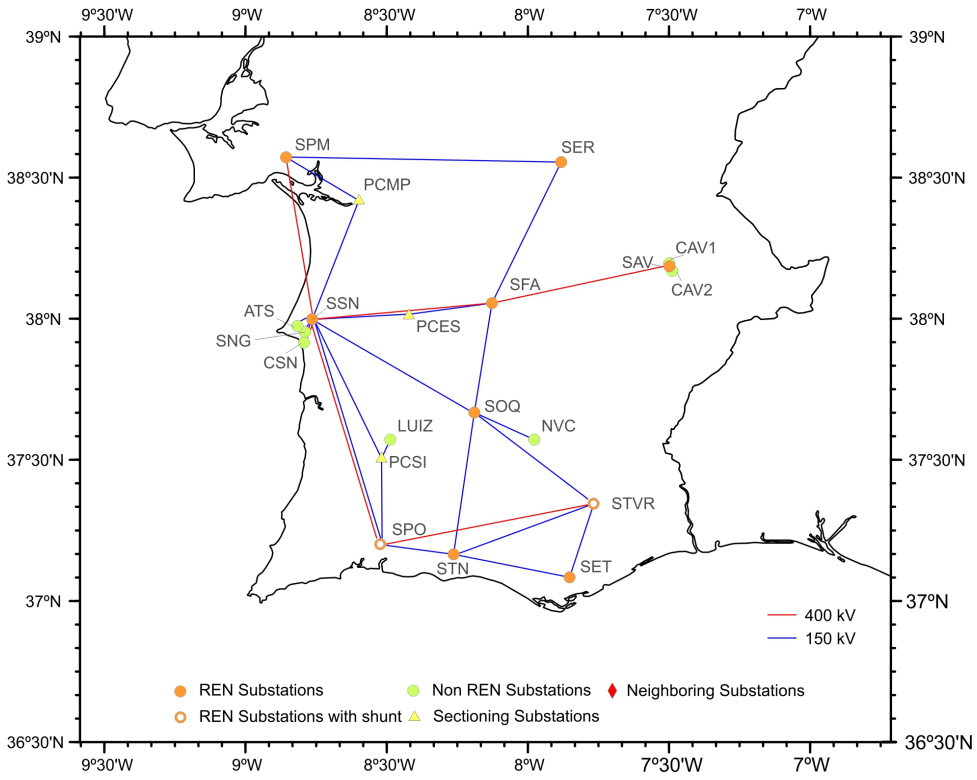

Figure 5.5: Portuguese south region network. (Alves Ribeiro et al., 2020).

The algorithm used to compute the GICs in the Portuguese south region can be seen in Figure 5.6. Due to a confidentiality agreement between UC and REN, the network model is not the real one, the earthing resistance for all the substations are a standard value of 0.20 Ω and for the windings resistances it was introduced a systematic error of 3% and a random one of 5%.

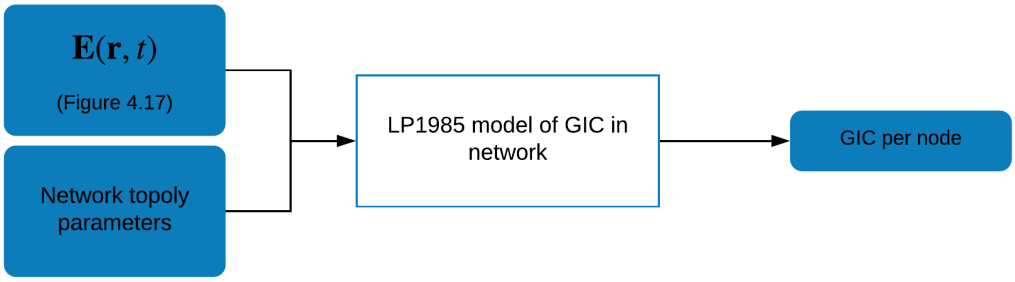

Figure 5.6: Algorithm to compute GICs adapted from GEOMAGICA from Bailey et al. (2017).

In a first approach where the focus is on the effect of the network topology, a uniform induced electric field of $E = 1\text{V/km}$ is considered. It is possible to determine which substations in a power network are more susceptible to GICs in a certain direction. Computing the northward ($E_N = |E|\cos\theta$) and the eastward ($E_E = |E|\sin\theta$) components of this field allows to determine the GIC produced by those components, at a station i, for

$0 < \theta < 360^{o}$ the angle between **E** and the North direction: (Boteler, 2013)

$$GIC_i = \alpha_i \mid E \mid \cos\theta + \beta_i \mid E \mid \sin\theta \tag{5.15}$$

In the above equation, α_i and β_i are the GICs produced separately when **E** is along the North-South and East-West direction, respectively. Using this equation it is possible to infer the sensitivity of each substation, and some examples are given in Figure 5.7. That is, it is shown how the effect of the orientation of the 1 V/km electric field affects the intensity of the GIC at each substation.

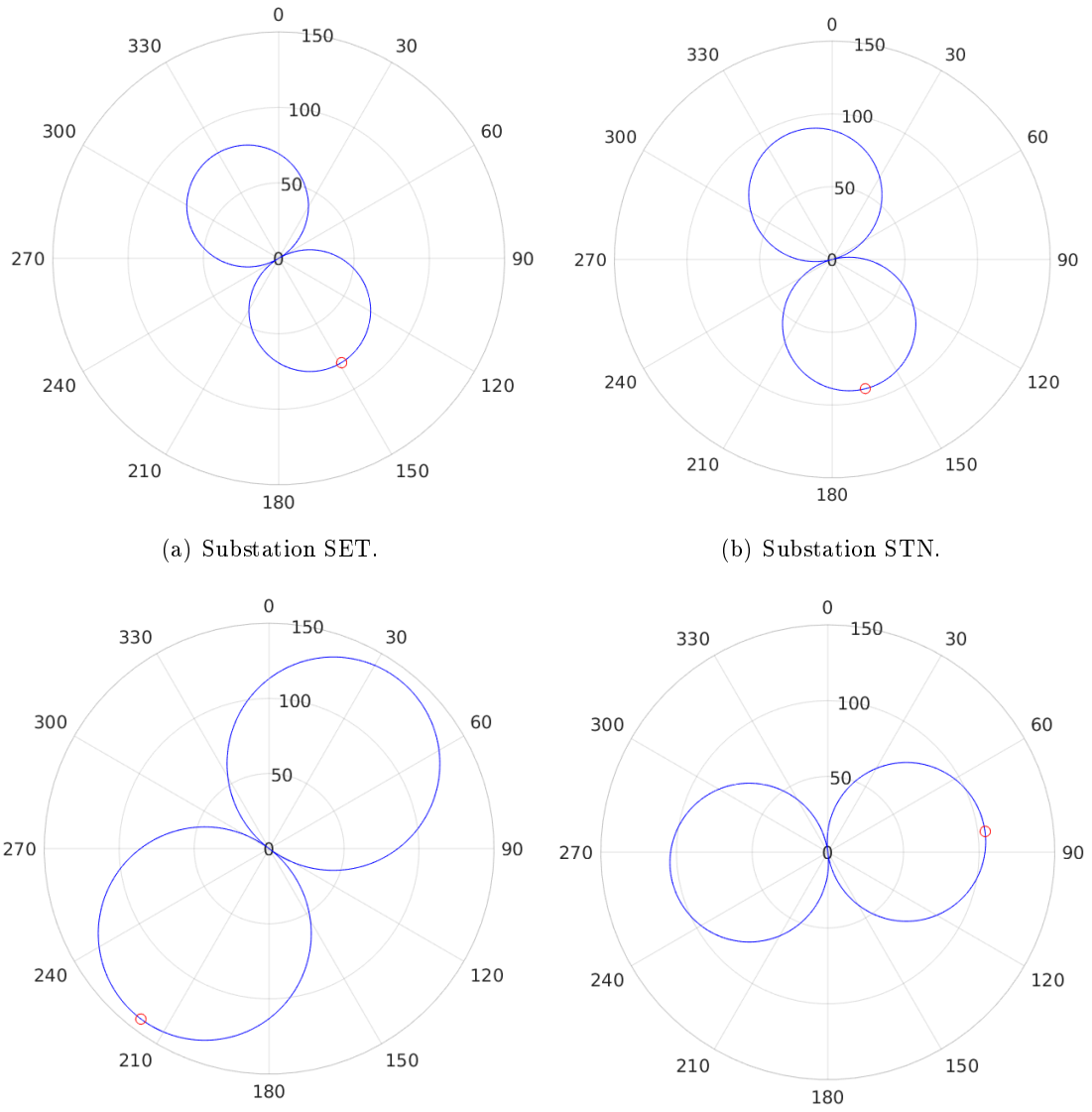

(a) Substation SET.

(b) Substation STN.

(c) Substation SPO.

(d) Substation STVR.

Figure 5.7: Directional sensitivity for four of the twenty substations south of Palmela, with the highest GIC value marked with a red circle.

For the entire power network shown in Figure 5.5, the maximum value of GICs obtained with a uniform electric field with intensity 1 V/km and pointing North and East can be seen in Figure 5.8.

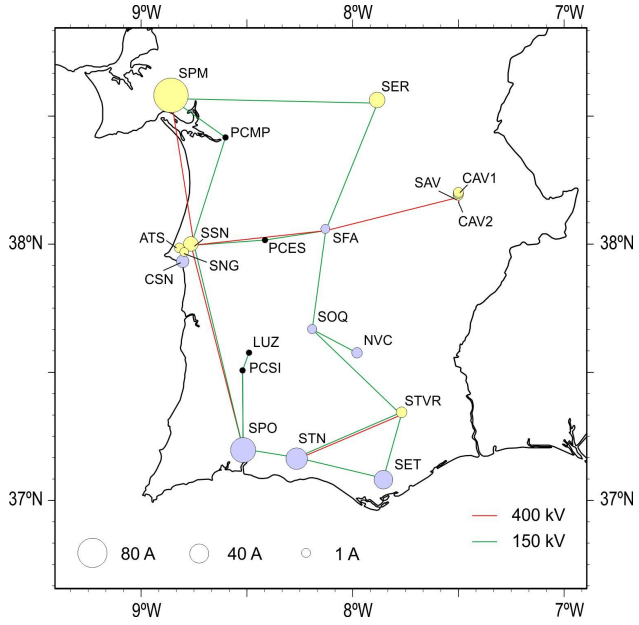

(a)

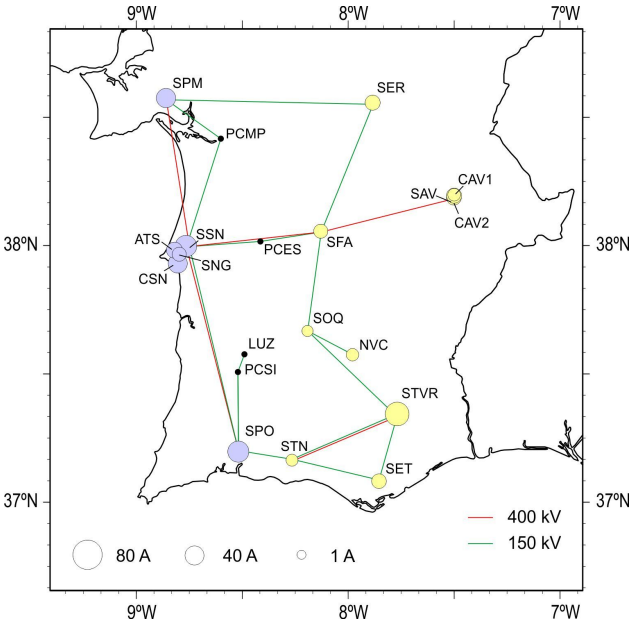

(b)

Figure 5.8: Maximum GIC values distribution for a North (a) and East (b) uniform induced electric field of 1 V/km for all the substations south of Palmela.

The directional GIC sensitivity (Equation (5.15)) allows to determine the intensity and direction of the peak GIC by equating $\frac{\partial GIC_i}{\partial \theta}$ to zero,

$$(GIC_i)_{\text{peak}} = \sqrt{\alpha_i^2 + \beta_i^2}\,|E| \tag{5.16}$$

and

$$(\theta_i)_{\text{peak}} = \arctan\left(\frac{\beta_i}{\alpha_i}\right) \tag{5.17}$$

respectively. Applying these equations to some of the substations, the electric field orientation to which each substation is most sensitive can be seen in Figure 5.9, as well as the maximum GIC values attained.

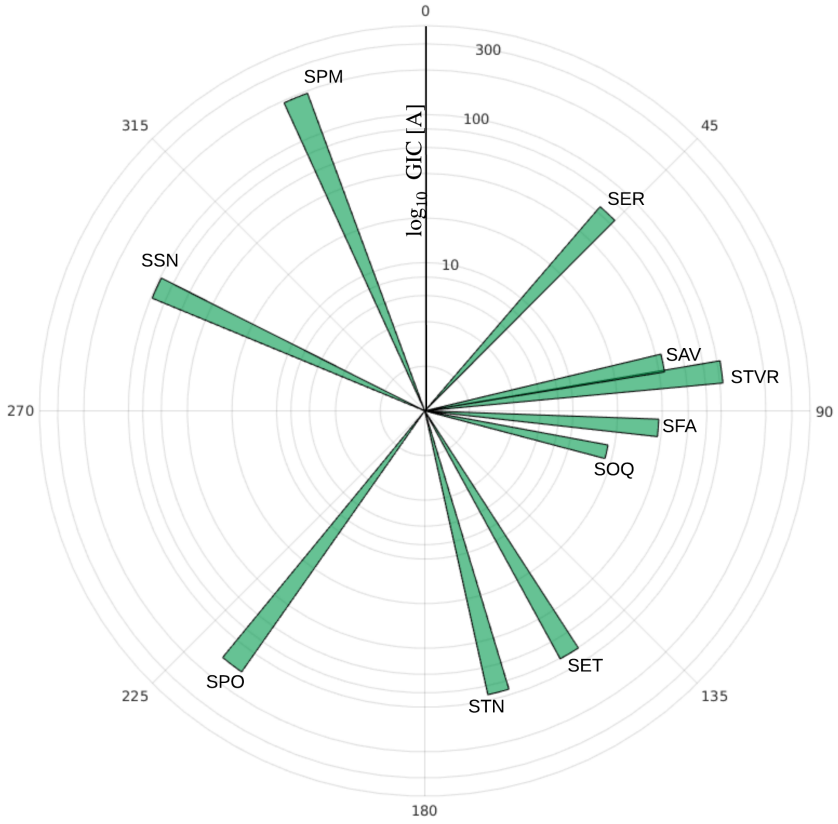

Figure 5.9: Direction of the uniform induced electric field with 1 V/km magnitude that causes the highest GIC for each substation, along with the corresponding GIC intensity.

When information exists, it is more interesting to do a realistic GIC estimation using the geoelectric induced fields obtained in Section 4.4 from the observed geomagnetic storms analyzed in Section 4.2 and an Earth conductivity model. The GICs produced by the E_N and the E_E components of the field can be seen, for each storm and for each substation from Figure 5.9, in Figures 5.10 to 5.14.

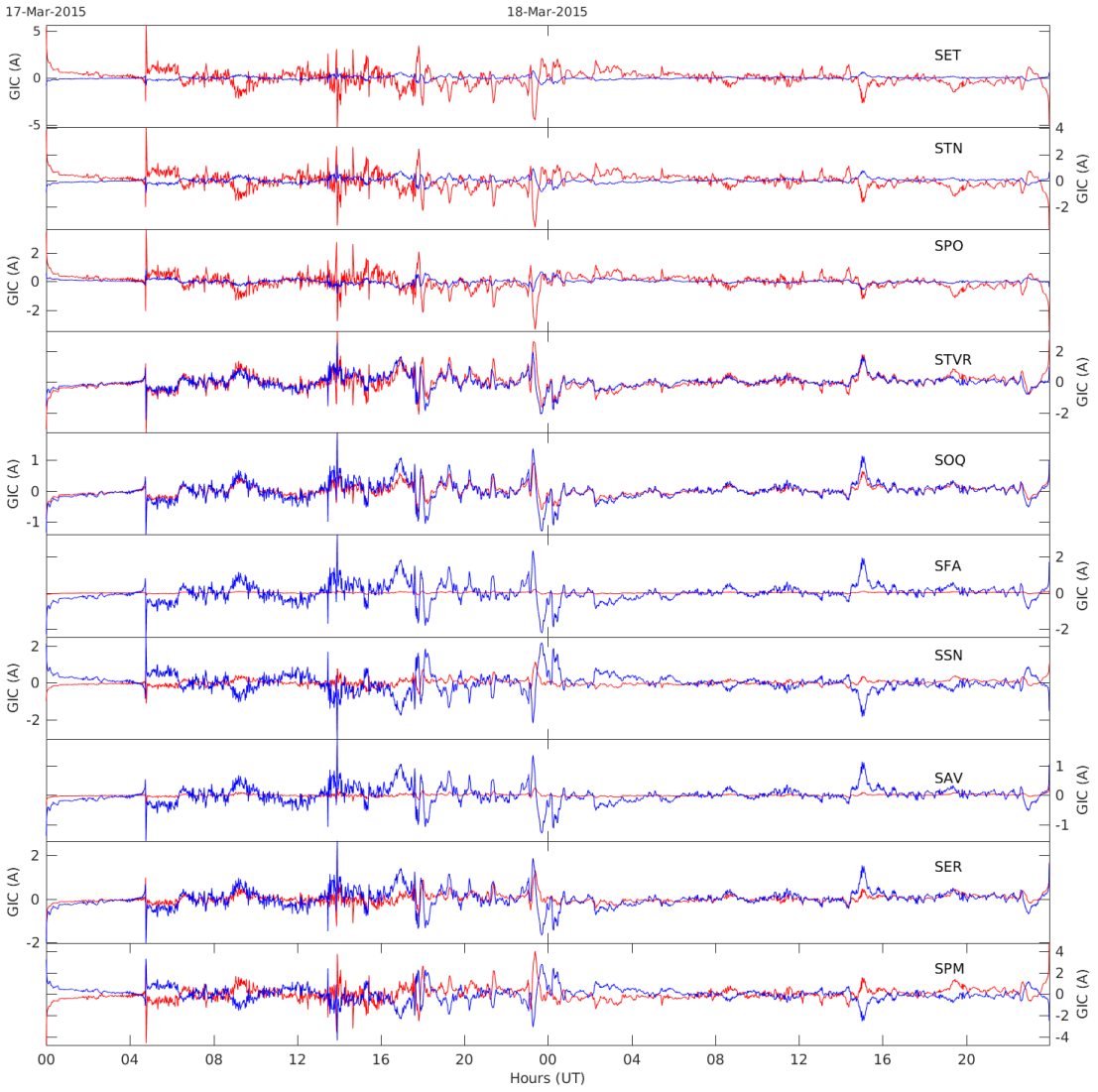

Figure 5.10: GICs produced by the E_N (red) and the E_E (blue) components of the electric field for the St.Patrick's Day storm.

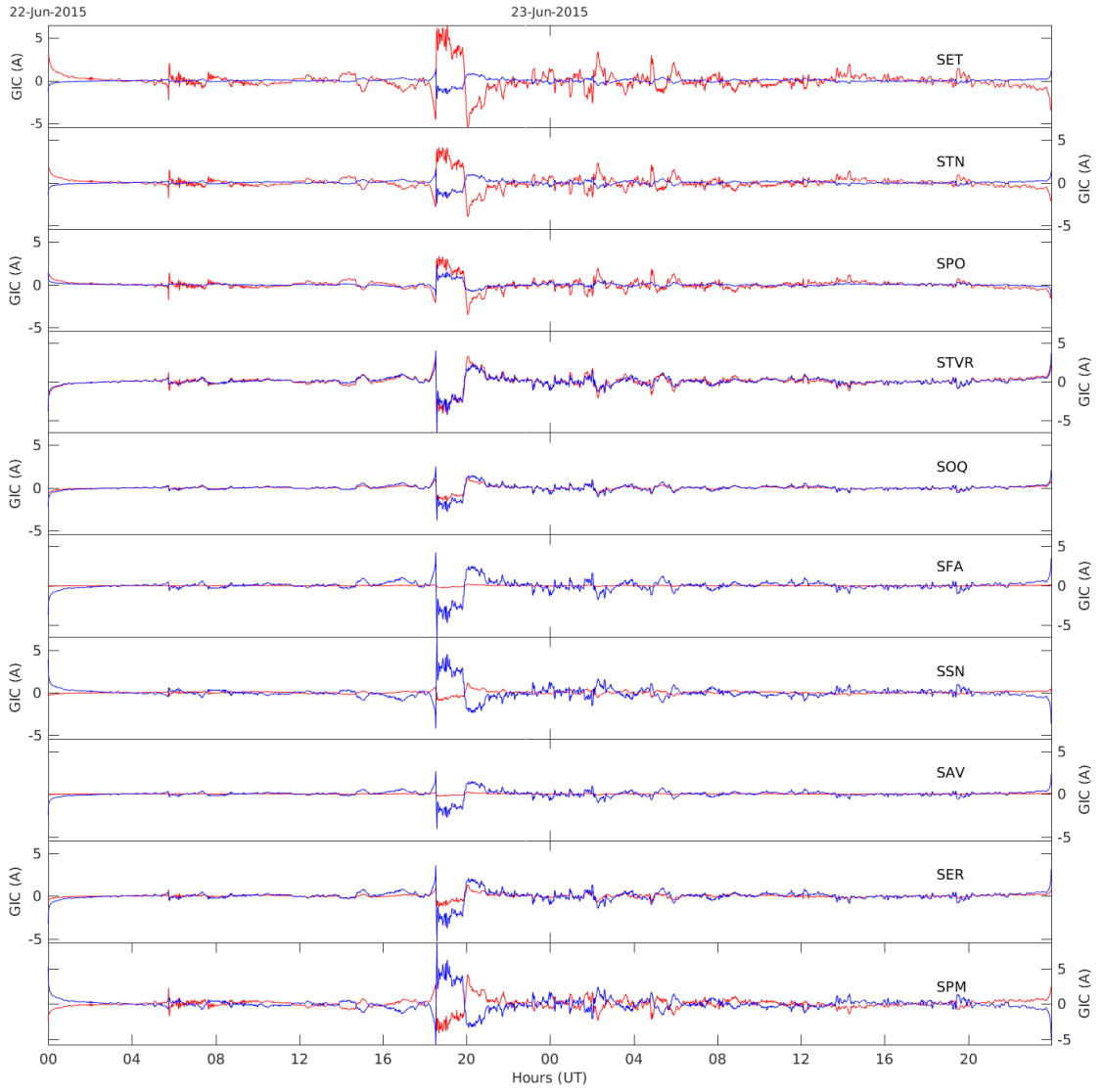

Figure 5.11: GICs produced by the E_N (red) and the E_E (blue) components of the electric field for the storm of June 2015.

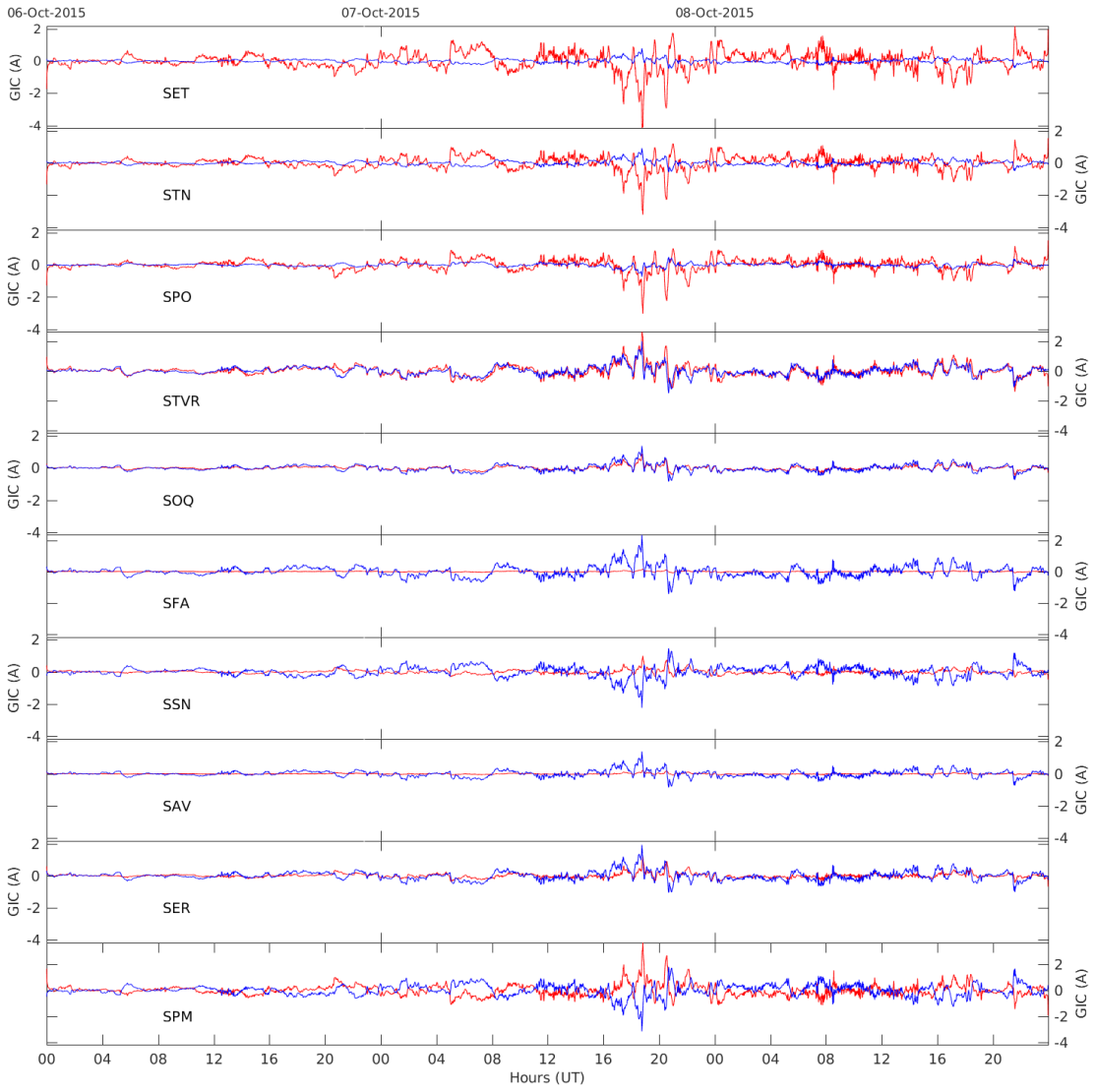

Figure 5.12: GICs produced by the E_N (red) and the E_E (blue) components of the electric field for the storm of October 2015.

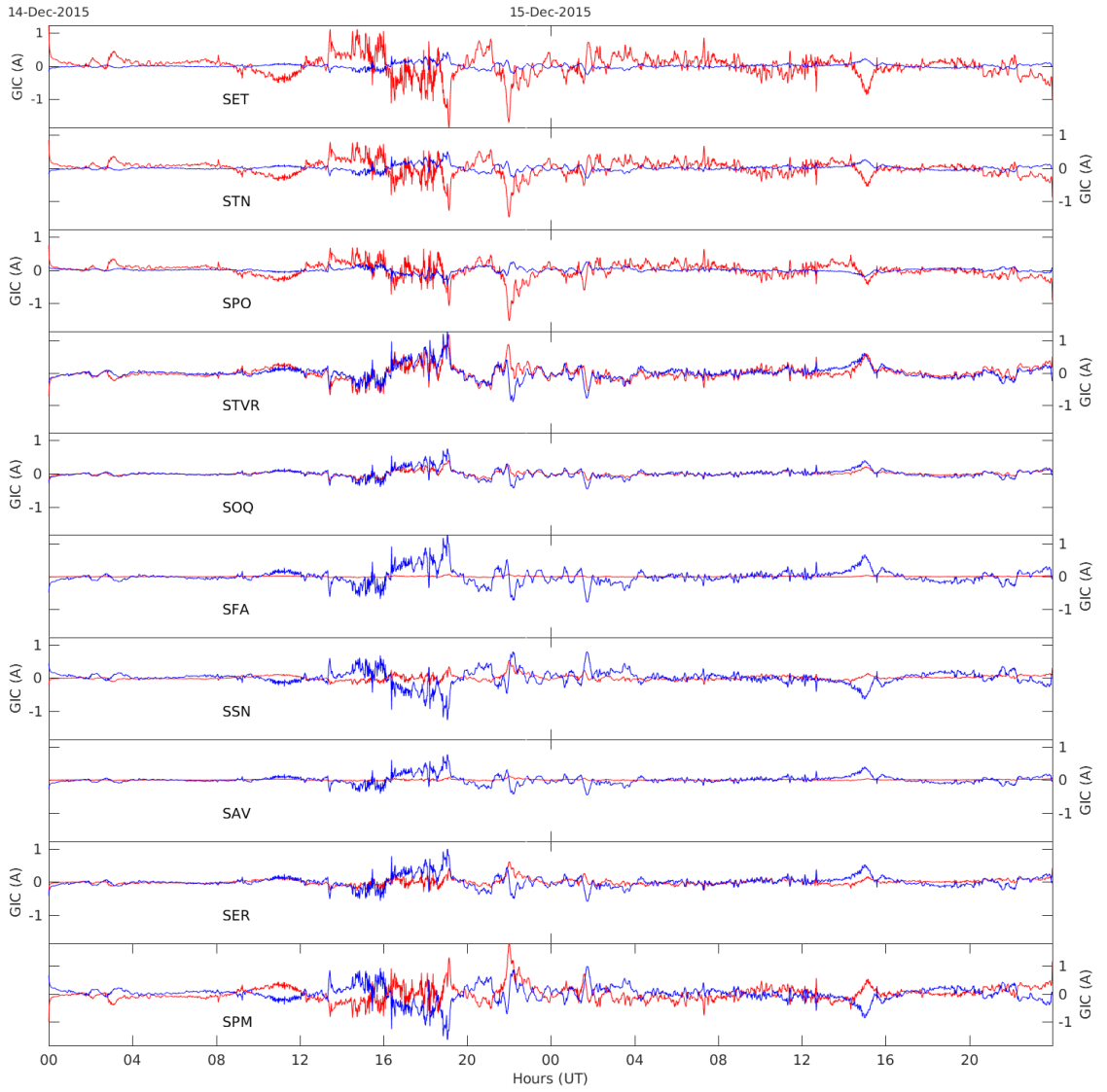

Figure 5.13: GICs produced by the E_N (red) and the E_E (blue) components of the electric field for the first storm of December 2015.

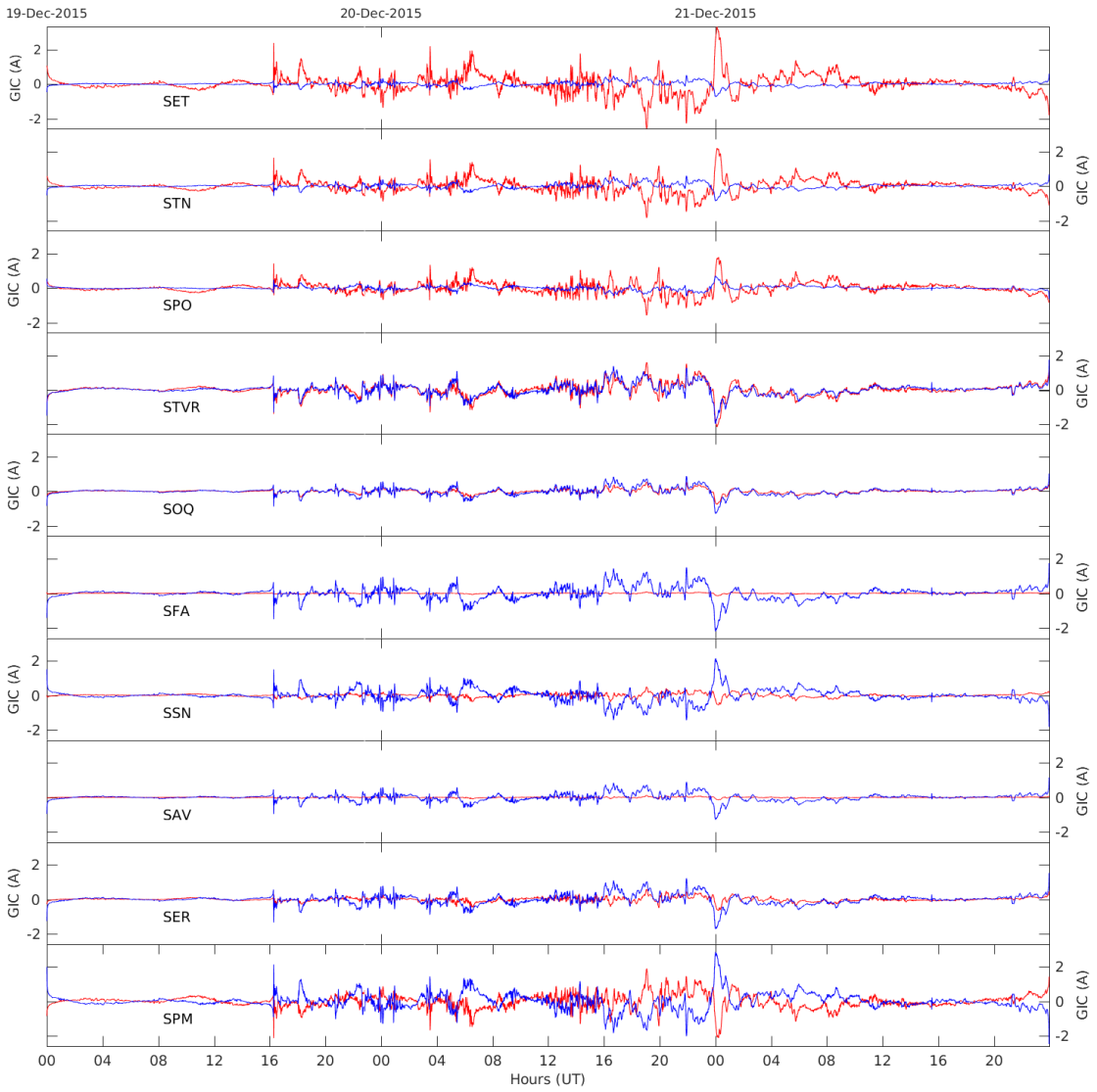

Figure 5.14: GICs produced by the E_N (red) and the E_E (blue) components of the electric field for the second storm of December 2015.

It can be seen from these figures that for the substations near the south coast (SET, STN and SPO), the GIC produced by the E_N component is higher, which is in agreement with the fact that for that location the induced electric field has a predominant northward direction, being perpendicular to the coast as seen in Chapter 4. For the same reason, the substations near the west coast have the GIC produced by the E_E component larger than the other. However, the SPM substation is a special case since it is located near a south and west coast, not having the predominance of one the components. For the remain substations, the ones away from the coast, the GIC produced by E_N component is higher but its magnitude is much lower. Another thing that can be seen is that the SFA and the SAV substations have a larger difference between the GICs produced by the two components, when compared with the others on the interior of the country, due to the 400 **kV** line that connects them.

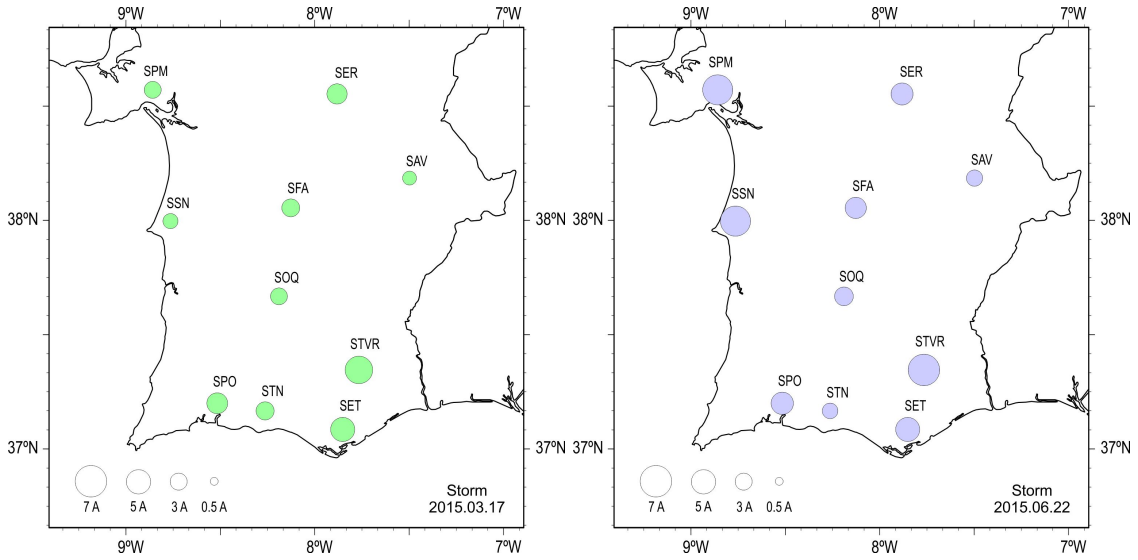

(a) Storm of March 2015

(b) Storm of June 2015

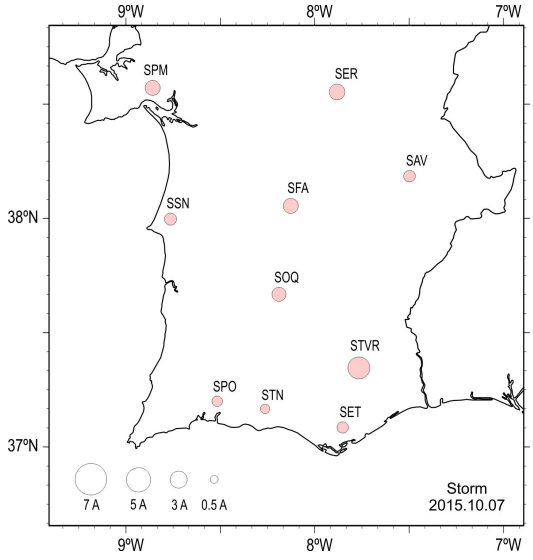

(c) Storm of October 2015

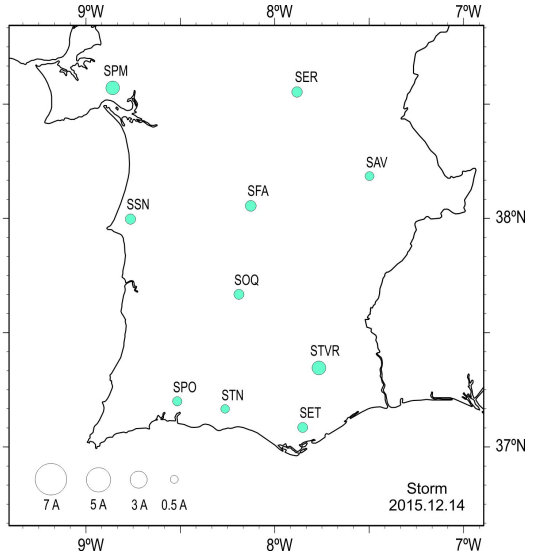

(d) First storm of December 2015

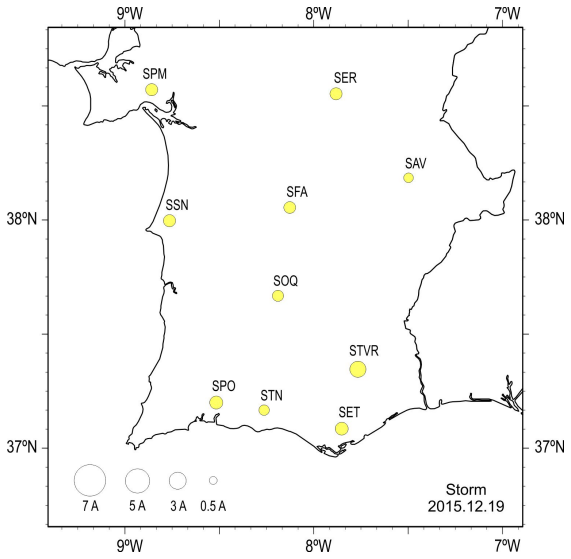

(e) Second storm of December 2015

Figure 5.15: Maximum GIC values per station for the different storms of 2015 in study.

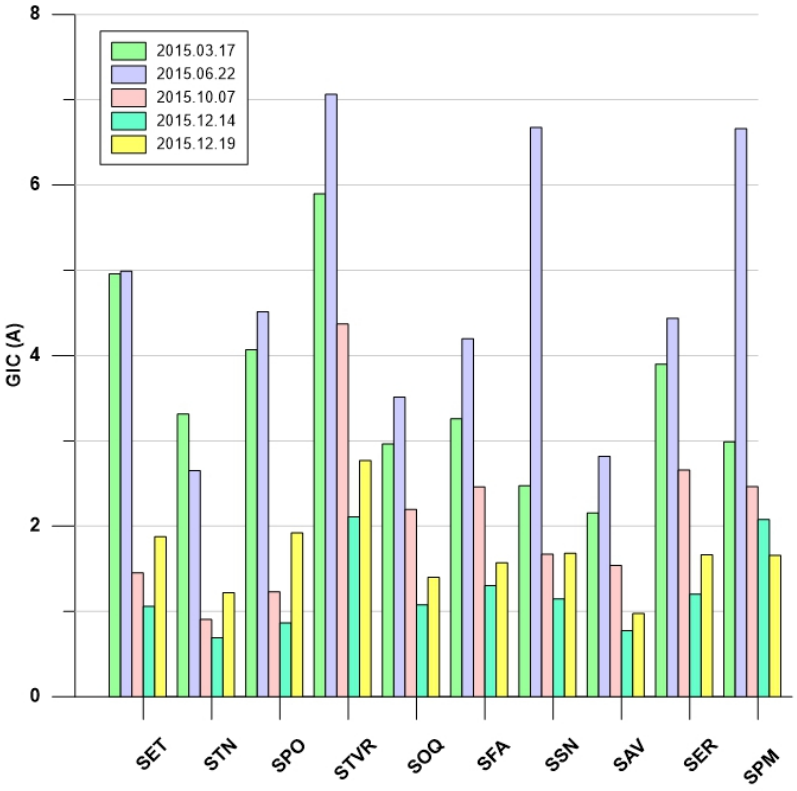

Figure 5.16: Histogram of the maximum GIC values per substation shown in Figure 5.15.

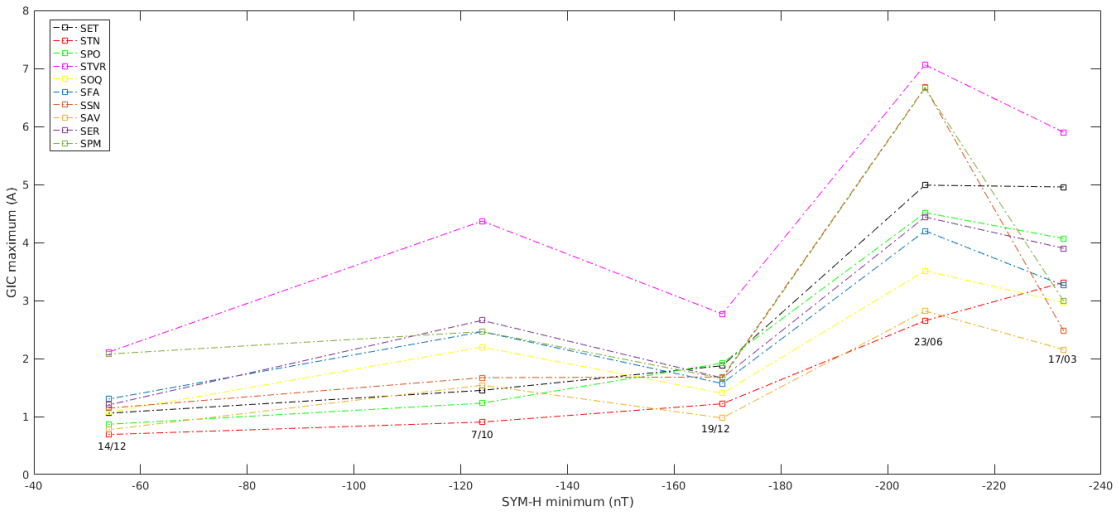

Figure 5.17: Relation of the minimum value of SYM-H from each storm and the GIC maximum at each substation.

From Figure 5.16 it can be seen that the highest GIC maximum for most of the substations occurs for the storm of June (which is the storm with highest values of induced electric field (see Section 4.4)), and the lowest maximum occurs for the first storm of December. This figure also shows that on average, the STVR substation has the highest GIC maximum for each storm.

Figure 5.17 shows the relation of the minimum value of SYM-H from each storm (taken from Figures 4.10 to 4.14) and the GIC maximum in each substation for each storm. It can be seen that the behavior of each substation tends to be the same but for different values of GIC, depending on SYM-H value. Once again the STVR substation is the one with higher values of GICs, as seen before.

Another way to see the different behavior of the substations is to analyze how the GICs change when the earthing resistance is different. For that it was computed the GIC caused by earthing resistances of 0.15 Ω and 0.25 Ω (Figure 5.18) and they were compared with the original value 0.20 Ω (Figure 5.19).

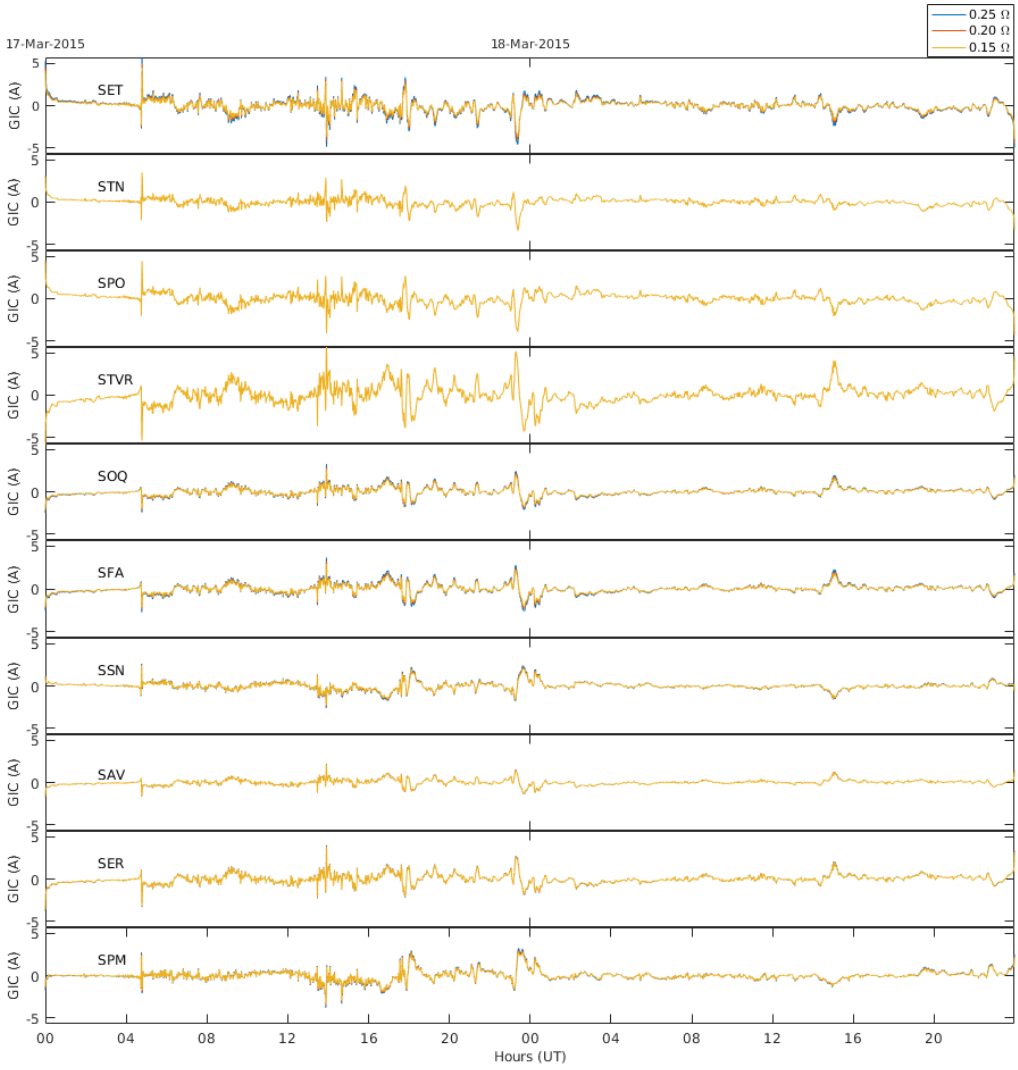

Figure 5.18: GIC values per substation for different earthing resistances, for the storm of March 2015.

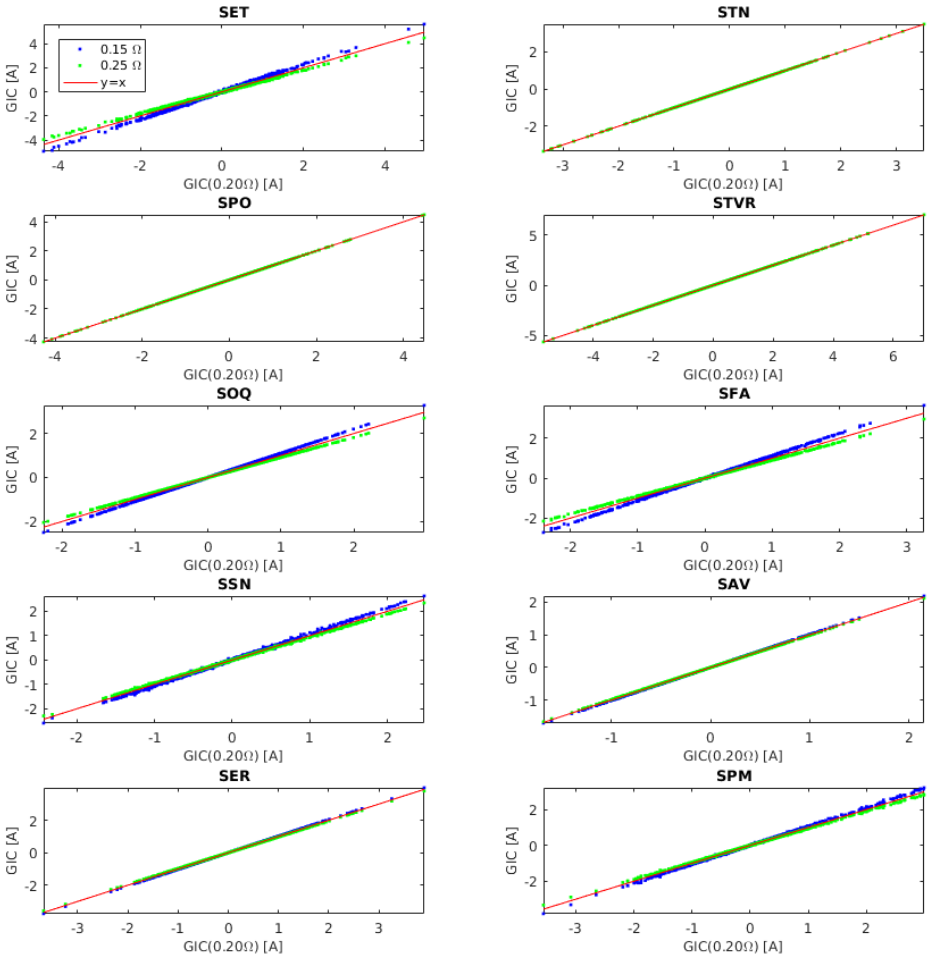

Figure 5.19: Comparison of GIC values using modified values of earthing resistances (vertical axis), with GIC values for reference parameters, for the storm of March 2015.

From Figures 5.18 and 5.19 it can be seen that the substations more sensitive to variations in the earthing resistances are SET, SOQ and SFA. It is also possible to see that the GIC values decrease with the increase of the earthing resistance.

	$\text{GIC}_{\text{alt}} = a + b\text{GIC}_{\text{orig}}$				$GIC_{0.20} = 2.5$		ΔGIC_1	ΔGIC_2
	a_1	b_1	a_2	b_2	$GIC_{0.15}$	$GIC_{0.25}$		
SET	-6.123E-11	1.145	4.697E-11	0.8943	2.862	2.236	**0.362**	**0.264**
STN	1.086E-17	1	1.086E-17	1	2.500	2.500	**0.000**	**0.000**
SPO	4.087E-17	1	4.087E-17	1	2.500	2.500	**0.000**	**0.000**
STVR	-5.638E-17	1	-5.638E-17	1	2.500	2.500	**0.000**	**0.000**
SOQ	1.135E-10	1.102	-8.196E-11	0.9135	2.755	2.284	0.255	0.216
SFA	1.681E-10	1.124	-1.098E-10	0.9015	2.810	2.254	0.310	0.246
SSN	-2.430E-10	1.061	1.768E-10	0.9459	2.652	2.365	0.152	0.135
SAV	4.407E-11	1.016	-3.437E-11	0.9836	2.540	2.459	0.040	0.041
SER	-8.445E-11	1.022	6.141E-11	0.9732	2.555	2.433	0.055	0.067
SPM	8.468E-10	1.057	-6.269E-10	0.9484	2.643	2.371	0.143	0.129

Table 5.1: Linear fit parameters for the data in Figure 5.19, where a_1 and b_1 are the intercept and slope of the regression line for GICs with earthing resistance 0.15 Ω, respectively, and a_2 and b_2 are the intercept and slope of the regression line for GICs with earthing resistance 0.25 Ω, respectively. For each substation and regression line, the difference between the real and the altered GIC is calculated for a real GIC value of 2.5 A, using the linear regression results. The substation with the largest difference is identified in red, while the substations with no variation are marked in green.

Table 5.1 confirms the observations made on Figure 5.19 but with greater detail. It is possible to identify three stations that do not display any variation of the GIC values when the earthing resistances are altered, these stations being STN, SPO and STVR. On the other hand, the SET substation displays the largest variation. Comparing the values obtained for 0.15 Ω and 0.25 Ω it can be verified that, as mentioned previously, the greater the earthing resistance the smaller the GICs.

Another analysis that can be made on Table 5.1 is that within the range of earthing resistivities evaluated here (0.15 Ω to 0.25 Ω), the assumption of 0.20 Ω values can result in a GIC miscalculation of the order of $\sim 10\%$. This result is particularly valid for this regions for which this grounding resistance interval is representative of the transformer stations can presented there. Yet other stations can present earthing resistances well outside this range (*e.g.*, 0.6 Ω (Myllys et al., 2014), which would require an extension of this work to those values.

Making the same analyses, but for an extend version of the previous model it comes the results in Figure 5.20 with the its linear fit parameters for the data in Table 5.2. This modified model is just the original one with an equivalent circuit north of Palmela to simulate the substations north of it.

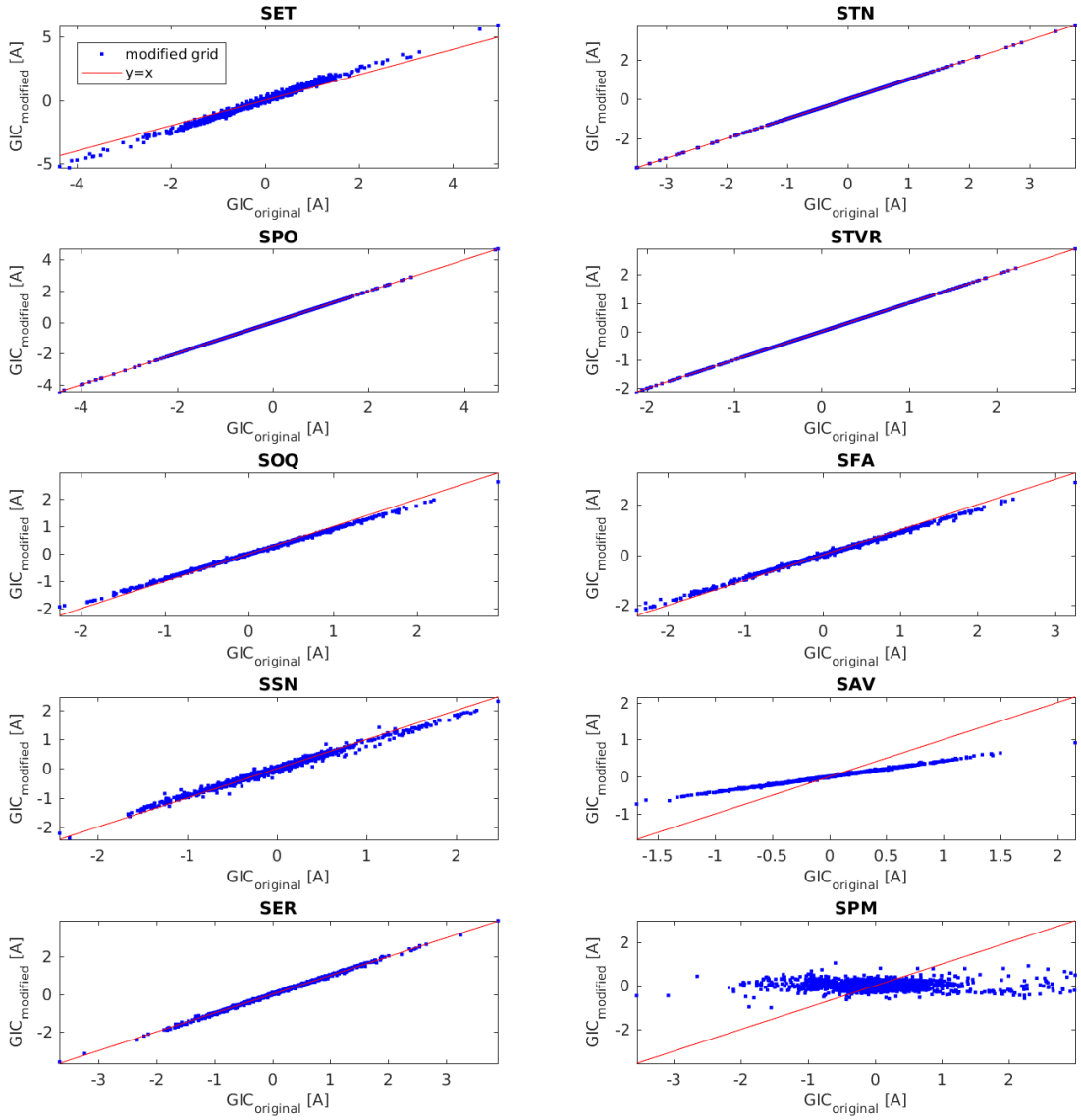

Figure 5.20: Relation between the GICs of the modified network and the original values, per substation for for the storm of March 2015.

	$GIC_{modif} = a_1 + b_1 GIC_{orig}$		$GIC_{orig} = 2.5$	$\lvert\Delta GIC\rvert$
	a_1	b_1	GIC_{modif}	
SET	-1.422E-10	1.223	3.057	0.557
STN	-9.311E-18	1.000	2.500	0.000
SPO	-2.276E-17	1.000	2.500	0.000
STVR	2.586E-19	1.000	2.500	0.000
SOQ	-3.040E-10	0.900	2.250	0.250
SFA	-6.187E-10	0.907	2.268	0.232
SSN	-1.519E-9	0.922	2.304	0.196
SAV	-5.735E-11	0.423	1.057	1.443
SER	-4.365E-10	1.007	2.517	0.017
SPM	1.058E-8	-0.005	-0.013	2.513

Table 5.2: Linear fit parameters for the data on Figure 5.20, where a_1 and b_1 are the intercept and slope of the regression line for GICs in the modified model. For each substation and regression line, the difference between the real and the modified GIC is calculated for a real GIC value of 2.5 A, using the linear regression results. The substation with the largest difference is identified in red, while the substations with no variation are marked in green.

The SPM station has the highest difference between the modified grid value and the original one because it is at the end of the grid, which means that it has an equivalent circuit attached as if it was the grid north of it. And that is the reason why STN, SPO or SER does not change, because their connections stayed the same.

Chapter 6

Conclusions

Space Weather is nowadays a really exciting field of study that contributes to our understanding of the impact of Solar activity on Earth-based technological systems. It is well-known that geomagnetic storms can have a strong impact on power grids, both in large and small scale power network systems by inducing GICs. Studies on GICs depend on two main areas: geophysical studies (Magnetotelluric method to study the conductivity model of the region) and space weather (geomagnetic storms).

The *MAG-GIC* project is the first of its kind to study these effects in the Portuguese power network to help understand the potential risks and limitations of the country's network topology.

The geomagnetic storms have different sources which influence their behavior. These sources can be better characterized by studying the precursors and proxies of the storms. In this work a detailed study of five, amongst the most important storms during 2015, was carried out. Through the magnetic field measured at the COI observatory it was possible to compute the induced electric field for each of those storms. It was verified that this electric field tends to be perpendicular to the conductivity discontinuity region (the coastline) and it is also more intense there than when compared with regions away from the coast. Also, the more intense the storm is (highest induced electric field) the greater the GICs will be.

Computing the GICs for each substation with a standard uniform induced field of 1 V/km, allowed to determine their individual responses and which are more sensitive. This sensitivity depends on the specific characteristics of each substation, such as location, grounding resistance, number of line connections, etc.

As shown in Figures 5.8 and 5.15 the substations at the coast have, in general, higher GICs (SET, SGN and SPM). However, the STVR substation has the highest GIC maximum for all the storms, as seen in Figure 5.16, which can be explained by its connection to the three substations in the south coast and by being at the end of the network.

Another thing that affects the GIC values at a substation is the earthing resistance. It is shown that STN, SPO, STVR, SAV and SER substations hardly feel some difference when the earthing resistance is changed, but on the other hand, SET, SOQ and SFA substations display different GIC values. The SET substation is one of the substations with highest values of GIC and one of those more sensitive to the earthing resistance which make it one of the more sensitive to GICs. These results can be observed in Figures 5.18 and 5.19.

By assessing the sensitivity of different substations to geomagnetic storms, the next step will be the prevention of major damages in the power network when it is known that a major storm is coming. The information in this study can be used to mitigate potential issues in the power grid and provide solutions to potentially severe problems, involving both engineering solutions (like, e.g., the grounding resistors) and logistic solutions (like how to best implement these changes to optimize results, costs, etc.).

6.1 Future Work

For a future work it would be interesting to study the behavior of the substations to the change in other network parameters (line resistances, number of connections, type of transformers, etc.)

Another application of this kind of study is on the installation of a Hall Effect probe to directly measure the flow of GICs to and from the ground at a single transformer. Since it is a very expensive equipment, these studies help to choose the best location for it. As said before, with the data presented the SET substation appears to be the more sensitive one and therefore a good candidate to the installation of the Hall Effect probe.

MAG-GIC project started with the area south of Palmela due to its simplicity in terms of the electrical network and the privileged position of having the two coastal areas with different directions, allowing to see different behaviors and to test the models in a simpler network. The aim is to apply the model to the whole country taking into account that more urban areas such as the region of Lisbon will always be a huge challenge due to its complexity.

Bibliography

Alfvén, H. (1942). Existence of electromagnetic-hydrodynamic waves. *Nature*, 150(3805):405–406.

Alves, M., Echer, E., and Gonzalez, W. (2006). Geoeffectiveness of corotating interaction regions as measured by dst index. *Journal of Geophysical Research: Space Physics*, 111(A7).

Alves Ribeiro, J. (2018). *Magnetotelluric studies in detecting an old suture zone and major crustal scale shear zones (Iberia)*. PhD thesis, Universidade de Lisboa, Faculdade de Ciências.

Alves Ribeiro, J. et al. (2020). Geomagnetically induced currents in the south of portugal. *Space Weather (submitted)*.

Ambastha, A. (2020). *Physics of the Invisible Sun: Instrumentation, Observations, and Inferences*. CRC Press.

Antiochos, S., Mikić, Z., Titov, V., Lionello, R., and Linker, J. (2011). A model for the sources of the slow solar wind. *The Astrophysical Journal*, 731(2):112.

Arajarvi, E. and Viljanen, A. (2008). Geomagnetically induced current estimation in the wisconsin 345kv power grid. *Rep 1018125, EPRI*.

Azzarone, A. (2003a). Istituto nazionale di geofisica e vulcanologia – dst index. http://roma2.rm.ingv.it/en/themes/23/geomagnetic_indices/27/dst_index.

Azzarone, A. (2003b). Istituto nazionale di geofisica e vulcanologia – kp planetary index. http://roma2.rm.ingv.it/en/themes/23/geomagnetic_indices/23/kp_planetary_index.

Bailey, R. (2018). *Space weather and geomagnetically induced currents in Austria*. PhD thesis, University of Wien.

Bailey, R. L., Halbedl, T. S., Schattauer, I., Römer, A., Achleitner, G., Beggan, C. D., Wesztergom, V., Egli, R., and Leonhardt, R. (2017). Modelling geomagnetically induced currents in midlatitude central europe using a thin-sheet approach. In *Annales Geophysicae*, volume 35, pages 751–761. European Geosciences Union.

Balan, N., Tulasiram, S., Kamide, Y., Batista, I., Souza, J., Shiokawa, K., Rajesh, P., and Victor, N. J. (2017). Automatic selection of dst storms and their seasonal variations in two versions of dst in 50 years. *Earth, Planets and Space*, 69(1):59.

Basu, S. and Antia, H. (2008). Helioseismology and solar abundances. *Physics Reports*, 457(5-6):217–283.

Bernabeu, E. E. (2012). Modeling geomagnetically induced currents in dominion virginia power using extreme 100-year geoelectric field scenarios—part 1. *IEEE Transactions on Power Delivery*, 28(1):516–523.

Bernhardi, E., Cilliers, P., and Gaunt, C. (2008). Improvement in the modelling of geomagnetically induced currents in southern africa. *South African Journal of Science*, 104(7-8):265–272.

Bhaskar, A. and Vichare, G. (2019). Forecasting of symh and asyh indices for geomagnetic storms of solar cycle 24 including st. patrick's day, 2015 storm using narx neural network. *Journal of Space Weather and Space Climate*, 9:A12.

Blake, S. (2017). *Modelling and monitoring geomagnetically induced currents in Ireland*. PhD thesis, Trinity College Dublin.

Blake, S. P., Gallagher, P. T., Campanyà, J., Hogg, C., Beggan, C. D., Thomson, A. W., Richardson, G. S., and Bell, D. (2018). A detailed model of the irish high voltage power network for simulating gics. *Space Weather*, 16(11):1770–1783.

Borovsky, J. E. and Denton, M. H. (2006). Differences between cme-driven storms and cir-driven storms. *Journal of Geophysical Research: Space Physics*, 111(A7).

Boteler, D. (2013). The use of linear superposition in modelling geomagnetically induced currents. In *2013 IEEE Power & Energy Society General Meeting*, pages 1–5. IEEE.

Boteler, D., Bui-Van, Q., and Lemay, J. (1994). Directional sensitivity to geomagnetically induced currents of the hydro-quebec 735 kv power system. *IEEE Transactions on Power Delivery*, 9(4):1963–1971.

Boteler, D. and Pirjola, R. (2014). Comparison of methods for modelling geomagnetically induced currents. *Annales Geophysicae (09927689)*, 32(9).

Boteler, D. and Pirjola, R. (2017). Modeling geomagnetically induced currents. *Space Weather*, 15(1):258–276.

Cagniard, L. (1953). Basic theory of the magneto-telluric method of geophysical prospecting. *Geophysics*, 18(3):605–635.

Cairns, I. (2000). Lecture 8: Formation of the solar wind.

Caraballo, R. (2016). The south atlantic magnetic anomaly phenomena: its impact on the technological infrastructure. *Master in Geosciences, Montevideo*.

Caraballo, R., Sánchez Bettucci, L., and Tancredi, G. (2013). Geomagnetically induced currents in the uruguayan high-voltage power grid. *Geophysical Journal International*, 195(2):844–853.

Carneiro, R. L. (2005). Stellar evolution and social evolution: A study in parallel processes. *Social Evolution & History*, 4(1):136–159.

Cherkose, B. A. and Mizunaga, H. (2018). Resistivity imaging of aluto-langano geothermal field using 3-d magnetotelluric inversion. *Journal of African Earth Sciences*, 139:307–318.

Cnossen, I. and Richmond, A. D. (2012). How changes in the tilt angle of the geomagnetic dipole affect the coupled magnetosphere-ionosphere-thermosphere system. *Journal of Geophysical Research: Space Physics*, 117(A10).

Cnossen, I., Wiltberger, M., and Ouellette, J. E. (2012). The effects of seasonal and diurnal variations in the earth's magnetic dipole orientation on solar wind–magnetosphere-ionosphere coupling. *Journal of Geophysical Research: Space Physics*, 117(A11).

da Silva Barbosa, C., Hartmann, G. A., and Pinheiro, K. J. (2015). Numerical modeling of geomagnetically induced currents in a brazilian transmission line. *Advances in Space Research*, 55(4):1168–1179.

Demorest, P. (2001). Dynamo theory and earth's magnetic field.

Erinmez, I. A., Kappenman, J. G., and Radasky, W. A. (2002). Management of the geomagnetically induced current risks on the national grid company's electric power transmission system. *Journal of atmospheric and Solar-terrestrial physics*, 64(5-6):743–756.

Fantaye, T. et al. (2011). Magnetotelluric and transient electromagnetic methods in geothermal exploration with examples from the krỳsuvík area, sw-iceland.

Ganushkina, N. Y., Liemohn, M., and Dubyagin, S. (2018). Current systems in the earth's magnetosphere. *Reviews of Geophysics*, 56(2):309–332.

Gilbert, J., Radasky, W., and Savage, E. (2012). A technique for calculating the currents induced by geomagnetic storms on large high voltage power grids. In *2012 IEEE International Symposium on Electromagnetic Compatibility*, pages 323–328. IEEE.

Gold, T. (1959). Motions in the magnetosphere of the earth. *Journal of Geophysical Research*, 64(9):1219–1224.

Gonzalez, W. D., Tsurutani, B. T., and De Gonzalez, A. L. C. (1999). Interplanetary origin of geomagnetic storms. *Space Science Reviews*, 88(3-4):529–562.

Goossens, M. (2012). *An introduction to plasma astrophysics and magnetohydrodynamics*, volume 294. Springer Science & Business Media.

Gosling, J. T. (2007). Chapter 5 - the solar wind. In McFadden, L.-A., Weissman, P. R., and Johnson, T. V., editors, *Encyclopedia of the Solar System (Second Edition)*, pages 99 – 116. Academic Press, San Diego, second edition edition.

Guo, S.-X., Liu, L.-G., Pirjola, R. J., Wang, K.-R., and Dong, B. (2014). Impact of the ehv power system on geomagnetically induced currents in the uhv power system. *IEEE Transactions on Power Delivery*, 30(5):2163–2170.

Hamilton, D. C., Gloeckler, G., Ipavich, F., Stüdemann, W., Wilken, B., and Kremser, G. (1988). Ring current development during the great geomagnetic storm of february 1986. *Journal of Geophysical Research: Space Physics*, 93(A12):14343–14355.

Hathaway, D. H. (2015). The solar cycle. *Living Reviews in Solar Physics*, 12(1):4.

Hughes, J. (2016). Fundamentals of space physics.

Hundhausen, A. J. (2012). *Coronal expansion and solar wind*, volume 5. Springer Science & Business Media.

Kallenrode, M.-B. (2003). An introduction to plasmas and particles in the heliosphere and magnetospheres.

Kelly, G., Viljanen, A., Beggan, C., and Thomson, A. (2017). Understanding gic in the uk and french high-voltage transmission systems during severe magnetic storms. *Space Weather*, 15(1):99–114.

Koen, J. and Gaunt, T. (2003). Geomagnetically induced currents in the southern african electricity transmission network. In *2003 IEEE Bologna Power Tech Conference Proceedings*, volume 1, pages 7–pp. IEEE.

Kontar, E., Hannah, I., and MacKinnon, A. (2008). Chromospheric magnetic field and density structure measurements using hard x-rays in a flaring coronal loop. *Astronomy & Astrophysics*, 489(3):L57–L60.

Koskinen, H. (2011). *Physics of space storms: From the solar surface to the Earth*. Springer Science & Business Media.

Kunagu, P. and Chandrasekhar, E. (2013). External field characterization using champ satellite data for induction studies. *Journal of Earth System Science*, 122(3):651–660.

Laundal, K. M. and Richmond, A. D. (2017). Magnetic coordinate systems. *Space Science Reviews*, 206(1-4):27–59.

Lehtinen, M. (1985). Currents produced in earthed conductor networks by geomagnetically-induced electric fields. *Ann. Geophys.*, 3(4):479–484.

Lepping, R., Jones, J., and Burlaga, L. (1990). Magnetic field structure of interplanetary magnetic clouds at 1 au. *Journal of Geophysical Research: Space Physics*, 95(A8):11957–11965.

Liu, C., Li, Y., and Pirjola, R. (2014). Observations and modeling of gic in the chinese large-scale high-voltage power networks. *Journal of Space Weather and Space Climate*, 4:A03.

Liu, C.-m., Li, Y.-l., and Chen, L. (2013). Modelling geomagnetically induced currents in xinjiang 750kv power grid in china. In *2013 IEEE Power & Energy Society General Meeting*, pages 1–5. IEEE.

Lopez, R. E. and Gonzalez, W. (2017). The external chapman-ferraro current. *AGUFM*, 2017:SM11A–2294.

Makinen, T. (1993). *Geomagnetically induced currents in the Finnish power transmission system.* Ilmatieteen laitos Helsinki.

Marshall, R., Dalzell, M., Waters, C., Goldthorpe, P., and Smith, E. (2012). Geomagnetically induced currents in the new zealand power network. *Space Weather*, 10(8).

Marshall, R., Smith, E., Francis, M., Waters, C., and Sciffer, M. (2011). A preliminary risk assessment of the australian region power network to space weather. *Space Weather*, 9(10).

Martini, D., Argese, C., Di Loreto, M., and Mursula, K. (2016). Revisiting geomagnetic activity at auroral latitudes: No need for regular quiet curve removal for geomagnetic activity indices based on hourly data. *Journal of Geophysical Research: Space Physics*, 121(7):6307–6323.

McKay, A. J. (2004). Geoelectric fields and geomagnetically induced currents in the united kingdom.

Miensopust, M. (2010). *Multidimensional Magnetotellurics: a 2D case study and a 3D approach to simultaneously invert for resistivity structure and distortion parameters.* PhD thesis, National University of Ireland.

Monteiro Santos, F. A., Soares, A., Nolasco, R., Rodrigues, H., Luzio, R., Palshin, N., and team, I.-D. (2003). Lithosphere conductivity structure using the cam-1 (lisbon-madeira) submarine cable. *Geophysical Journal International*, 155(2):591–600.

Myllys, M., Viljanen, A., Rui, Ø. A., and Ohnstad, T. M. (2014). Geomagnetically induced currents in norway: the northernmost high-voltage power grid in the world. *Journal of Space Weather and Space Climate*, 4:A10.

Narita, Y. (2012). *Plasma turbulence in the solar system.* Springer Science & Business Media.

Newell, P., Sotirelis, T., Liou, K., Meng, C.-I., and Rich, F. (2007). A nearly universal solar wind-magnetosphere coupling function inferred from 10 magnetospheric state variables. *Journal of Geophysical Research: Space Physics*, 112(A1).

Ngwira, C. M., Pulkkinen, A., McKinnell, L.-A., and Cilliers, P. J. (2008). Improved modeling of geomagnetically induced currents in the south african power network. *Space Weather*, 6(11).

Nowada, M., Shue, J.-H., and Russell, C. (2009). Effects of dipole tilt angle on geomagnetic activity. *Planetary and Space Science*, 57(11):1254–1259.

Pethick, A. (1999). Tutorial - 1d forward modelling (magnetotelluric). http://www.digitalearthlab.com/tutorial/tutorial-1d-mt-forward/.

Pinheiro, F. et al. (2020). From geomagnetic observations at coi to gics in the portuguese power system network. *Space Weather (subm).*

Pirjola, R. (1985). Currents produced in the finnish 400kv power transmission grid and in the finnish natural gas pipeline by geomagnetically-induced electric fields. *Ann. Geophys.*, 3(4):485–491.

Pulkkinen, A., Bernabeu, E., Thomson, A., Viljanen, A., Pirjola, R., Boteler, D., Eichner, J., Cilliers, P., Welling, D., Savani, N., et al. (2017). Geomagnetically induced currents: Science, engineering, and applications readiness. *Space Weather*, 15(7):828–856.

Radasky, W., Kappenman, J., and Gilbert, J. (2006). An overview of the development and validation of large power grid models for geomagnetic storms. In *The 2006 4th Asia-Pacific Conference on Environmental Electromagnetics*, pages 25–28. IEEE.

Rosales, Y. (2017). *Global and Mid-Latitude impact of ten years of solar activity using observational data of the Geophysical and Astronomical observatory of the University of Coimbra.* PhD thesis, University of Coimbra.

Schatten, K. H., Wilcox, J. M., and Ness, N. F. (1969). A model of interplanetary and coronal magnetic fields. *Solar Physics*, 6(3):442–455.

Simpson, F. and Bahr, K. (2005). *Practical magnetotellurics.* Cambridge University Press.

Smith, E. J., Tsurutani, B. T., and Rosenberg, R. L. (1978). Observations of the interplanetary sector structure up to heliographic latitudes of 16: Pioneer 11. *Journal of Geophysical Research: Space Physics*, 83(A2):717–724.

SpaceWeatherlive (2003). Space weather live global – real-time auroral and solar activity. https://www.spaceweatherlive.com/en/help/the-kp-index.

Syed, B. A., Siddiqui, F. I., et al. (2012). Use of vertical electrical sounding (ves) method as an alternative to standard penetration test (spt). In *The Twenty-second International Offshore and Polar Engineering Conference*. International Society of Offshore and Polar Engineers.

Tarditi, T. J. V. S. A. and Harte, M. V. (2014). Application of geomagnetic disturbance vulnerability assessments using the eskom main transmission system model. CIGRE 2014.

Thiel, S. (2008). *Modelling and inversion of magnetotelluric data for 2-D and 3-D lithospheric structure, with application to obducted and subducted terranes.* PhD thesis.

Thorberg, R. (2012). Risk analysis of geomagnetically induced currents in power systems. *Division of Industrial Electrical Enginnering and Automation Faculty of Engineering, LTH, Lund University.*

Tikhonov, A. (1950). On determining electrical characteristics of the deep layers of the earth's crust. In *Doklady*, volume 73, pages 295–297.

Torta, J. M., Marsal, S., and Quintana, M. (2014). Assessing the hazard from geomagnetically induced currents to the entire high-voltage power network in spain. *Earth, Planets and Space*, 66(1):87.

Travassos, J. and Beamish, D. (1988). Magnetotelluric data processing—a case study. *Geophysical Journal International*, 93(2):377–391.

Tsurutani, B. T. and Gonzalez, W. D. (1997). The interplanetary causes of magnetic storms: A review. *GMS*, 98:77–89.

Turnbull, K. (2010). Modelling gic in the uk. *Astronomy & Geophysics*, 51(5):5–25.

Turnbull, K. (2011). *Modelling of geomagnetically induced currents in the United Kingdom*. PhD thesis, PhD thesis, University of Lancaster.

Turner, N. E., Baker, D., Pulkkinen, T., and McPherron, R. (2000). Evaluation of the tail current contribution to dst. *Journal of Geophysical Research: Space Physics*, 105(A3):5431–5439.

Unsworth, M. (2015). Magnetotelluric studies of lithospheric structure beneath western canada: insights into plate tectonics both past and present. *Department of physics, University of Alberta, Edmonton, Canada*, pages 28–32.

Vo, T. (2018). Parker spirals – a study on the structure of the interplanetary magnetic field.

Watari, S. (2017). Geomagnetic storms of cycle 24 and their solar sources. *Earth, Planets and Space*, 69(1):1–8.

Wik, M., Viljanen, A., Pirjola, R., Pulkkinen, A., Wintoft, P., and Lundstedt, H. (2008). Calculation of geomagnetically induced currents in the 400 kv power grid in southern sweden. *Space weather*, 6(7).

Zheng, K., Liu, L., Ge, H., and Li, W. (2012). Comparative study of the gic amplitudes and characteristics in different power grids in china. In *Proc. 44th CIGRE*.